Time sequence of TGFs and optical pulses detected by ASIM and a comparison of TGFs observed by different spacecrafts

Master Thesis in Space Physics
by
Ingrid Bjørge-Engeland

Supervisor: Professor Nikolai Østgaard

Department of Physics and Technology
University of Bergen
June 15, 2020

Acknowledgements

First and foremost I want to express my gratitude to my supervisor, Professor Nikolai Østgaard, for his invaluable guidance, advice and support. I also want to thank Chris Alexander Skeie for his generous support and the countless hours spent discussing methods and trying out different approaches for data analysis. For this, I am extremely grateful. I would like to thank Andrey Mezentsev for his extensive guidance with processing the ASIM data and for helpful discussions. I wish to extend my gratitude to Anders Lindanger and the rest of the Hard Radiation from Thunderstorms group at Birkeland Centre for Space Science for interesting discussions over the past two years.

I also want to thank the ASIM team, the World Wide Lightning Location Network, Vaisala, the AGILE Science Data Center, as well as the Fermi and RHESSI teams for providing the data used in this thesis.

Furthermore, I wish to thank my fellow master students Amalie, Andreas, Espen, Hector, Jone, Josephine, Judith, Ragnar and Simon for interesting discussions and good times, Kevin for valuable particle physics discussions and enjoyable lunchbreaks over the past five years, and Eldho, Isabel and Torunn for the amusing coordinated breaks.

Last, but not least, I would like to thank my parents for their constant support and inspiration.

Abstract

Terrestrial gamma-ray flashes (TGFs) are short energetic bursts of photons associated with lightning activity. TGFs are believed to be produced in relation to positive intracloud (IC+) lightning, during the upward propagation of the negative lightning leader. In April 2018, the Atmospheric Space Interactions Monitor (ASIM) was launched and mounted on the Columbus module on the International Space Station (ISS), and is the first mission specifically designed for detection of TGFs from space. Using catalogs of TGFs detected by other platforms prior to the launch of ASIM, we studied the global distribution of TGFs, and how the instrumental properties of the spacecrafts affect the TGF durations and number of counts. By using both X- and γ-ray detections and optical detections by ASIM, we investigated the TGF duration and the time sequence of TGFs and optical lightning pulses.

Data from both detector modules of ASIM, the Modular X- and Gamma-ray Sensor (MXGS) and the Modular Multi-spectral and Imaging Array (MMIA), were used to construct timelines of ASIM detections. Between June 2018 and March 2019, the relative timing accuracy of MXGS and MMIA was ± 80 μs. Within this timespan, 95 TGFs detected by MXGS had associated optical detections by MMIA. Of these, 39 had clear optical associations. Lightning detection network data were used to ascertain that the detected optical pulses originated from lightning activity occurring within the field of view of MMIA.

TGFs detected by the different platforms showed similar geographic distributions, with a clustering of TGFs around the continents in the equatorial region. The ASIM TGF durations, determined using MXGS detections, were shorter than those previously found by other platforms. The ASIM TGFs also contained more counts. The time difference between the onset of the MXGS TGF detection and the onset of the associated optical pulse in MMIA, was used to study the time sequence of TGFs and the lightning strokes. The time sequence of ASIM TGFs (with optical pre-activity, TGF detection in MXGS, and main optical pulse detection in MMIA) suggests that TGFs are produced towards the later stages of leader development, before the current pulse heats up the channel to emit an optical pulse. The relation found between TGF duration and the delay of the associated optical pulses further suggests that the optical pulse is less delayed for shorter TGFs.

List of abbreviations

AC Anti-Coincidence (shield)
AGILE Astro-rivelatore Gamma a Immagini LEggero
ASIC Application Specific Integrated Circuit
ASIM Atmospheric Space Interactions Monitor
BATSE Burst and Transient Source Experiment
CEPA Columbus Externals Payloads Adaptor
CG Cloud to Gound (lightning)
CGR Compton Gamma-Ray (observatory)
CHU Camera Head Unit
DAU Data Assembly Unit
DHPU Data Handling and Power Unit
DHU Data Head Unit
DM Detector Module
DOY Day Of Year
DPU Data Processing Unit
ECEF Earth Centered Earth-Fixed
EM-CCD Electron-Multiplication Charged Coupled Device
FOV Field Of View
IC Intracloud (lightning)
ISS International Space Station
GBM Gamma-ray Burst Monitor
GRID Gamma-Ray Imaging Detector
GSHHHC Global Self-consistent Hierarchical High-resolution Geography Database
HED High-Energy Detector
HV High Voltage
HVPS High Voltage Power Supply
LAD Large-Area Detector
LASA Los Alamos Sferic Array
LAT Large-Area Telescope
LED Low-Energy Detector

LF Low Frequency

LMA Lightning Mapping Array

LWPC Long Wave Propagation Capability

MC Monte Carlo

MCAL Mini-CALorimeter

MMIA Modular Multi-spectral and Imaging Array

MXGS Modular X- and Gamma-ray Sensor

NLDN National Lightning Detection Network

PMT Photo-Multiplier Tube

RHESSI Reuven Ramaty High Energy Solar Spectroscopic Imager

RBEB Relativistic Binary-Encounter-Bethe

REAM Runaway Electron Avalanche Model

RMS Root Mean Square

RREA Relativistic Runaway Electron Avalanches

SAA South Atlantic Anomaly

SD Spectroscopy Detector

SCUs Sound Card Unit

TCP Time Correlation Pulse

TGF Terrestrial Gamma-ray Flash

TLE Transient Luminous Events

TOGA Time Of Group Arrival

TTE Time-Tagged Event

VLF Very Low Frequency

WWLLN World Wide Lightning Location Network

Contents

Chapter 1

Introduction

Terrestrial gamma-ray flashes (TGFs) are short energetic bursts of high-energy photons produced in association with lightning activity. When observed from space, they are believed to be produced during positive intracloud (IC+) lightning events [Roberts et al., 2018], and can have energies up to 30-40 MeV. TGF emissions from thunderclouds generate secondary electrons and positrons that can be detected by satellites in the inner parts of the magnetosphere [Dwyer et al., 2012]. TGFs were first observed by the Burst and Transient Source Experiment (BATSE) onboard the Compton Gamma-ray Observatory (CGR) in 1991 [Fishman et al., 1994], and have since been detected from space by Reuven Ramaty High Energy Solar Spectroscopic Imager (RHESSI) [Smith et al., 2005], Fermi Gamma-ray Burst Monitor [Briggs et al., 2010] and the Astrorivelatore Gamma a Immagini Leggero satellite (AGILE) [Marisaldi et al., 2013]. The first instrument specifically designed to observe TGFs, the Atmospheric Space Interactions Monitor (ASIM), was launched in April 2018 [Chanrion et al., 2019; Neubert et al., 2019; Østgaard et al., 2019b].

The TGFs that were first detected by BATSE could be distinguished from the events this platform was designed to observe (galactic gamma-ray bursts) because of their short millisecond durations. Since these first observations, TGFs have been monitored by different spacecrafts, and have most frequently been observed in equatorial regions, where thunderstorm activity is most prevalent. Their durations are now believed to be on the order of tens or hundreds of microseconds [Connaughton et al., 2013; Gjesteland et al., 2017; Marisaldi et al., 2013]. Whereas BATSE detected only 78 TGFs over its lifetime of nine years, RHESSI had a detection rate of 0.43 TGFs per day [Grefenstette et al., 2009]. Fermi obtained a detection rate of 2.2 TGFs per day [Roberts et al., 2018], and AGILE 0.3 TGFs per day [Marisaldi et al., 2013] before March 2015 (the detection rate then increased to 3 TGFs per day [Marisaldi et al., 2015]). TGFs occur in the proximity to coastlines [Splitt et al., 2010; Lindanger et al., 2020], with more TGFs occurring over bodies of water than over land [Roberts et al., 2018].

TGFs are produced by relativistic electrons in a bremsstrahlung process in the ambient field in thunderclouds [Dwyer et al., 2012; Skeltved et al., 2017]. Different theories were developed to explain the production of these relativistic electrons and how they are multiplied in relation to thunderstorms. The first theories focused on strong electric fields accelerating high-energy electrons to overcome the frictional force in air and run away. These strong electric fields could be the ambient fields within thunderclouds, and Gurevich et al., 1992, suggested that the multiplication of the electrons could take place by Møller scattering. This multiplication could produce Relativistic Runaway Electron Avalanches (RREAs), as outlined by Dwyer et al., 2012. The seed electrons believed to be involved in these processes were cosmic particles.

Moss et al., 2006, suggested that electrons could be multiplied and accelerated in the electric fields ahead of leaders [Skeltved et al., 2017]. The seed electrons needed in this scenario could originate from thermal runaway electrons that have been accelerated in the streamer tips. Bidirectional leaders, which initiate intracloud discharges, develop electric potential differences in the leader heads as they extend over kilometer lengths [Celestin and Pasko, 2011]. Celestin and Pasko, 2011, found through modelling, that from the overlapping electric fields in streamer tips, the majority of runaway electrons were able to obtain energies close to ∼65 keV. This energy is sufficient for the electrons to be further accelerated to relativistic energies in the electric fields produced by negative stepped leaders.

Due to timing uncertainties, the precise relationship between the lightning discharge development and TGF production is challenging to determine, but TGFs are believed to be related to the upward negative leader [Cummer et al., 2015]. By studying three TGFs, Cummer et al., 2015, found that TGFs could be produced in the middle of leader development, in terms of both location and timing, milliseconds after the leader initiation and several kilometers above, with the leader velocity seeming to increase with altitude. Shao et al., 2010, suggested, by analysing RHESSI TGFs, that TGFs are produced as the lightning discharge extended vertically from the negative to the positive charge region of the cloud. They also found that the TGFs occurred during the first milliseconds of intracloud (IC) flashes. Shao and Krehbiel, 1996, reported that the initial stage of IC development could last from several milliseconds to tens of milliseconds depending on the storm depth, as the leaders extend several kilometers within the clouds.

Several studies have investigated the time sequence of leader development and emission of optical pulses. Østgaard et al., 2013, reported on a simultaneous observation of a TGF and a corresponding optical signal, indicating that TGFs could be produced in the initial stage of an IC discharge, deep inside the thundercloud. The observed TGF had a very short duration of 70 μs. Gjesteland et al., 2017, argued that, due to the 1.5-2 ms time resolution of the optical data from the lighting imaging sensor (LIS), the sequence of emissions could not be accurately determined, but the TGF and the optical signal were found to occur simultaneously within ±1.6 ms. Using the first results from ASIM, with a relative timing accuracy of ±80 μs, Østgaard et al., 2019a, suggested that the majority of the

TGFs detected by ASIM are produced before the emission of an optical pulse, which is produced when the channel is heated by a large current pulse.

The main focus of this thesis will be the time sequence of TGFs and optical pulses detected by ASIM, and the duration of observed TGFs. The thesis will also include comparisons of the different platforms that have been used for TGF observations from space. The specific questions that will be addressed in this thesis are:

Comparison of platforms

1. Are there differences in the global distribution of TGFs detected by the different platforms?
2. Are there differences in the durations and number of counts detected by the different platforms?

ASIM TGFs

1. Are the onsets of the TGFs and the optical pulse simultaneous, or is there a delay of one relative to the other?
2. Is there a relation between the delay between the onsets of the TGF and the optical pulse, and the duration of the TGF?

Chapter 2

Theory

This chapter will outline the different mechanisms for electrification of clouds and different types of lightning discharges and different mechanism for the production of runaway electrons, as well as particle interactions in air.

2.1 Clouds and electrification of clouds

Thunderclouds are the primary source of lightning, and are most commonly found at low latitudes, in particular over warm coastal areas. The basic and simplified cloud charge structure is shown in Figure 2.1. In this idealized model, the cloud is located above a perfectly conducting ground. The tripole charge structure shows that there are two primary charge regions; the top positive region and the center negative region. The lower positive region might not always be present. The two primary charge regions are believed to be equal in magnitude and constitute a positive dipole. Cloud electrification mechanisms include processes of electrification of hydrometeors and processes of separating hydrometeors by their polarity, such that the distances between the charged regions of the clouds are on the order of kilometers [Rakov and Uman, 2003, ch.3].

The electric field due to each charge region is given by the vector sum of the charge region and its image. Image charges are used to obtain zero potential at the ground surface. Using the image method (Figure 2.2), where the negative point charge is placed a height H above the ground, and the electric field is found at a point on the ground surface, each contribution is given by:

$$|E^-| = |E^+| = \frac{|Q|}{4\pi\epsilon_0(H^2 + r^2)} \tag{2.1}$$

where r is the horizontal distance between the point charge and the observer. The field point is at the ground surface, where the potential is zero.

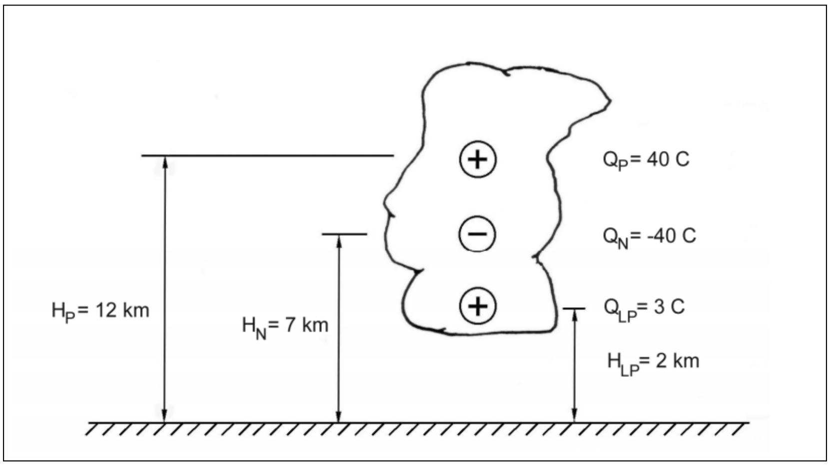

FIGURE 2.1: The tripole charge structure of a cumulonimbus. Figure from Rakov and Uman, 2003.

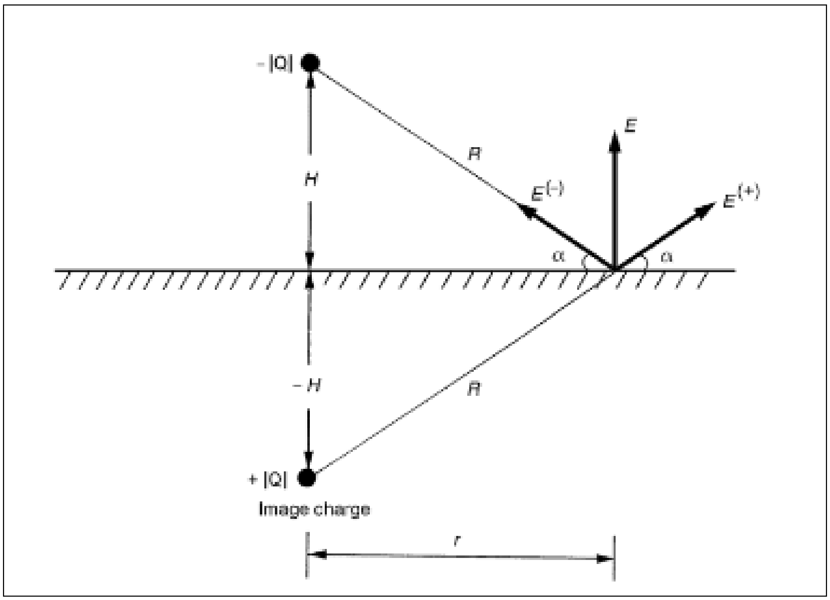

FIGURE 2.2: The image method for finding the electric field at a field point on the ground surface, due to a negative point charge above a perfectly conducting ground. Figure from Rakov and Uman, 2003.

The total electric field can be determined by summing the contributions from each charge region and the image charges. The vertical contribution from each charge region is given by:

$$\begin{aligned} |E| &= \frac{|Q|H}{2\pi\epsilon_0(H^2+r^2)^{3/2}} \\ &= k\frac{\sin\alpha}{R^2} \end{aligned} \tag{2.2}$$

where $R^2 = H^2 + r^2$ and $k = |Q|/(2\pi\epsilon_0)$, as shown by Rakov and Uman, 2003, ch. 3. R denotes the distance from the point charge to the observer, H the altitude of the point charge, and α denotes the angle between the ground surface and the radial field vectors. To obtain the total electric field, the three charge contributions have to be taken into account, giving three terms with different Q and R corresponding to each region. When $r = 0$, the electric field is dominated by the lower charge region. The upper charge contribution increases with r, and when r reaches the reversal distance, the contribution from the upper charge region becomes dominant, causing a reversal of the polarity. Figure 2.3 shows how the three charge regions contribute to the total electric field, and how the total electric field exhibits polarity reversals.

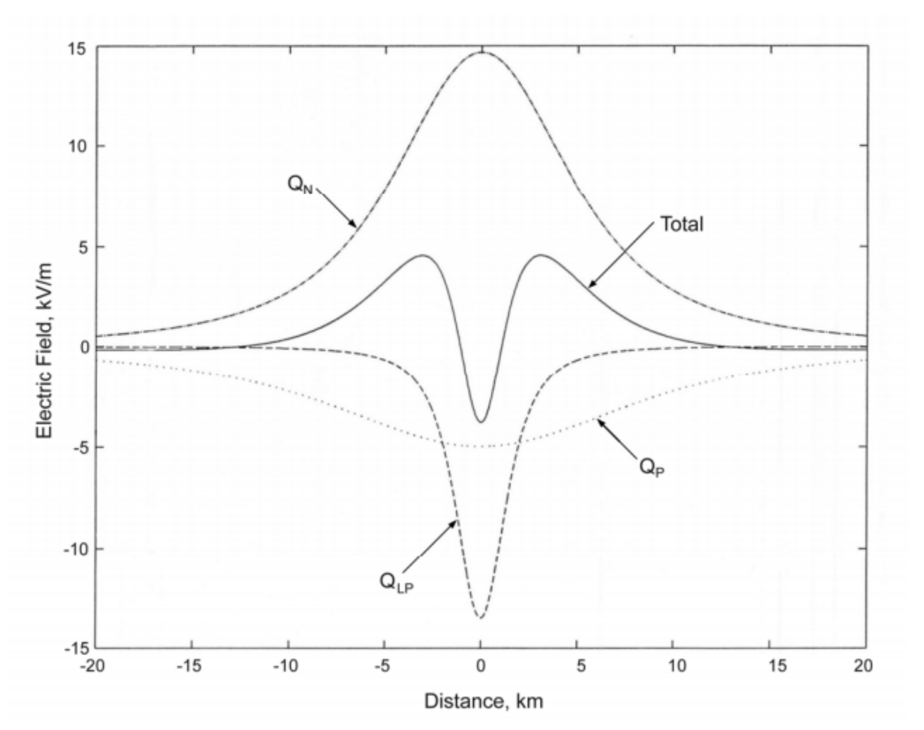

FIGURE 2.3: The electric field at the ground due to the tripole cloud charge structure, as a function of the distance from the tripole axis. The curve labelled "total" shows the total electric field. Figure from Rakov and Uman, 2003.

The electric field change in a cloud varies with distance to the tripole axis of the cloud (Figure 2.4). An electric field change is the difference between the final electric field value after a lightning discharge and the electric field value caused by the charge distributions of the original cloud [Rakov and Uman, 2003]. The field change associated with the removal of any charge is negative at any distance, because the upward-directed field associated with the negative charge becomes zero. In the occurrence of intracloud lightning and neutralization of both the positive and the main negative charge regions of the cloud, the resulting field change causes a polarity reversal (Figure 2.5). The field is negative at close distances to the tripole axis and positive at far distances, where the upper positive charge region dominates [Rakov and Uman, 2003, ch.3]. As outlined in Rakov and Uman, 2003, ch.3, the electric field is dominated by the reduction in upward-directed electric field at close ranges and by the reduction in downward-electric field at far ranges.

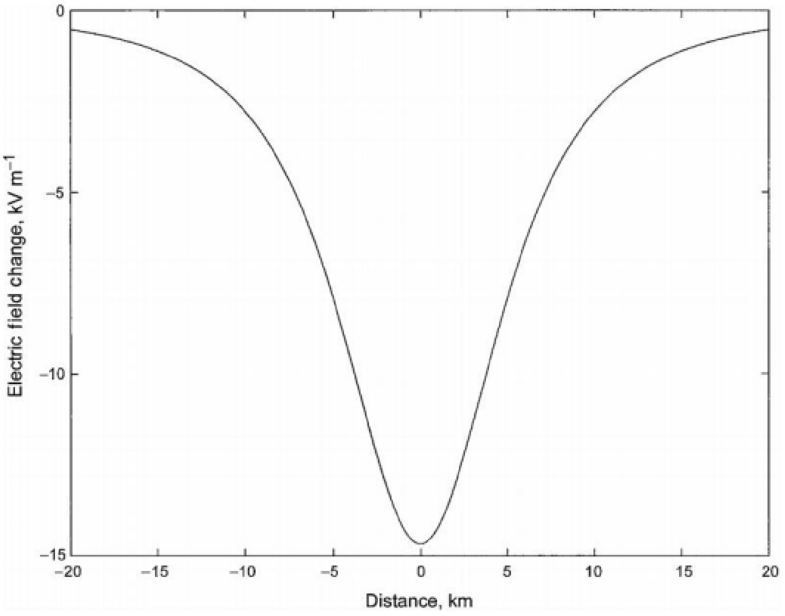

Figure 2.4: The electric field change at the ground as a function of the distance from the tripole axis, caused by the removal of negative charge. Figure from Rakov and Uman, 2003.

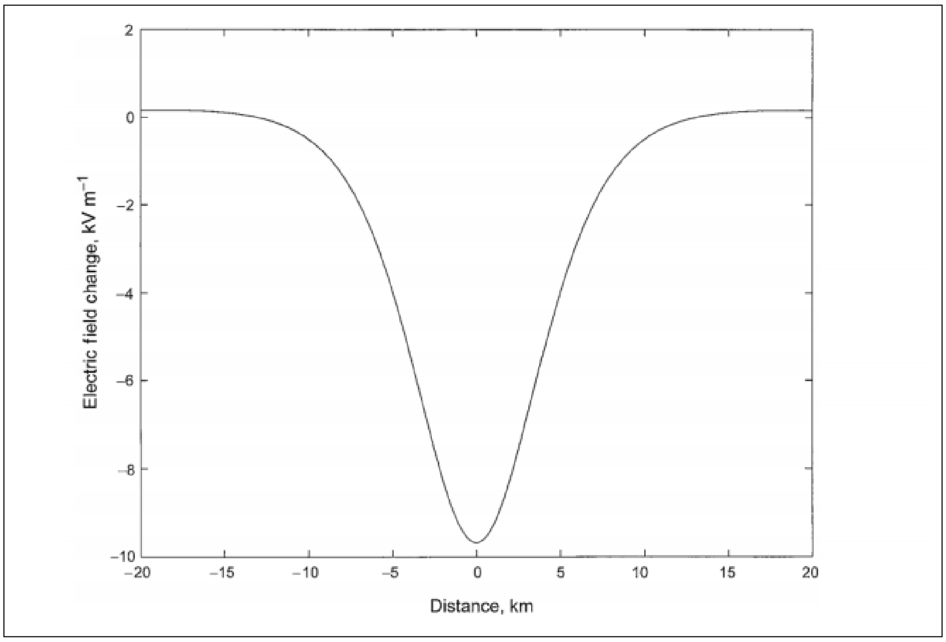

FIGURE 2.5: The change in the electric field at the ground, as a function of the distance from the tripole axis, caused by the removal of both the negative and upper positive charge. Figure from Rakov and Uman, 2003.

Under fair-weather conditions, the electric field vector is negative and directed downwards. This electric field is caused by positive charges found in the atmosphere and the negative charge of the Earth's surface. The typical magnitude of the fair-weather field is about 0.1 kV/m, and the ground-level electric field beneath an active thundercloud typically has a magnitude of 1-10 kV/m. Figure 2.6 shows how the electric field at the ground changes during a small storm. The fair-weather electric field is measured both before (until $\approx$ 12:30) and after (after $\approx$ 13:28) the storm. During the initiation of the storm, there is a slowly varying electric field, lasting for about 10 minutes. During the main parts of the storm, there is a large predominantly upward-directed electric field. This implies a dominant negative charge in the cloud above. The lightning discharges cause rapid changes in the electric field in association with charge neutralization [Rakov and Uman, 2003, ch.3].

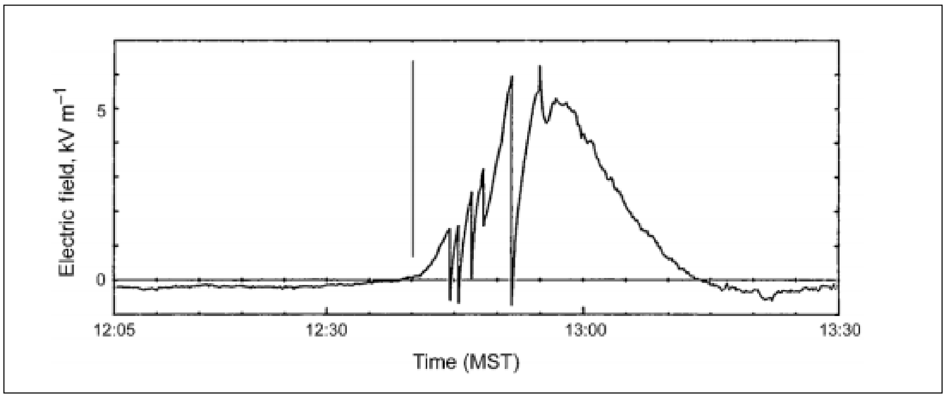

FIGURE 2.6: Measurements of the electric field at the ground about 5 km from a small storm in New Mexico, 1984. Figure from Rakov and Uman, 2003.

The two most commonly addressed cloud electrification mechanisms are the convection mechanism and the graupel-ice mechanism. In the convection mechanism (Figure 2.7), the electric charges are supplied by external sources, such as fair-weather positive space charges, corona near the ground and cosmic rays found near cloud tops. As described by Rakov and Uman, 2003, ch.3, updrafts carry positive fair-weather space charges to the top of the growing cloud. Cosmic rays above the cloud produce negative charges that attract to the cloud boundaries because of the positive space charges. Negative charges, produced by cosmic rays, attach to the cloud to form a negative screening layer. Due to cooling and convective circulation, downdrafts bring negative charges down the sides of the cloud. The negative charges aligned along the lower side boundaries of the cloud produce a positive corona at the surface (shown in (b) in Figure 2.7). The corona in turn produces a positive feedback, leading to a large positive space charge underneath the cloud (shown in (c)). The result of this mechanism is a positive cloud-charge dipole. It is unlikely that the main negative charge region produced is within the temperature range of thunderstorms, and this mechanism is therefore not considered the most probable cloud electrification mechanism [Rakov and Uman, 2003, ch.3].

The graupel-ice mechanism is believed to be the dominant cloud electrification mechanism. As ice crystals rise they collide with descending graupel, which are generally larger than the ice crystals. Collisions happen in the presence of water droplets, which is necessary for having any significant charge transfer, as shown experimentally by Takahashi, 1978, and Jayaratne et al., 1983. The charge transfer processes between the large graupel and the smaller cloud particles vary with temperature (Figure 2.8). When graupel experience temperatures below the reversal temperature (between -10° and -20°), the graupel obtain a negative charge after the collision and the ice crystals a positive charge. For collisions above this temperature, the graupel obtain a positive charge, and this could explain the existence of the lower positive charge region. The temperatures where the sign reversal happen correspond to the temperature range found in the main negative charge region of thunderclouds [Rakov and Uman, 2003, ch.3].

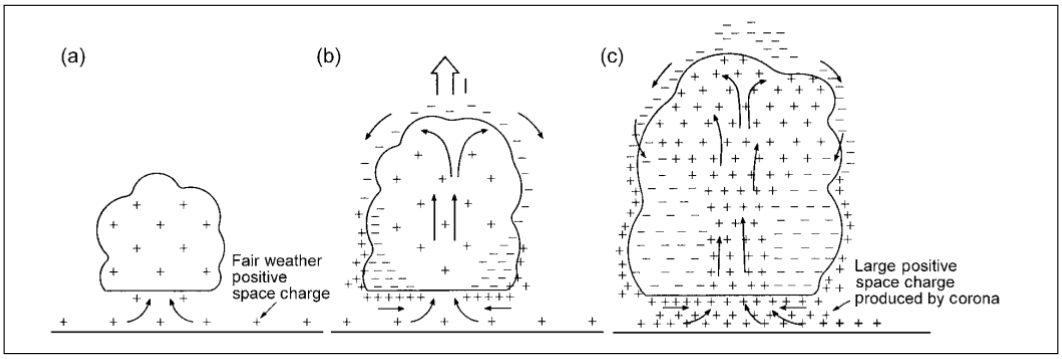

Figure 2.7: Illustration of the convection mechanism. Figure from Rakov and Uman, 2003 (adapted from MacGorman and Rust, 1998).

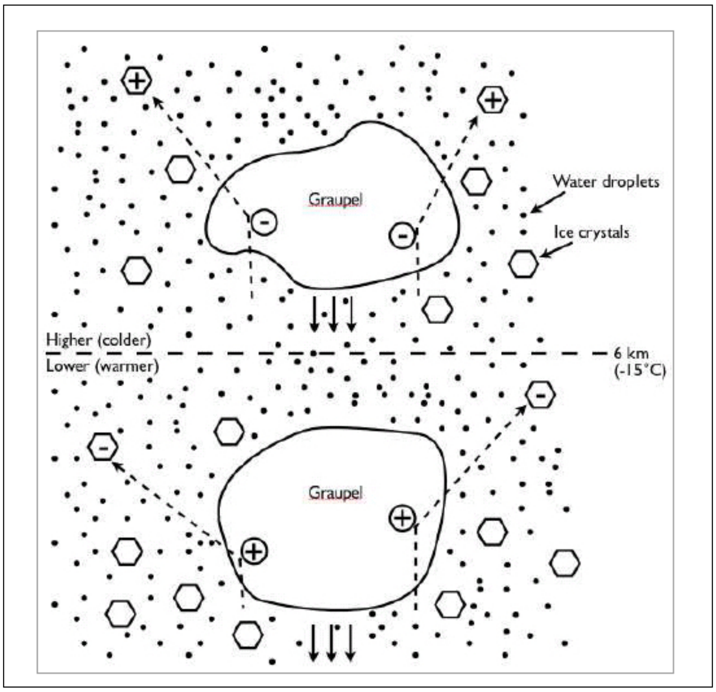

Figure 2.8: The charge transfer process between graupel and ice crystals. Figure from Rakov and Uman, 2003.

2.2 Lightning discharges

There are different types of lightning discharges (Figure 2.9), including cloud-to-ground (CG) discharges (lowering charge to the ground) and cloud discharges. Cloud discharges constitute the majority of the lightning discharges (about 75%), and can be divided into intracloud discharges, intercloud discharges and cloud-to-air discharges [Rakov and Uman, 2003, ch.1]. Positive intracloud lightning, IC^+, transports negative charge upwards, and negative intracloud lightning, IC^-, transports negative charge downwards. Cloud discharges dominate in the early stages of a thunderstorm, and pulses occurring in the early stages of cloud discharges are referred to as initial breakdown-pulses [Rakov and Uman, 2003, ch. 9].

CG discharges are less frequent than IC discharges, and include downward and upward negative lightning, as well as downward and upward positive lightning. Downward negative lightning accounts for about 90% of the global CGs, and downward positive lightning accounts for about 10% of the CGs [Rakov and Uman, 2003, ch.1]. The CGs are initiated by electrical breakdown processes in the cloud, and a column of charge (a stepped leader) is created when negative charge is transported downwards [Cooray, 2014]. Rakov and Uman, 2003, ch.1, define a leader as "any self-propagating electrical discharge that creates a channel with a conductivity in the order of 10^4 S m^{-1}". The leader can initiate the formation of several branches as it approaches the ground, and the electric field at the ground surface increases steadily. When the leader reaches an altitude of a few hundred meters above the ground, the electric field at the tips of tall structures on the ground increases. The tips initiate electrical discharges, termed connecting leaders, that propagate towards the stepped leader. If they connect with the stepped leader, the stepped leader has established a connection to the ground [Cooray, 2014]. A wave of potential is then able to travel along the established channel towards the cloud, and is followed by a return stroke. If the return stroke connects to a branch as it approaches the cloud, the charge in the branches is absorbed by the main channel, and the main channel is then illuminated. The currents associated with return strokes have typical duration of a few hundred microseconds [Cooray, 2014].

A cloud flash is likely to begin where the electric field is strongest, along the upper and lower boundaries of the negative charge region. The TGFs observed from space are likely to be produced in association with IC^+ lightning discharges [Mezentsev et al., 2018]. An IC^+ flash starts by negative discharges moving from the negative charge center to the positive charge region (stages a and b in Figure 2.10). The upper level channels then extend horizontally, and charge is transported through a vertical channel from the lower level to the upper level (stages c and d), in association with brief breakdowns in the lower levels. The vertical channel can have a length of a few kilometers. In stage e there are extensions in the lower level channels, before the conductivity of the vertical channel decreases (stage f), and the upper channels are separated from the lower level channels

[Cooray, 2014]. In these later stages of the lightning discharge there are also recoil leaders, where there can be several retraces of the same channel [Rakov and Uman, 2003].

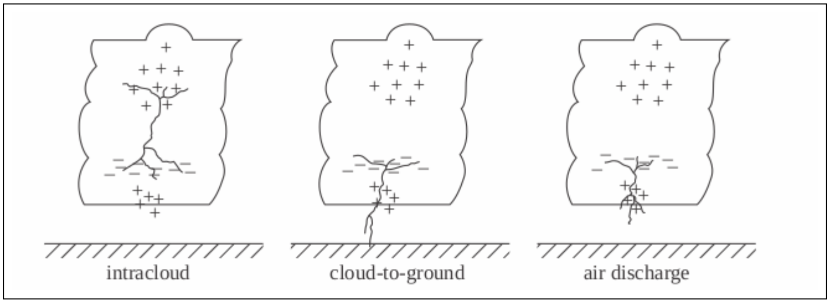

FIGURE 2.9: The lightning types found within the tripole charge structure of a thundercloud. Figure from Cooray, 2014.

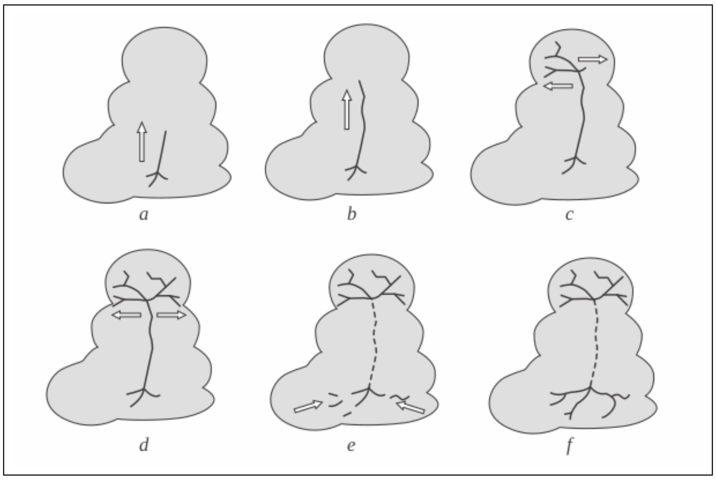

FIGURE 2.10: The mechanisms of an intracloud flash, where the arrows indicate the direction of discharge development. Figure from Cooray, 2014.

Streamers and leaders are essential in the theories of lightning discharges, as well as recoil leaders and return strokes. Streamers are found in front of the leader tips and are associated with lower electrical conductivities. The leader length is typically on the order of kilometers, whereas the streamers found ahead of leader tips are of centimeter length. The air behind the tip of a streamer acts as an insulator, and, as defined by Moss et al., 2006, "streamers are narrow filamentary plasmas, which are driven by highly nonlinear space charge waves. Streamers can exhibit both positive and negative polarities, which is simply defined by the sign of the charge existing in the streamer head". For streamers of negative polarity, electron avalanches from the streamer tip propagate away from the streamer tips, and hence the streamer does not require seed electrons.

As a lightning leader develops in the ambient field of a thundercloud, a strong electric field develops ahead of the leader tip [Skeltved et al., 2017]. The strength of the ambient field depends on the separation of the charge regions in the thundercloud and the amount of charge within the layers. The mean strength of the ambient field between the main charge regions is 0.2 - 0.5 kV/cm [Stolzenburg et al., 2007]. Although the strength of the ambient field is typically below the RREA threshold (subchapter 2.3), the peak strength can exceed the threshold. Marshall and Stolzenburg, 2001, found that the vertical separation of the main charge regions was 2-5 km, and found the potential difference between the charge layers by integrating the field over the vertical extension. The largest potential difference was 132 MV, and occurred between 6.5 and 9.9 km altitude.

The IC leaders are initiated where the ambient field is strongest, and this typically occurs above the main negative charge region. The IC leaders are bidirectional, and as the leaders develop in the ambient electric field, the charges on both ends of the leader increases, whereas the total charge on the leader remains zero. The leader continues to develop in the ambient field until it spans the separation between the charge layers. The IC^+ leaders are stepped leaders, and transport electrons from the main negative charge region to the upper positive charge region [Cummer et al., 2005]. If the leader channel is approximated as perfectly conducting, the induced charges on the surface of the leader align to oppose the ambient field, causing the potential to be uniform at the center of the leader, but accumulating towards the leader tips [Skeltved et al., 2017]. Ahead of the leader tips, streamers will continuously be initiated, as the field in this region is stronger than the conventional breakdown threshold. Liu and Pasko, 2004, found that, because of photoionization effects, acceleration and expansion of streamers causes a reduction in the preionization level ahead of streamers. To account for this reduction, the field at the streamer tips preceding the branching of the streamer can be as large as $10E_k$, where E_k is the conventional breakdown threshold field [Liu and Pasko, 2004]. Modelling results from Moss et al., 2006, indicate that such a high electric field ($10E_k$) can exist in the streamer tip just before branching, and this field can accelerate low energy electrons over the E_c shown in Figure 2.11 to run-away energies.

The strength of the field that can exist ahead of the leader tips is dependent on how fast the potential of a new leader drops, and can only occur for negative stepped leaders during the transient negative corona flash stage, as described by Celestin and Pasko, 2011. They suggested that the production of energetic electrons from the negative leaders will stop when there is significant branching.

2.3 Relativistic runaway electrons

Electrons that are subject to an electric field are, by Lorentz law, subject to a force (F_E) and accelerated through a gas, colliding with neutral gas molecules and atoms. As outlined by Moss et al., 2006, this gives rise to a dynamic friction force, F_D, which opposes the force applied by the electric field. The friction force an electron experiences as it moves through the air (Figure 2.11), as a function of the electron energy, is given by:

$$F_D(\epsilon) = \sum_j N_j \sigma_j(\epsilon) \delta\epsilon_j \tag{2.3}$$

where N_j is the partial density of N_2, O_2 or Ar in air, σ_j is the collision cross section and $\delta\epsilon_j$ denotes the energy loss. The sum is performed over all inelastic collision processes of the gas [Moss et al., 2006].

Figure 2.11 displays the necessary electric fields required, at surface density, to initiate different types of electrical breakdown processes, and the force these fields apply to the electrons. A maximum in the friction force is seen around an electric field of ~260 kV/cm, indicating that in order to have thermal breakdown, the electric field has to exceed 260 kV/cm. Electrons with energies around 100 eV frequently collide with neutral particles, leading to high values of F_D. The corresponding electric field is the thermal runaway threshold (E_c). If a field $E > E_c$ is applied, then $F_E > F_D$, and the electrons gain more energy from the electric field than they lose to collisions [Moss et al., 2006]. Some of the electrons are then able to reach energies above 100 eV, but they have a decreasing probability of collisions, and will accelerate to very high runaway energies. This is believed to occur on very small scales in relation to streamers. If a field $E < E_c$ is applied, then $F_E < F_D$, and the electron energies remain less than 100 eV [Moss et al., 2006].

For conventional breakdown to occur, the electric field has to exceed 32 kV/cm, which occurs for electrons with energies above a few eV. The electrons at 1-2 eV (the sharp peak on the left side of Figure 2.11) result from energy losses caused by excitation of air molecules.

A minimum in the frictional force occurs at the relativistic runaway threshold (E_t ~2 kV/cm), where the electrons have initial energies ~1 MeV. At these electron energies, the electrons have a reduced probability of colliding with neutral particles. When a field stronger than E_t is applied, the electrons will run away.

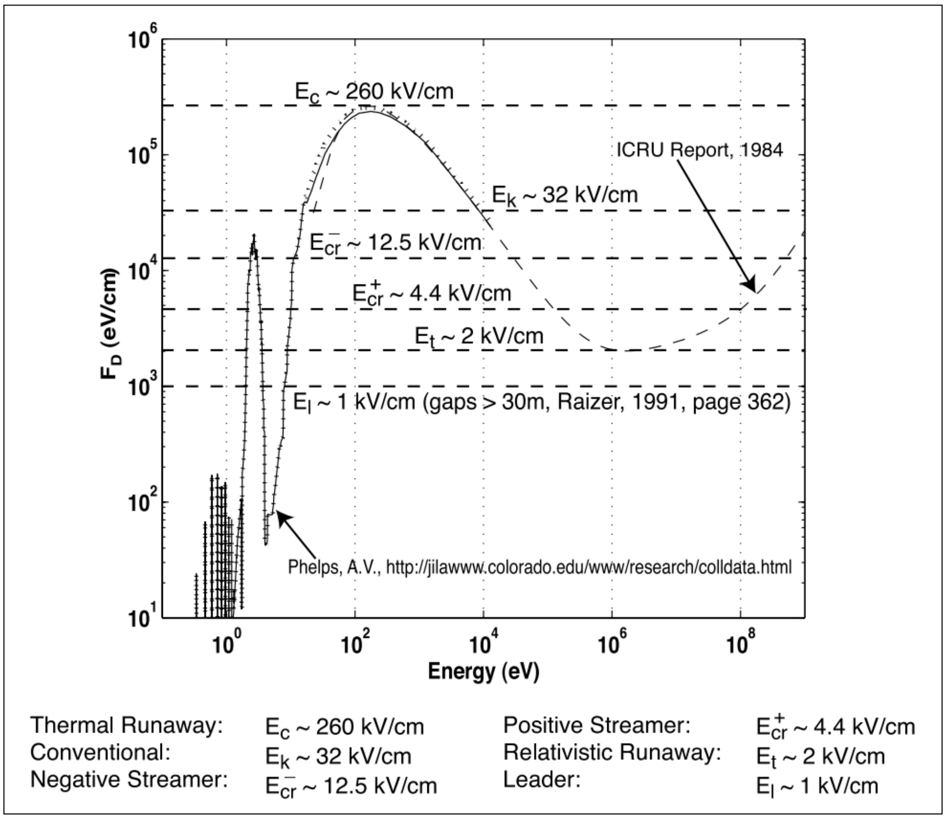

FIGURE 2.11: The friction force experienced by electrons in air, as a function of the electron energy. The solid line gives the force when inelastic collisions are taken into account to correspond to the air mixture of molecules. The dotted line gives the friction force when accounting for the energy losses caused by the dissociation of the N_2 and O_2 molecules. Figure from Moss et al., 2006.

The runaway electron mechanism was first suggested by Wilson, 1924, and occurs when electrons obtain large energies from the static electric fields in the air. The electrons "run away" when the rate of the energy gain exceeds the rate of energy loss due to interactions with particles in the air [Dwyer et al., 2012]. Runaway electrons are produced in fields that are stronger than the ideal break-even field:

$$E_b = 2.18 \times 10^5 V/m \times n \tag{2.4}$$

where n is the scaling factor, given by

$$n = \exp(-\frac{h}{H}) \tag{2.5}$$

where h denotes the altitude above ground and H denotes the scale height, implying that as the air density decreases, the frictional force will also decrease. The initial seed electrons can originate from external sources such as cosmic rays or radioactive decays [Dwyer et al., 2012].

A high-energy electron can trigger avalanche multiplication through ionisation of air molecules in the presence of a field E> E_t. Gurevich et al., 1992, showed that the electrons described by Wilson experience avalanche multiplication when Møller scattering is included. This leads to a large number of runaway electrons from an energetic seed electron, and this mechanism is referred to as the Relativistic Runaway Electron Avalanche (RREA).

If electrons travelled exactly along the electric field lines, $E_{th} = 2.18 \times 10^5 V/M \times n$ would be the threshold for electron propagation and avalanche multiplication [Dwyer et al., 2012]. Due to Coulomb and Møller scattering, there are deviations from the electron trajectories. The secondary electrons from Møller scattering are rarely created along the field lines, and 30% stronger electric fields, giving $E_{th} = 2.84 \times 10^5 V/M \times n$, are therefore needed for electrons to experience avalanche multiplication [Dwyer et al., 2012]. As this threshold is close to the field strength found inside thunderclouds, the RREA mechanism is believed to be common inside thunderclouds.

Since 1992, RREAs have been investigated by different teams, and simulations have been performed to investigate the avalanche length (Figure 2.12), which is the length required for the number of electrons to increase by the number e. Lehtinen et al., 1999, found avalanche rates and the runaway electron energy spectrum by using a Monte Carlo (MC) simulation for calculations of propagation of high energy electrons in both electric and magnetic fields. They excluded bremsstrahlung production and energy losses, but included energy losses from ionization and atomic excitation, as well as Møller scattering and angular diffusion from elastic scattering with atomic nuclei [Dwyer et al., 2012]. Following this simulation, other MC simulations were developed, such as Dwyer's Runaway Electron Avalanche Model (REAM), which included more of the key interactions involving runaway electrons. Celestin and Pasko, 2011, developed a MC simulation using the relativistic binary-encounter-Bethe (RBEB) electron impact model. The differential ionization cross-section of this model resulted in slightly different avalanche rates, compared to the methods based on the Møller scattering cross sections. Celestin and Pasko, 2011, excluded photons and positrons in their simulation, although photons are important in the avalanche development in low fields. The different simulations show similar results for a broad range of field strengths.

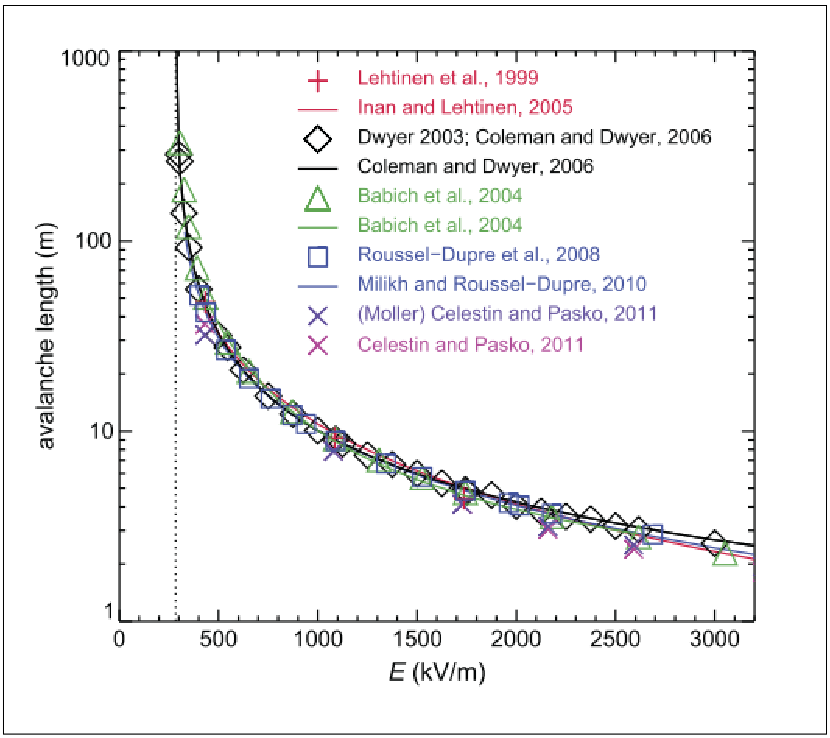

FIGURE 2.12: Different calculations of the avalanche length as a function of the electric field. Figure from Dwyer et al., 2012.

RREAs can occur for both cosmic ray electrons and electrons from cold runaway. As outlined in Dwyer et al., 2012, the flux (F_0) of the external seed particles (e.g. cosmic rays) that run away can be within the range 100-10 000 $m^{-2}s^{-1}$, depending on geographic location and altitude. The flux at the end of the avalanche region is given by:

$$F_{RREA} = F_0 exp(\xi), \; where \; \xi = \int_0^L \frac{dz}{\lambda} \tag{2.6}$$

where ξ is the number of e-folding lengths. For a uniform field, $\xi = L/\lambda$. The flux at the end of the avalanche is thus:

$$F_{RREA} = F_0 exp(\frac{L}{\lambda}) \tag{2.7}$$

The avalanche length can also be approximated by:

$$\lambda \approx \frac{7.3MeV}{eE - F_d} \tag{2.8}$$

where F_d = 0.276 MeV/m×n (n is the scaling factor), and is, as defined by Dwyer et al., 2012, approximately the rate of energy loss the minimum ionizing electrons experience along the avalanche direction.

The secondary electrons lose energy in the atmosphere through ionisation and bremsstrahlung, and thus have a finite range (mean free path length) in the absence of an electric field, before recombining with air molecules [Lindy et al., 2014]. Figure 2.13 shows the range of electrons in air under fair-weather conditions at different production altitudes. For an electron with energy ∼1 MeV, the range in air would be up to ∼10 m for production altitudes of 8-12 km.

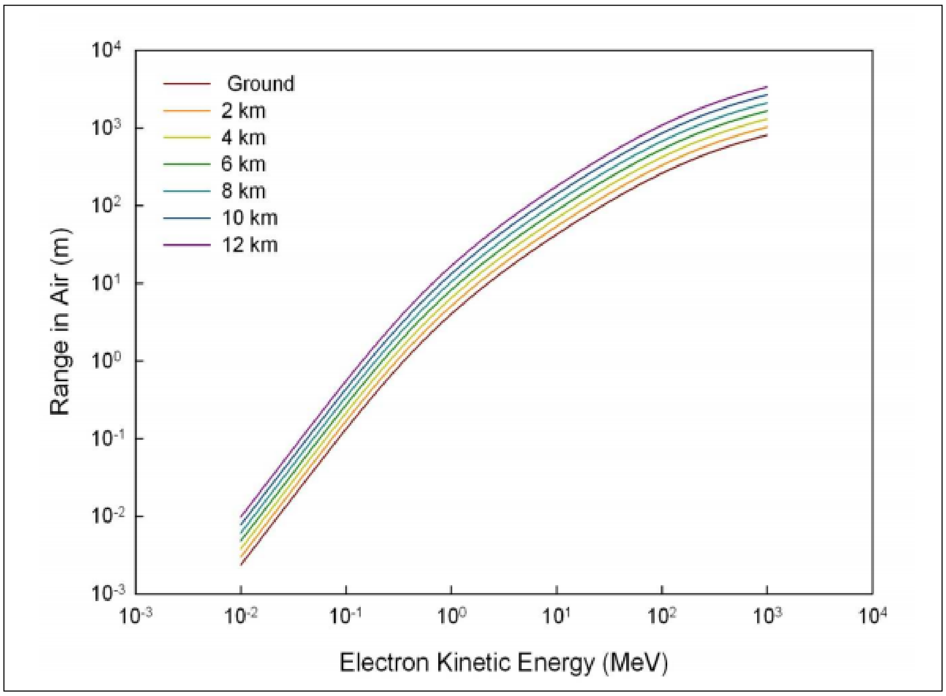

FIGURE 2.13: The range of electrons in air at various altitudes, under fair-weather conditions. Figure from Lindy et al., 2014.

2.4 The relativistic feedback mechanism

Dwyer, 2003, proposed the relativistic feedback mechanism (Figure 2.14), which can account for the large fluences and short durations of TGFs. This mechanism takes into account feedback effects from positrons and energetic photons, and shows how bremsstrahlung X-rays are emitted by runaway electrons that either Compton backscatter or pair-produce in the air [Dwyer et al., 2012]. The left avalanche in Figure 2.14 shows the X-ray feedback (dashed line) and the right avalanche illustrates the positron feedback mechanism (red non-solid line). A backscattered photon that propagates to the beginning of the avalanche region, where it produces more runaway electrons, will produce another avalanche. The positrons could also change direction and run away in the opposite direction relative to the electrons. The positrons might then produce more runaway electrons through the process of Bhabha scattering to produce secondary avalanches. The secondary avalanches can in turn lead to the emission of more X-rays that will experience Compton scattering or pair-production, increasing the number of avalanches [Dwyer et al., 2012].

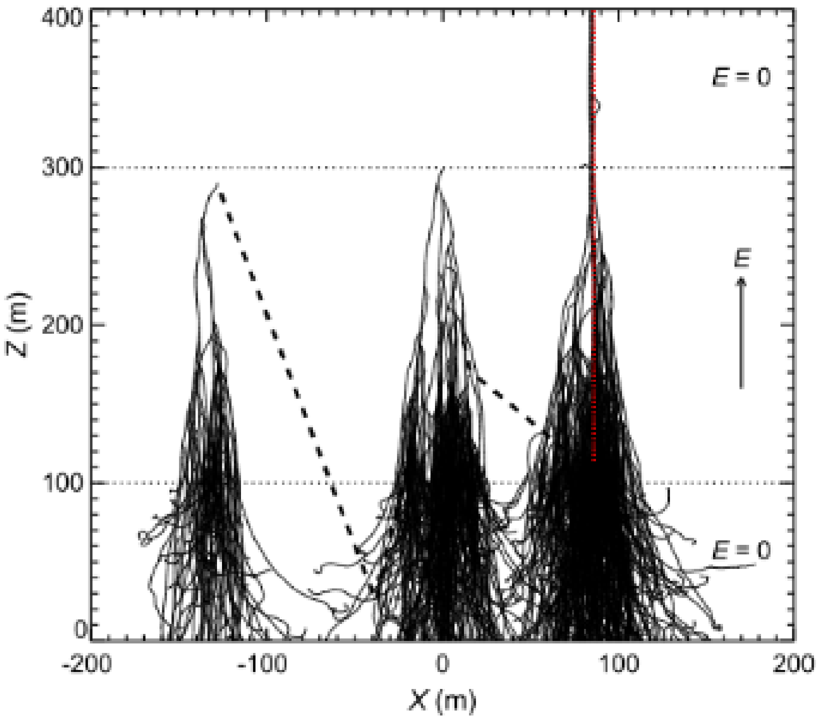

FIGURE 2.14: Illustration of the relativistic feedback mechanism, including Monte Carlo simulation. The dashed lines are X-rays, the thinnest tracks are the runaway electrons and the non-solid red line indicates a positron. Figure from Dwyer, 2003.

The feedback factor, γ, gives the fractional change in runaway electrons during each feedback cycle [Dwyer et al., 2012]. If $\gamma < 1$, the flux of the runaway electrons is enhanced by the factor:

$$F_{RREA} = \frac{F_0 exp(\xi)}{1 - \gamma} \tag{2.9}$$

where ξ gives the number of e-folding lengths. $\frac{F_0}{(1-\gamma)}$ gives the flux of the seed runaway electrons from cosmic rays and relativistic feedback [Dwyer et al., 2012]. If the field increases due to thundercloud charging and the feedback factor approaches 1, the relativistic feedback dominates over external seed particles. RREAs can also cause γ to exceed 1 in parts of the avalanche region. The flux of the runaway electrons when the relativistic feedback mechanism dominates the seed particle production is given by:

$$F_{RF} \propto exp(\xi)\gamma^{t/\tau_{fb}} = exp(\xi)exp(t/\tau') \tag{2.10}$$

where

$$\tau' = \tau_{fb}/ln(\gamma) \tag{2.11}$$

The feedback factor can exceed 1 if the electric field increases rapidly, before the system counteracts with a large discharge current. This can, as outlined by Dwyer et al., 2012, occur during large-scale charging of a thundercloud or in association with charge motion during lightning. The feedback factor can also exceed 1 in parts of the avalanche region due to currents caused by runaway electrons. The feedback time, τ_{fb}, is defined as the time runaway electrons and backward propagating positrons or X-rays need to complete a trip within the avalanche region [Dwyer et al., 2012]. Modelling results for E>500 kV/m, for an electric field region of length L<340 m, gives τ_{fb} <3μs [Dwyer, 2003]. As outlined by Dwyer et al., 2012, the number of runaway electrons increase by a factor γ during the feedback cycle. The flux of the seed runaway electrons quickly originates from the feedback process alone. A rapid increase in runaway avalanches results in a very large flux of runaway electrons and high numbers of accompanying X-rays.

2.5 Comparison of mechanisms

The mechanisms proposed (Figure 2.15) for the generation of high energy electrons in the atmosphere have evolved from the runaway electron mechanism, to the RREA and relativistic feedback mechanisms, taking new processes that the previous mechanisms did not include, into account. The feedback mechanism only requires one seed electron, and this seed could be either a cosmic particle or a thermal runaway electron. Thermal runaway can give $10^{10} - 10^{12}$ seed particles, and by the inclusion of Møller scattering to get RREA, the number of seed electrons can increase further by 10^5. If the feedback factor γ <1, the relativistic feedback mechanism is equivalent to the RREA mechanism [Dwyer et al., 2012].

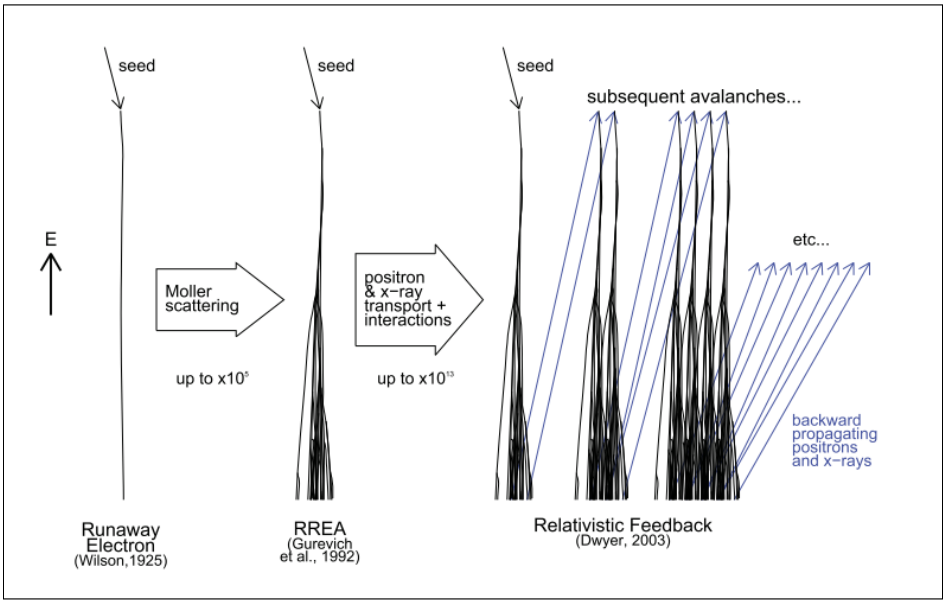

FIGURE 2.15: Summary of the three mechanisms; runaway electron, RREA and relativistic feedback. Figure from Dwyer et al., 2012.

2.6 Particle interactions

2.6.1 Ionisation processes in the air

Ionisation processes can cause an increase in the concentration of electrons in the air. An electron will gain energy in the presence of an electric field, but during collisions with atoms in a medium the electron is only able to transfer a quantum of its energy [Cooray, 2014]. The electron energy eventually exceeds the excitation energy of the colliding atom, and will be left in an excited state after a collision. If the electron energy exceeds the atom's ionisation energy, which is the minimum energy needed to free an electron, the atom could be left ionized after a collision. The probability of ionisation is given by:

$$P_{ion} = \frac{\sigma_{ion}}{\sigma} \tag{2.12}$$

where σ_{ion} is the microscopic cross section for ionisation, and σ is the total collision cross section [Cooray, 2014]. The collisional cross section can be found for elastic collisions, inelastic collisions and excitation collisions, and is given by:

$$\sigma_t = \sigma_e + \sigma_{ex} + \sigma_{ion} + \sigma_a + \sigma_{oth} \tag{2.13}$$

where σ_e is the cross section of elastic collisions, σ_{ex} the cross section of excitation collisions, σ_{ion} the cross section for ionisation, σ_a the cross section of attachment and σ_{oth} the cross section for any other processes [Cooray, 2014].

The probability of ionisation is proportional to the ionisation cross section (Figure 2.16), and increases with the electron energy. It reaches a peak around 100 eV, before it starts to decline. This decline can be attributed to the limited time available for interaction of the electron and an atom, such that the electron can pass by the atom closely without ejecting an electron from it [Cooray, 2014].

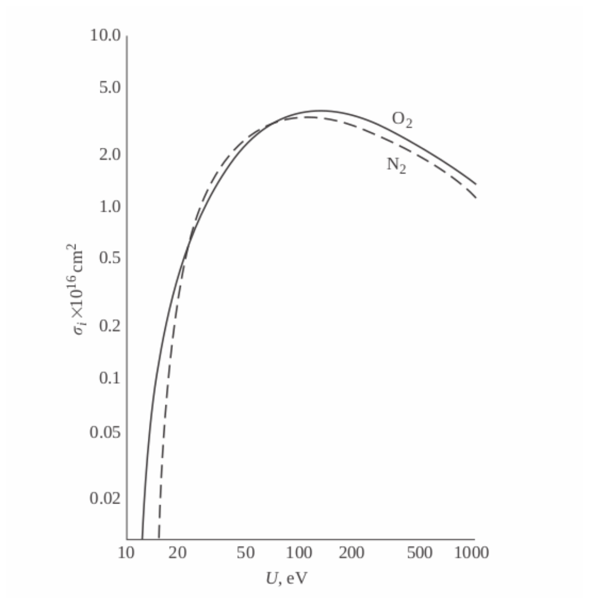

FIGURE 2.16: Ionisation cross section, σ_i, as a function of the electron energy, for electrons colliding with O_2 and N_2. Figure from Cooray, 2014.

Energetic electrons propagating through the air experience scattering processes, including Møller and Bhabha scattering, which only include electrons/positrons and (virtual) photons. In these processes, fermions (leptons) experience a bosonic exchange via the photon propagator. Møller scattering is the process of electron by electron (or positron by positron) scattering, whereas Bhabha scattering is electron by positron scattering. Møller scattering is described by two topologically different Feynman diagrams (Figure 2.17), where the two final electrons have different properties. The electron pairs (or positron pairs) involved in Møller scattering are indistinguishable, and hence the amplitudes for the two diagrams have to be subtracted. The Bhabha scattering is also given by two topologically different Feynman diagrams (Figure 2.18) that have to be subtracted (due to the Pauli exclusion principle), and the particles involved in Bhabha scattering can be distinguished by their charge. This is performed to find the amplitude and the cross section. The cross sections depend on the scattering angle, θ, and on the energy of the two electrons. The cross section for Møller scattering in the case of large energies, where $E \gg m_e c^2$, is given by:

$$\frac{d\sigma}{d\Omega} = \frac{\alpha^2}{E^2}(\hbar c)^2 f(\theta) \tag{2.14}$$

where E is the energy of one of the two leptons in the center of mass, α is the fine structure constant and $f(\theta)$ is a function of the scattering angle. At very high energies, the lepton mass does not affect the cross section [Henley and Garcia, 2007].

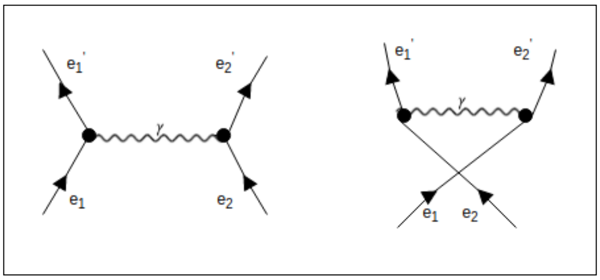

FIGURE 2.17: Feynman diagrams of Møller scattering, adapted from Henley and Garcia, 2007. The time arrow is upwards, and the electrons are labelled 1 and 2 because of their different momenta and spin.

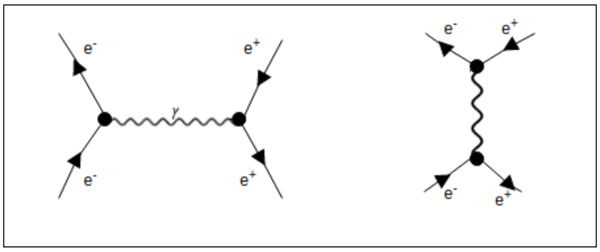

FIGURE 2.18: Feynman diagrams for Bhabha scattering, adapted from Henley and Garcia, 2007.

2.6.2 X- and γ-rays in the atmosphere

X-rays propagating through the air experience mainly three processes; the photoelectric effect, Compton scattering and pair production (Figure 2.19).

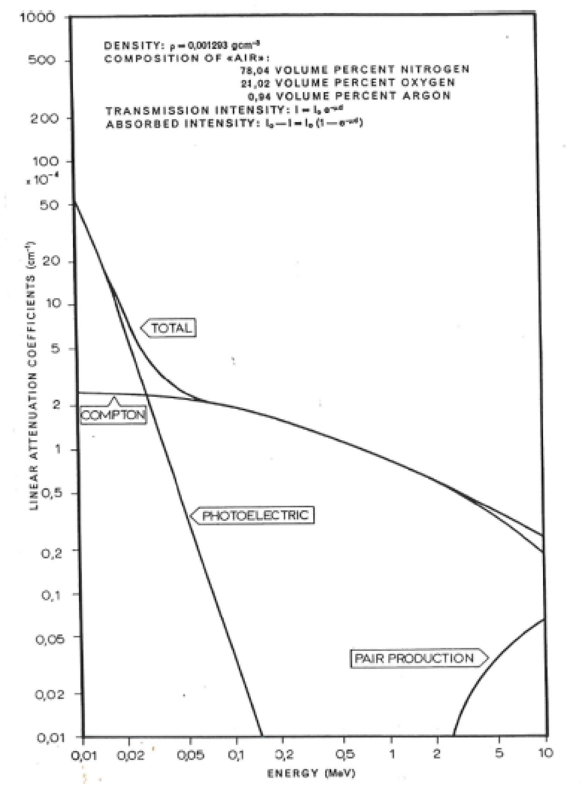

Figure 2.19: The linear attenuation coefficient for X-rays in the air at ground level at STP, showing the different processes X-rays experience in the air [*Phys252: Measurements of Auroral X-rays*].

Bremsstrahlung

Charged particles that are accelerated emit electromagnetic radiation. X-rays are emitted during the process of bremsstrahlung, which occurs when energetic electrons are decelerated after being deflected in the field of an atomic nucleus [*Phys252: Measurements of Auroral X-rays*]. This interaction causes the electron to lose energy, which is converted into electromagnetic radiation, in form of photons. The number of photons per unit energy interval emitted per electron is given by:

$$\frac{dn}{dE_x} = 1.4 \times 10^{-8} Z(\frac{E_e}{E_x} - 1) \tag{2.15}$$

where E_e is the electron kinetic energy and Z is the average atomic number of the particles in the material. The value of Z is typically set to 7.2 for air, as it consists of mainly nitrogen and oxygen [*Phys252: Measurements of Auroral X-rays*]. Equation 2.15 shows that the photon flux decreases with increasing photon energy, before the photon energy is equal to the electron kinetic energy. The spectrum of bremsstrahlung X-rays is therefore continuous for energies $E_x < E_e$, but the spectrum is heavily skewed towards lower energies, as most of the electrons are decelerated through series of collisions where smaller amounts of energy are lost [Cember and Johnson, 2009].

Lehtinen et al., 1996, reported that the energy distribution of the TGF photons could be explained by an attenuated bremsstrahlung spectrum. The attenuated spectrum indicates that the sources of these photons are high-energy electrons (>10 keV). To obtain the large number of electrons, the high-energy electrons must be in a region with a strong electric field, such as the strong fields near the streamer tips [Skeltved et al., 2017].

In order to obtain the bremsstrahlung spectrum of TGFs, the RREA energy distribution is required to reach a steady state where the maximum energies are greater than that of the TGFs [Skeltved et al., 2017].

Photoelectric effect

The photoelectric effect dominates at lower energies, and is significant up to 50 keV for X-rays in the air. An incoming X-ray photon interacts with the atom, transferring its energy to an electron from the K-shell of the atom (Figure 2.20). The photon is then fully absorbed in the collision [*Phys252: Measurements of Auroral X-rays*]. The energy of the emitted electron is given by:

$$E_k = h\nu - E_b \tag{2.16}$$

where E_b is the binding energy of the electron, which is the energy needed to free an electron from an atomic nucleus. The binding energy is also often referred to as the ionisation energy. The cross section decreases rapidly with increasing photon energy.

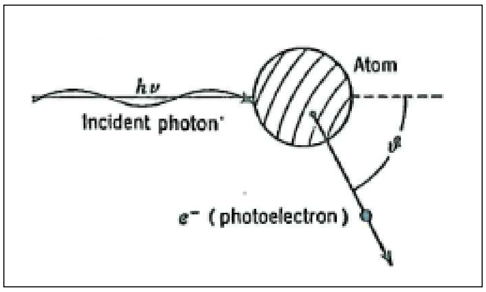

FIGURE 2.20: Illustration of the photoelectric effect, showing an incoming photon freeing an electron from the K-shell of the atom. Figure from Thorsteinsen, 1995.

Compton scattering

In Compton scattering (Figure 2.21), the incoming X-ray reacts with one of the orbital electrons of the atom. These electrons are the most loosely bound electrons in the material, and the electrons can thus be considered as "free". The electron is considered a free electron if the energy of the incoming photon, $h\nu$ is much larger than the binding energy of the electron, and the collision is then elastic [Thorsteinsen, 1995]. The scattered electron has less energy after the collision, and the shift in wavelength of the scattered photon is given by:

$$\Delta\lambda = \lambda' - \lambda = \frac{h}{m_0 c}(1 - cos\theta) \tag{2.17}$$

where $\frac{h}{m_0 c} = 0.02426$ nm, which is referred to as the Compton wavelength of the electron. The maximum wavelength shift is in the case of backward scattering, when $\theta = \pi$.

The electron is considered to be at rest before the Compton scattering. The incoming photon has $E = h\nu$, and $p = h\nu/c$. By conservation of energy and momentum:

$$\begin{aligned} p = \frac{h\nu}{c} = \frac{h\nu'}{c}\cos(\theta) + p_e \cos(\phi) E = h\nu = E' + E_K = h\nu' + E_K \\ p_e c = \sqrt{E_K(E_K + 2m_e c^2} \end{aligned} \tag{2.18}$$

where E_K is the kinetic energy of the electron, m_e is the restmass and p_e is the momentum.

The energy of the scattered photon is given by:

$$E' = h\nu' = \frac{h\nu}{1 + \epsilon(1 - \cos(\theta)} = \frac{E}{1 + \epsilon(1 - \cos(\theta))} \tag{2.19}$$

where $\epsilon = \frac{E}{m_e c^2} = \frac{h\nu}{m_e c^2}$, as outlined in Thorsteinsen, 1995. The kinetic energy of the electron can then be written as:

$$E_K = \frac{\epsilon(1 - \cos(\theta))h\nu}{1 + \epsilon(1 - \cos(\theta))} = \frac{\epsilon(1 - \cos(\theta))E}{1 + \epsilon(1 - \cos(\theta))} \tag{2.20}$$

The scattered electron is likely to deposit energy locally, and the energy transferred to the electron increases with photon energy. Some of this energy is not deposited locally, and is converted to X-rays.

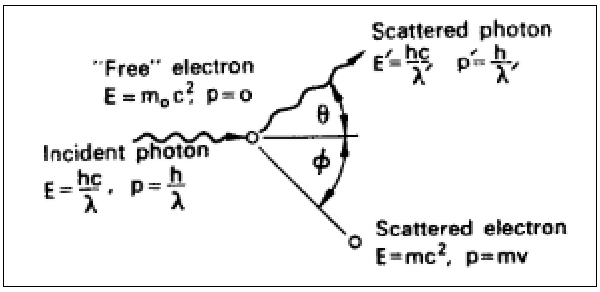

FIGURE 2.21: Illustration of Compton scattering, where the incoming photon scatters on the atom's orbital electron. Figure from Cember and Johnson, 2009.

Pair production

In pair-production (Figure 2.22), a photon produces an electron-positron pair in the Coulomb-field of a nucleus. The rest mass of the electron and the positron is given by:

$$m_e c^2 = 0.511 MeV \tag{2.21}$$

and a photon energy $h\nu > 1.022$ MeV is required to enable pair-production. The particles deposit most of their kinetic energy locally, but when the positron has lost nearly all of its kinetic energy it will be absorbed by an electron. The electron-positron pair then annihilates, and produces two photons with energies 0.511 MeV, in order to obey the conservation of momentum. The photons produced have an finite probability of being able to escape the collisional area [Thorsteinsen, 1995].

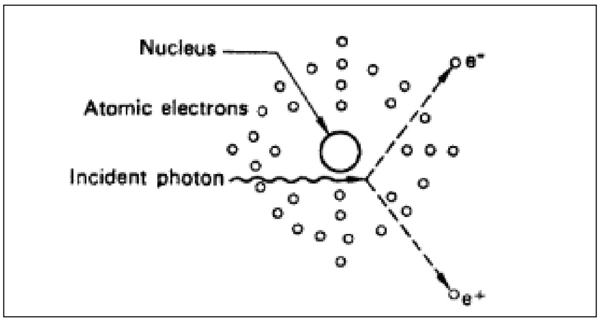

FIGURE 2.22: Illustration of pair-production in the Coulomb-field of a nucleus. Figure from Cember and Johnson, 2009.

Chapter 3

Data and Instrumentation

This chapter outlines the different platforms that have been used to observe TGFs from space. The chapter also focuses on the ground-based lightning networks used for finding lightning associations to the detected TGFs.

3.1 BATSE

BATSE was launched in April 1991, and mounted on NASA's CGR Observatory. As the CGR Observatory flew in a low-Earth orbit, half of the detectors always pointed downwards. The orbit had an initial altitude of 450 km, which was decreased to ∼410 km in 1992, and an orbital inclination of 28.5°. BATSE was removed from its orbit in 2000.

The first discoveries of TGFs were made by BATSE [Fishman et al., 1994], although the main objective of BATSE was to observe cosmic gamma-ray bursts. Over the course of nine years, BATSE observed 78 TGFs. BATSE consisted of eight detector modules, each containing a large-area detector (LAD) and a spectroscopy detector (SD). The data presented in the first BATSE catalog contained data from the LADs, which were NaI scintillators with a diameter of ∼50 cm and a thickness of ∼1.3 cm. The photons detected were analyzed into 128 energy channels, and covered an energy range of 25 keV - 2 MeV [Fishman et al., 1994].

The duration of a gamma-ray burst is typically a few seconds, but the duration of the TGFs observed by BATSE were typically on millisecond scale (Figure 3.1). As BATSE was a triggered instrument, it returned data when the algorithm detected a significant increase in the count rate above background time scales. The long trigger window (64 ms) prevented the detection of faint TGFs [Dwyer et al., 2012]. The burst triggering was disabled during the passage through the South Atlantic Anomaly (SAA), due to the high amount of energetic protons in this region. The use of a time-tagged event (TTE) format resulted in an accuracy of 2 μs for the arrival time of each count in the LADs [Dwyer et al., 2012].

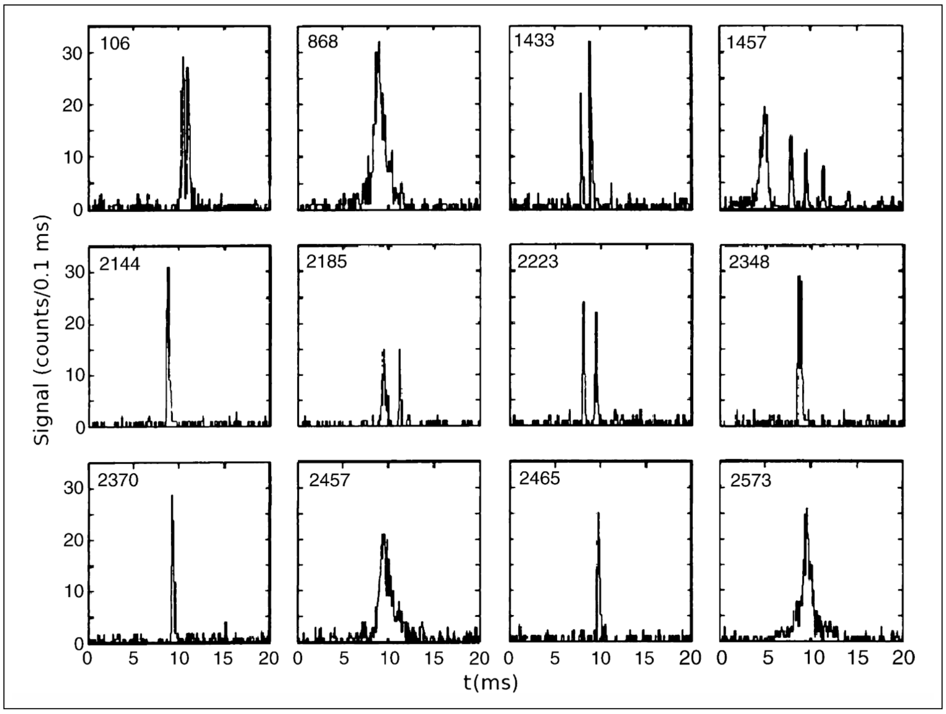

FIGURE 3.1: TGFs detected by BATSE. Figure from Dwyer et al., 2012 (adapted from Fishman et al., 1994).

3.2 RHESSI

RHESSI was launched in 2002 into an orbit of altitude 580 km and 38° inclination. RHESSI showed that TGFs are more frequent than indicated by the BATSE observations. In comparison with BATSE, the spectral resolution was improved and allowed for more detailed analysis of the events. There was a decrease in the sensitivity of the detectors after 2006, due to radiation damage [Grefenstette et al., 2009], causing a decrease in the number of TGFs detected. Before this decrease, RHESSI observed, on average, one TGF every 2.35 days. RHESSI was decommissioned in August 2018.

RHESSI was built for detection of solar flares, and contained nine high-resolution germanium detectors. These were divided into front and rear segments, and the events collected at the different segments were read out by separate electronics [Grefenstette et al., 2009]. The germanium detectors had a cylindrical shape, with a diameter of 7.1 cm diameter and length of 8.5 cm. The top of the detectors, as well as the curved outer part, was covered by a thin boron layer (with a thickness of ∼0.3 μs), to have a surface transparent down to 3 keV X-rays. The energy resolution of the germanium detector segments and the range in which they could view the whole sky is given in Table 3.1. The high energy resolution of RHESSI allowed for the lines of solar gamma-rays to be resolved, and also allowed for the separation of thermal and non-thermal X-rays [Smith et al., 2002]. Photons that experienced Compton scattering from one segment to another would result in two counts being observed at the same time. Combining the energies of these two photons to find the energy of the original photon allowed for the recording of energies that exceeded 20 MeV. For the first RHESSI catalog, only data from the active rear segments were used, as they had larger volumes and the front segment detectors were occasionally switched off when the sun was behind the horizon [Grefenstette et al., 2009]. Figure 3.2 shows the effective area of the rear segments of the instrument as a function of energy. It shows the average response to photons hitting the detectors from random directions [Grefenstette et al., 2009].

Table 3.1: Properties of the front and rear segments of RHESSI detectors

Segments	**Energy range**	**Energy resolution**
Front segments	25 keV - 17 MeV	∼1 keV FWHM (low-energy cutoff at ∼2.7 keV)
Rear segments	3 keV - 2.7 MeV	>3 keV FWHM

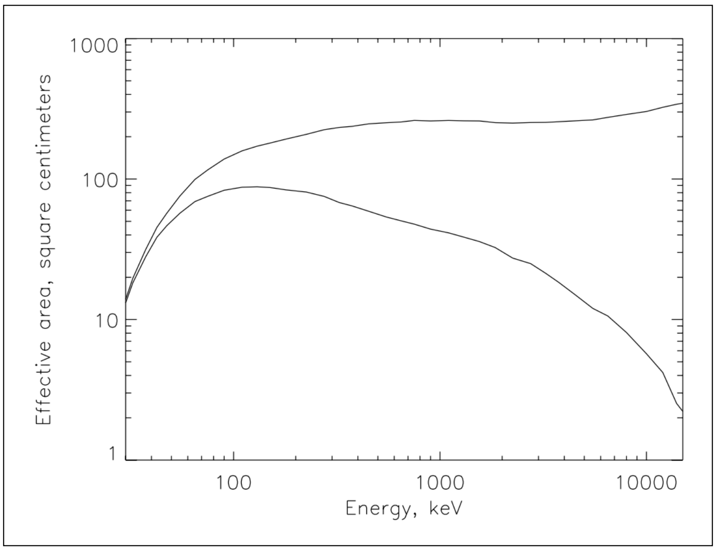

Figure 3.2: The top curve shows the effective area for isotropic input photons for any interaction. The bottom curve shows the effective area for photons that deposit all their energy in detectors. Figure from Grefenstette et al., 2009.

The time resolution of the RHESSI data was 0.95 μs, but RHESSI had a systematic clock offset of 1.8 ms. This was resolved by Mezentsev et al., 2016, down to an accuracy of 100 μs, by analysing the detected TGFs with World Wide Lightning Location Network (WWLLN) sources and magnetic field recordings [Mezentsev et al., 2016]. For the first RHESSI catalog, the time series were collected in bins of 1 ms, and a recording was considered a potential TGF if the number of counts exceeded the background by at least 12σ counts. Here σ denotes the variation of the background and is determined by $\sigma \approx \sqrt{N+1}$, where N gives the average number of background counts per ms in a 300 ms block [Grefenstette et al., 2009].

RHESSI used continuous data acquisition, and telemetered all the data to the ground for further processing. An exception to the continuous data flow was when RHESSI passed through the SAA. The data mode was also interrupted when RHESSI passed through regions of high magnetic latitude, where the instruments would be affected by the highly energetic electrons from the outer radiation belt [Grefenstette et al., 2009].

The second RHESSI catalog, being used for this thesis, contains TGFs detected between 2002 and 2015, according to the algorithm described by Gjesteland et al., 2012. In this search algorithm, only counts with energies exceeding 30 keV were considered. There were different steps for identifying the RHESSI TGFs:

1. Using a triggering window of 1 ms. This covers the typical duration of TGFs
2. Calculating the background counts for a trigger window, and finding the probability of false events
3. Using a fine search algorithm, where events with substantially varying background levels were eliminated:
    - Checking the duration of the trigger, eliminating e.g. cosmic ray detection and possible TGF electron beam detections
    - Eliminating false triggers caused by high voltage arcing
    - Placing constraints on the hardness ratio, defined as

      $$H_r = \frac{Number\, of\, counts\, with\, energy > 1MeV}{Number\, of\, counts\, with\, energy < 1MeV} \tag{3.1}$$

      such that triggers with values of $H_r < 0.025$ were rejected
    - Removing triggers with an excessive amount of overflow counts (to remove cosmic rays)

This algorithm applied by Gjesteland et al., 2012, more than doubled the number of detected TGFs by RHESSI.

3.3 Fermi

Fermi was launched in 2008 into an orbit of altitude 565 km and an orbital inclination of 25.6° [Roberts et al., 2018]. The satellite's orbital inclination causes it to spend a large amount of time over the tropical regions, where thunderstorms are most prevalent.

Fermi has two instruments for gamma-ray observations, the Large Area Telescope (LAT) and the Gamma-ray Burst Monitor (GBM). The energy ranges of these instruments are shown in Table 3.2. The primary goal of GBM is to measure gamma-ray bursts. GBM consists of 12 NaI scintillators and two BGO scintillators. The effective area of the BGO scintillators is ~160 cm^2 for energies greater than 300 keV. The BGOs are placed on opposite sides of the spacecraft, in order for the bursts above the horizon to be visible to at least one of the detectors [Meegan et al., 2009]. The properties of the NaI and BGO scintillators are given in Table 3.3. The NaI scintillators are oriented in various directions to enable it to view a larger fraction of the sky, to specify the locations of the observed gamma-ray bursts. The BGOs are most significant for detecting TGFs, because of their energy response and range. Unlike the NaI scintillators, the BGOs respond well to high-energy γ-rays.

Table 3.2: Properties of Fermi instruments

Instrument	**Energy range**
LAT	20 MeV to >300 GeV
GBM	8 keV - 40 MeV

PMTs are used for converting the BGO scintillation light into electronic signals (Figure 3.3). A Data Processing Unit (DPU) receives the signals from the PMTs, and they are then processed and formatted for transmission.

Table 3.3: Properties of GBM detectors

Detector	**Dimensions**	**Energy range**
NaI scintillator	12.7 cm diameter 1.27 cm thickness	8 keV - 1 MeV
BGO scintillator	12.7 cm diameter 12.7 cm length	200 keV - 40 MeV

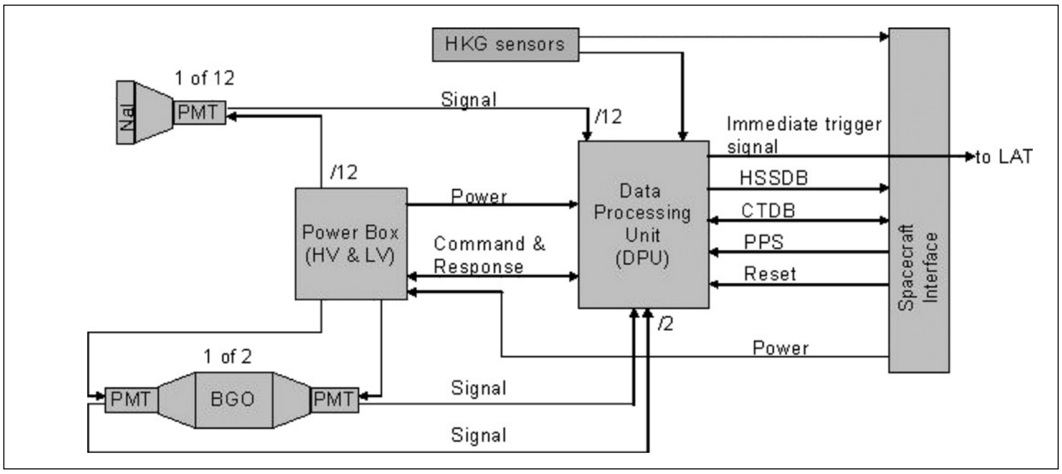

FIGURE 3.3: Functional block diagram of GBM. Figure from Meegan et al., 2009.

TGFs are detected in two different modes by GBM; an online and an off-line search. The online search is performed in real-time onboard the spacecraft, and the offline search is performed on the ground. When the flight software detects an increase in the count rates of at least two of the NaI scintillators, a burst trigger occurs. The increase has to exceed the background level determined by the preceding seconds of data (excluding the most recent 4 s). After a fixed time (typically about 300 s), TTE data is terminated and the TTE buffer restarts [Briggs et al., 2010]. TTE is the data type of GBM that is most significant for TGF observations. For TTE data, individual counts in the GBM detectors are time-tagged, giving a temporal resolution of 2 μs and a nominal dead-time of 2.6 μs [Roberts et al., 2018]. This dead-time increases to 10.4 μs when events are registered in overflow channels of the scintillators. The dead-time in an overflow count in one detector does not affect the dead-time of the other detectors. Overlapping pulses have been observed to have altered energy counts depending on whether peak or tail pileup is significant [Roberts et al., 2018]. Dead-time is a a common problem for TGF detectors, and occurs when the detector is prevented from reacting to incoming pulses because it is still processing previous events.

The GBM detectors operate continuously, except when passing through the SAA. The GBM data is telemetered to the ground in coarsely time-binned continuous data, and the data volume is increased when the flight software detects an event of interest [Briggs et al., 2010]. Similar to BATSE, Fermi uses a trigger process for gathering TGF data. The trigger algorithm was modified in 2010, such that there was continuous data acquisition over the regions likely to have high TGF activity [Briggs et al., 2013]. This continuous data acquisition was powered on when Fermi passed through one of these regions (Figure 3.4). The data acquisition method of Fermi also took into account seasonal variations, by using continuous data acquisition for summer thunderstorm seasons. In 2012, the continuous data acquisition was modified to include the entire orbit (with the exception of the SAA).

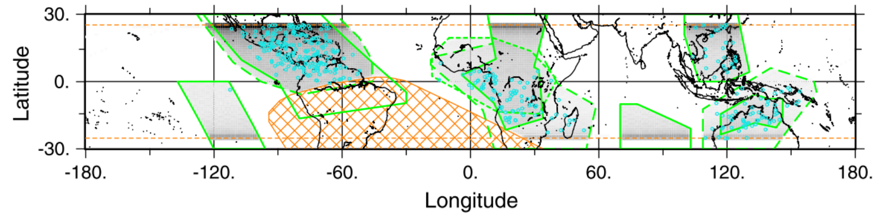

FIGURE 3.4: The boundaries of the regions used for continuous data acquisition by Fermi are given by the green lines. The orange grid region depicts the SAA. Figure from Briggs et al., 2013.

The trigger window was 16 ms for both the NaI scintillators and the BGOs before the data acquisition was modified. The trigger interval was much longer than the typical duration of TGFs, and would reduce the significance of the signal. The flight software was updated in 2009 to include the BGO rates in the trigger algorithms. The subsequent updates in data acquisiton in 2010 and 2012 (Figure 3.5) increased the detection rate of TGFs [Briggs et al., 2010].

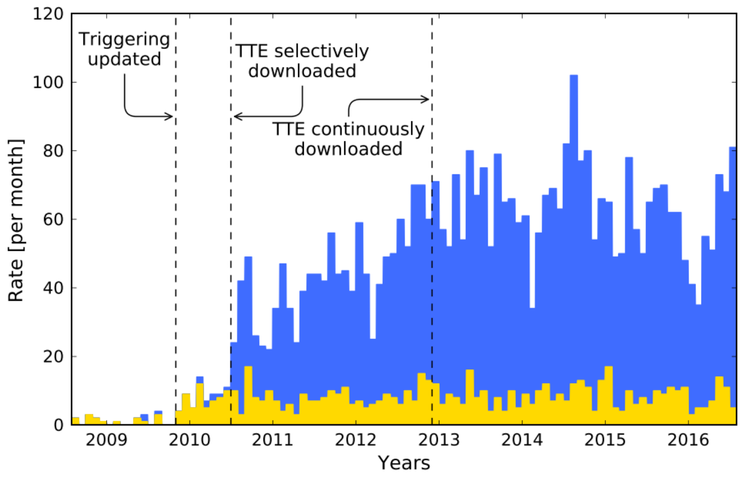

FIGURE 3.5: Plot of the evolution of the TGF detection rate of the GBM. The online triggered mode is shown as yellow, and the offline search mode as blue. Figure from Roberts et al., 2018.

The Fermi catalog used for this thesis was provided by `https://fermi.gsfc.nasa.gov/ssc/data/access/gbm/tgf/`, and contains TGFs detected between July 2008 and July 2013.

3.4 AGILE

AGILE was launched in 2007 into an orbit with an average altitude of ∼535 km and an orbital inclination of 2.5°, and uses a trigger algorithm [Tavani et al., 2009; Marisaldi et al., 2013]. The altitude of the orbit decreases with time, due to atmospheric drag. The main objective of AGILE is to do astrophysical observations in the range 30 MeV - 30 GeV, and X-ray observations in the range 18 - 60 keV.

The scientific payload of AGILE consists of different instruments:

1. A Tungsten-Silicon tracker for gamma-ray imaging in the range 30 MeV - 30 GeV
2. An X-ray detector (silicon-based), for imaging in the range 30 MeV - 30 GeV
3. A mini-calorimeter (MCAL), consisting of 30 scintillator bars, for gamma-ray detections in the energy range 300 keV to 100 MeV. The energy resolution for a typical MCAL bar is ∼14% FWHM at 1.275 MeV for un-collimated events [Labanti et al., 2009; Marisaldi et al., 2015]
4. An anticoincidence system to shield the payload from charged particles from cosmic sources and reduce the detection of noise

Most of the AGILE TGFs are detected by MCAL. The instrument consists of 30 CsI scintillator bars of dimensions $15 \times 23 \times 375$ mm^3. The bars are placed in two orthogonal layers, resulting in a total thickness of 1.5 radiation lengths. MCAL has a time resolution of 2 μs. The contributors to the instrumental dead-time effects of MCAL are the scintillators' processing time, dead-time caused by the anticoincidence (AC) shield and count queuing before the Data Head Unit (DHU). The most significant contribution to the dead-time is from the AC shield [Marisaldi et al., 2013].

MCAL can operate in two different modes; a GRID mode and a BURST mode. The GRID operative mode is used for event selection and energy construction [Marisaldi et al., 2013]. The BURST mode operates in the energy range 350 keV to 100 MeV, and the onboard trigger logic of this mode operates over four time ranges. As described by Marisaldi et al., 2013, when MCAL detects a trigger, the instrument telemeters the data photon-by-photon for several seconds around the trigger time. The telemetered data also contains information about photon energy.

AGILE's selection algorithm is based on the use of a moving time window of 1 ms duration, searching for clusters. A cluster occurs when the time window contains at least 6 counts. A cluster will include all counts that are 300 μs from the previous count. The clusters are then processed further, and in order for a cluster to be classified as a TGF, it has to pass several criteria, as outlined by Marisaldi et al., 2013:

1. The cluster has to contain at least 10 counts
2. The trigger has to be found within 20 ms of the cluster starting time
3. The following constraint is placed on the hardness ratio:

$$H_r = \frac{Number\,of\,counts\,with\,energy\ \geq\ 1.4\,MeV}{Number\,of\,counts\,with\,energy\ \leq\ 1.4\,MeV} \leq 0.05 \tag{3.2}$$

4. The maximum photon energy has to be ≤30 MeV
5. Each quadrant of MCAL has to register at least one count

TGFs between March 2015 and September 2018, from the 3rd AGILE TGF catalog [Lindanger et al., 2020; Maiorana et al., 2020], were used for this thesis. This data was recorded after an on-board configuration of AGILE, dealing with the dead-time of the AC shield. The configuration was made to disable the AC shield's "veto signal", with the purpose of increasing the discovery rate of TGFs. As a result of the on-board configuration, the number of TGFs detected increased by an order of magnitude. The trigger logic was not changed during the new configuration, but the threshold of the search time window was increased to account for the increase in the background rate. Also, after 2015, the burst detection software was switched off during the passage through the SAA [Marisaldi et al., 2015].

3.5 ASIM

ASIM is the first mission specifically designed to explore TGFs and Transient Luminous Events (TLEs) from space, and was launched in 2018. ASIM is mounted on the Columbus module of the International Space Station (ISS), in an orbit at ∼400 km altitude and 51.6° inclination. The ASIM payload consists of the instruments Modular X- and Gamma-ray Sensor (MXGS) and Modular Multi-spectral and Imaging Array (MMIA). One of the main goals of ASIM is to find the occurrence rate of TGFs [Østgaard et al., 2019b]. The previous missions detecting TGFs have differed in their number of detections, due to differences in trigger windows. By the end of 2019, ASIM had detected 484 TGFs.

3.5.1 MXGS

MXGS (Figure 3.6) is an X- and γ-ray imaging instrument, with an imaging capability for finding the source region of energetic discharges and for investigating energy spectra of the events [Østgaard et al., 2019b]. MXGS contains two detector layers, the Low-Energy Detector (LED) and the High-Energy Detector (HED).

LED

LED consists of pixelated CZT (Cadmium-Zinc-Telluride) detector crystals, and has a geometric area of 1024 cm^2. The effective detection area at 100 keV is $\sim$400 cm^2. LED uses a coded mask for providing an 80° × 80° field of view (FOV). Photons with energies <400 keV can only enter LED through the holes of the coded mask [Østgaard et al., 2019b]. The mask is covered towards the inside by Kapton foil, preventing electrons with energies <200 keV from entering the LED, but allows photons with energies down to 15 keV to enter. The direction of the incoming photons can be determined from a penumbra pattern created at the coded mask, by the flux of incoming photons from distant sources [Østgaard et al., 2019b].

The outside of the coded mask is covered by a foil to absorb a large portion of UV radiation and visible light incident on the detector. Surrounding LED is a graded shield to prevent fluorescence photons, radioactive decays and ambient γ-rays from affecting the detector crystals. Each of LED's four Data Assembly Units (DAUs) consists of four chains of four Detector Modules (DMs), and each is read out separately. A DM contains 16 × 16 pixels, resulting in 4096 pixels per DAU and a total of 16384 pixels for LED.

When X-rays and photons enter through the coded mask, they react with the solid-state CZT-crystals and their energies are converted to pairs of holes and electrons. The CZT crystals are capable of measuring photons with energies 20-400 keV. The photons with energies exceeding 300 keV will mostly pass through LED. The photon energies are converted to electrical charges, and an electric field produced by the High Voltage Power Supply (HVPS) drifts these charges to the LED readout electrodes (Figure 3.6). The signals are thereafter amplified by Application Specific Integrated Circuits (ASICs), digitized and given a time stamp by the DAU [Østgaard et al., 2019b].

The average TGF is expected to have about 70 counts in LED, which has a temporal resolution of 1 μs given by 20-bit timestamps. There is a dead-time of 1.4 μs for each ASIC. There are eight ASICs connected along the same chain, and if another hit occurs in a different ASIC within 1.4 μs, this will be recorded as a multi-hit. When new hits occur within the 1.4 μs, the pile-up effect continues, resulting in an underestimated recording of count rates. Such events cannot be used for imaging because their energies are added and their addresses are incorrectly recorded [Østgaard et al., 2019b].

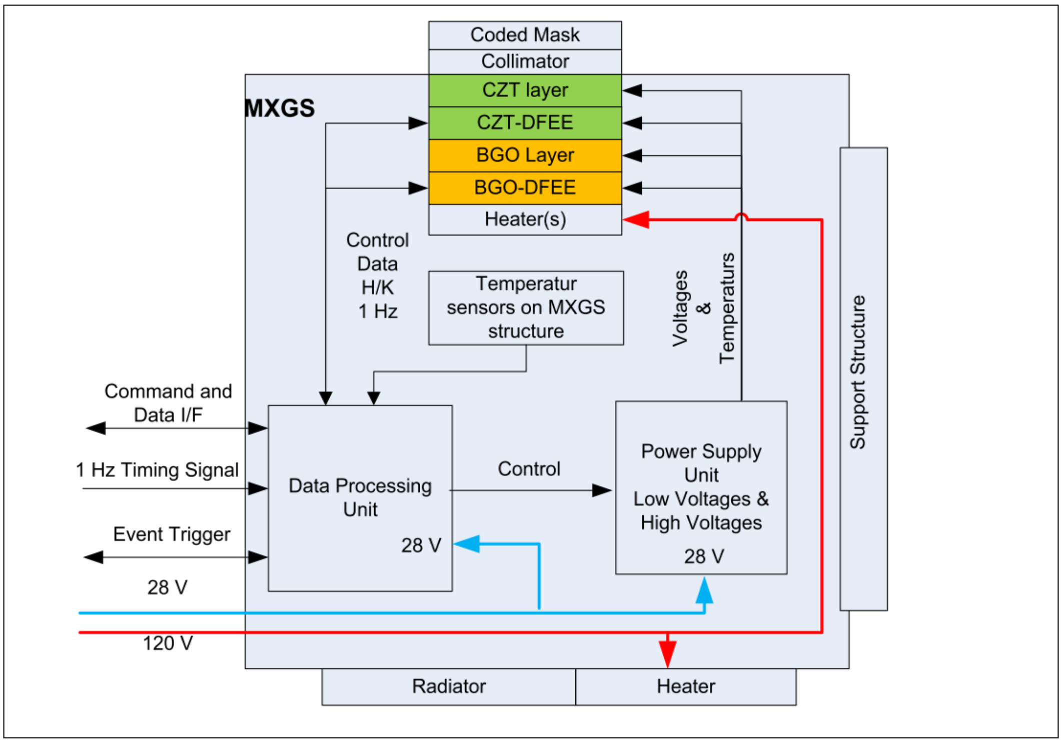

FIGURE 3.6: MXGS block diagram. Figure from Østgaard et al., 2019b.

HED

HED consists of 12 BGO (Bismuth-Germanium Oxide) detector bars coupled to PMTs. The geometric detector area of HED is 900 cm^2, and the effective detection area is ~650 cm^2/1 MeV. HED is placed behind LED, and shields LED from radiation from the rear end. Three radioactive 22Na-sources are placed between the detector layers of HED, and are used for in-flight calibration of the BGO-detectors. The BGOs are assembled in four DAUs, with each DAU consisting of three BGOs that are each connected to a PMT. Each of these is read out separately. Similar to the other missions mentioned, the HED high voltage (HV) is switched off when passing through the SAA, to protect the PMTs from high particle fluxes.

The photons passing through LED are absorbed in the BGO-crystals in HED. The BGO bars are sensitive to photon energies from 300 keV to >30 MeV. Light is produced in the scintillator crystals and received by the PMTs, digitized and processed before being passed to the DPU. The output from the PMTs is generated as voltage signals, digitized to 12-bit at a rate of 36 MHz [Østgaard et al., 2019b]. The average TGF is expected to give about 200 counts in HED, which has a temporal resolution of 28.7 ns, given by 27-bit timestamps. The dead-time for each BGO is 550 ns, defined by the peak time of the pulse (250 ns) and the time window between peak detection and a possible new pulse (300 ns). The output data from HED contains normal events, fast events (pile-up events) and overflow events. Overflow events occur when the maximum ADC value is exceeded, causing overflow duration to replace the energy bits [Østgaard et al., 2019b].

Trigger logic

Upon detection of a short burst, a trigger signal is generated, and the DPU formats the data for telemetry [Østgaard et al., 2019b]. All events detected within a two-second time interval around the trigger time is telemetered and subsequently analysed. The parameters transmitted for each event are information about address (for LED this is in terms of the pixel-ID, and for HED the BGO-bar), the pulse-height and the arrival time. The event data from both LED and HED are processed by the DPU, which is also responsible for the transmitting and receiving of triggers between MMIA and MXGS [Østgaard et al., 2019b].

The DPU is controlled by the Data Handling and Power Unit (DHPU), which provides the DPU with a 1 Hz Time Correlation Pulse (TCP). This is then encoded onto a 1 MHz clock signal (generated by the DPU, as outlined in Chanrion et al., 2019) passed to both the CZTs and the BGOs, and is used for time-tagging the data (with 1 μs resolution), resulting in a relative timing accuracy between MXGS and MMIA of ± 5 μs (from April 2019).

3.5.2 MMIA

MMIA (Figure 3.7) is a suite of optical sensors, and contains cameras and photometers for observations of thunderstorm activity and the associated optical activity [Chanrion et al., 2019]. The cameras and photometers are co-aligned and mounted on an optical bench. They are tilted 5° upwards to avoid disturbances from another platform. The DPU is mounted directly on the external payload adaptor, and has a radiating shield for thermal control [Chanrion et al., 2019]. MMIA contains three photometers, operating in the 337 nm (with a 4 nm bandwidth), 180-240 nm and 777.4 nm (5 nm bandwidth) bands, and two cameras operating at 337 nm (with a 5 nm bandwidth) and 777.4 nm (with a 3 nm bandwidth).

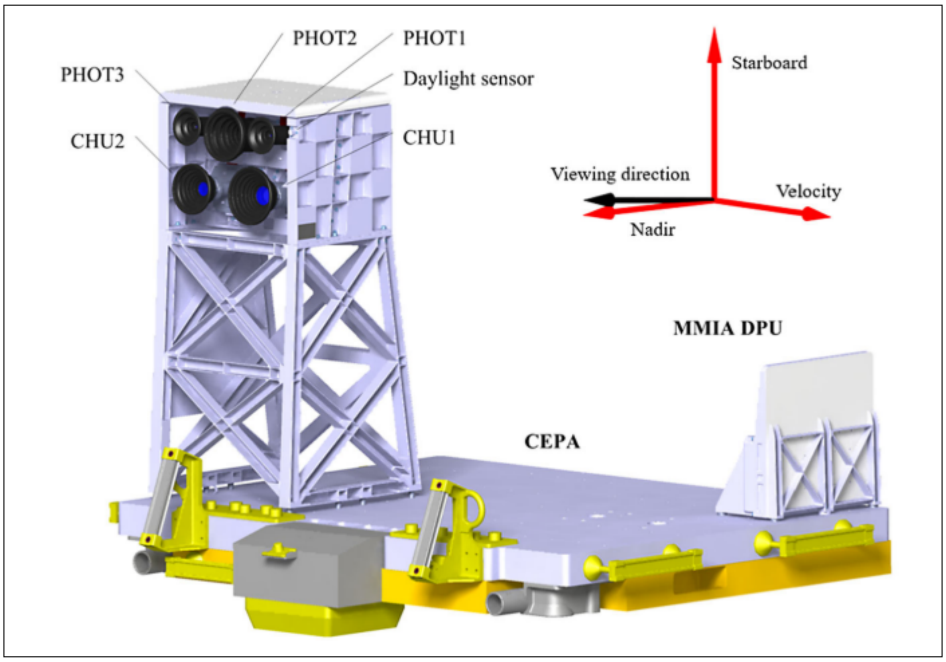

FIGURE 3.7: The components of MMIA. Figure from Chanrion et al., 2019.

The 777.4 nm band of PHOT3 is the band that is dominated by the lightning stroke, as PHOT1 and PHOT2 also detect emissions from TLEs. Emissions in the 777.4 nm band are mostly from atomic oxygen, and the emissions in the 337 nm band are mostly from $N_2 2P$ and although this band is the most sensitive to lightning, signals from TLEs are also seen [Østgaard et al., 2019a]. The emissions in the UV-band are almost completely absorbed by molecular oxygen in the air and are likely to originate from high altitudes [Chanrion et al., 2019]. The strength of the detections by PHOT1 compared to the detections by PHOT3 gives an indication of the emission altitude.

The camera head units (CHUs) contain a baffle to reduce stray light, a narrow band filter, a focal plane assembly, containing an electron-multiplication charged coupled device (EM-CCD), as well as electronics for control and readout of the frames from the sensor. Both CHUs have an 80°-diagonal FOV. The purpose of the band filter is to limit the shift in the centre wavelength, and it is located such that it limits the incident angle on the filter [Chanrion et al., 2019]. The output image frames of the CHUs consist of 1026 lines, with 1056 pixels per line. Each pixel can be encoded as 12-bit values. The CHUs have a temporal resolution of 83 ms. The light associated with one event is assumed to be contained inside a frame with a duration of 83 ms.

The photometers have a temporal resolution of 10 μs and also contain an optical assembly with a baffle for reducing stray light. As shown in Figure 3.8, the photometers also contain lenses, a PMT, a calibration system and proximity electronics. PHOT2 has a circular 80°-diagonal FOV, whereas PHOTS 1 and 3 have a square 80°-diagonal FOV. An interference filter limits the wavelength shift of PHOTs 1 and 3, and a square field aperture is placed between the filter and the last lense to limit the FOV such that the image matches with the CHUs [Chanrion et al., 2019]. A collimator lens is also included, to obtain a uniform spread of photon energies on the photocathodes of the PMTs. PHOT2 includes a front lens heater to remove contamination.

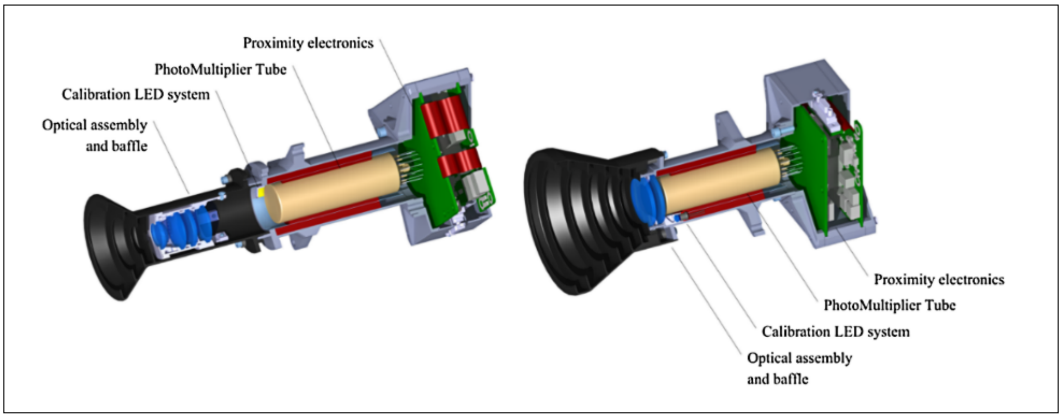

Figure 3.8: MMIA photometers. The left image illustrates the photometers (PHOTs 1 and 3) with a square 80°-diagonal FOV, and the right image illustrates the photometer (PHOT2) with a circular 80°-diagonal FOV. Illustration from Chanrion et al., 2019.

3.5.3 Relative timing between MXGS and MMIA

MXGS and MMIA can both cross-trigger and trigger independently. During a cross-trigger, two seconds of data are captured from both instruments when either the MXGS count-rate exceeds a certain threshold or MMIA triggers. The triggering system enables the capture of both optical and MXGS data for some TGFs and contains timed sequences of counts, using external second ticks (based on the ISS clock) and internal μs counters. The external counters are called TCPs and the internal are DPU ticks. The relative timing between the two instruments was ±80 μs between June 2018 and March 2019, due to an uncertainty in the time stamping of MMIA photometer data relative to the TCPs [Østgaard et al., 2019b]. From April 2019, the relative timing accuracy between MXGS and MMIA is ±5 μs. The timing correction consists of two terms; the frame shift and drift terms. The frame shift is 0-550 μs and the drift term 0-160 μs [Mezentsev, 2019].

A recorded event in MMIA can consist of up to eight frames, and if the observation lasts longer than these eight frames, a new event is created. The photometer data arrives in sequences of 10 μs, and these sequences are not time tagged. Instead, the instrument imposes its own time reference to the observation. For the beginning of the observation, MMIA provides the value of the preceding TCP-counter, which is a reference to the absolute time. MMIA also provides a label value of a DPU-counter, which is the number of microseconds after the trigger TCP. The system then provides the equivalent of the frame number after the TCP. There is a set of 12 possible values corresponding to the beginnings of the ideal frames. To account for the difference between ideal and real frames, a "mDPU" variable is defined by

$$mDPU = \frac{Frame\ number\ after\ TCP}{83250} \times 83200 \tag{3.3}$$

where 83200 denotes the length of the frame in microseconds for the real frames, whereas 83250 is the length of the frame for the ideal frames.

The length of the ideal frames is 83250 μs for frames 0-10, and 84250 μs for the last frame. For the real frames, the frame length is 83200 μs for frames 0-10 and 84800 μs for the last frame. The sum of all the frame lengths (both in the ideal and the real case) should be 1×10^6 μs. As a result of the difference between the real and ideal frames, there is a frame shift term to take into consideration for the relative MXGS-MMIA timing. The frame shift is given by N × 50 μs, where N is the number of the starting frame after the latest TCP. Since there are 12 frames per seconds, and the labels of the frames range from 0 to 11, the frame shift varies from 0 to 550 μs [Mezentsev, 2019].

In addition to the frame shift term there is also a drift term contribution to the discrepancy in the relative timing between the instruments. The drift term arises because there are not exactly $1\ \times10^5$ samples between two consecutive TCPs. The amount of samples between consecutive TCPs varies for each TCP, giving an average excess of 1.3 ± 0.5 samples. This implies that a TCP-"second" is on average 13 μs longer than a real second. Ideally, the first frame (frame 0), should begin exactly when the TCP arrives [Mezentsev, 2019], but instead each new frame 0 could start a few samples before the TCP arrives, and the discrepancy between the onset of the 0 frame and the arrival of the TCP accumulates with time. Due to this discrepancy, the system increases the size of the last frame (frame 11), by 16 samples when the discrepancy exceeds 16 samples. Also, if the beginning of frame 0 is delayed by more than 16 samples compared to the TCP, the system reduces the length of the last frame by 16 samples. On average, every eighth TCP has an increased number of samples in frame 11, but there is very rarely a decrease in the number of samples in frame 11. Whenever frame 11 has the standard length of 84800 μs it is called a "finishing frame", and when the length has been altered it is called a "correction frame". As the discrepancy accumulates, the drift term of the relative timing correction increases every second by on average two samples. As the correction frame is issued every eighth seconds on average and the drift component resets, the drift component reaches 16 samples, equivalent to 160 μs [Mezentsev, 2019].

The relative timing correction could be up to 710 μs, combining both the frame shift and the drift term corrections. The drift term can be corrected, but when the “finishing frame” is unknown, a drift term of 80 μs is added, with a ±80 μs uncertainty. If the “finishing frame” is known, the drift term can be added with a ±5 μs uncertainty.

3.6 The main characteristics of all the gamma-ray detectors

Table 3.4 summarizes some of the characteristics of the different platforms for TGF observations that are used in this thesis.

Table 3.4: Characteristics of the platforms

Characteristic	**RHESSI**	**AGILE**	**Fermi**	**ASIM**
Launch	2002	2007	2008	2018
Orbit altitude	510 km	~535 km	565 km	400 km
Orbit inclination	38	2.5	25.6	51.6
Data acquisition	Continuous	Triggered	Triggered/Continuous	Triggered
Energy range	3 keV-17 MeV	18 keV-30 GeV	8 keV-40 MeV	50 keV to >30 MeV

The effective areas of the AGILE, Fermi and RHESSI detectors are shown in Figure 3.9.

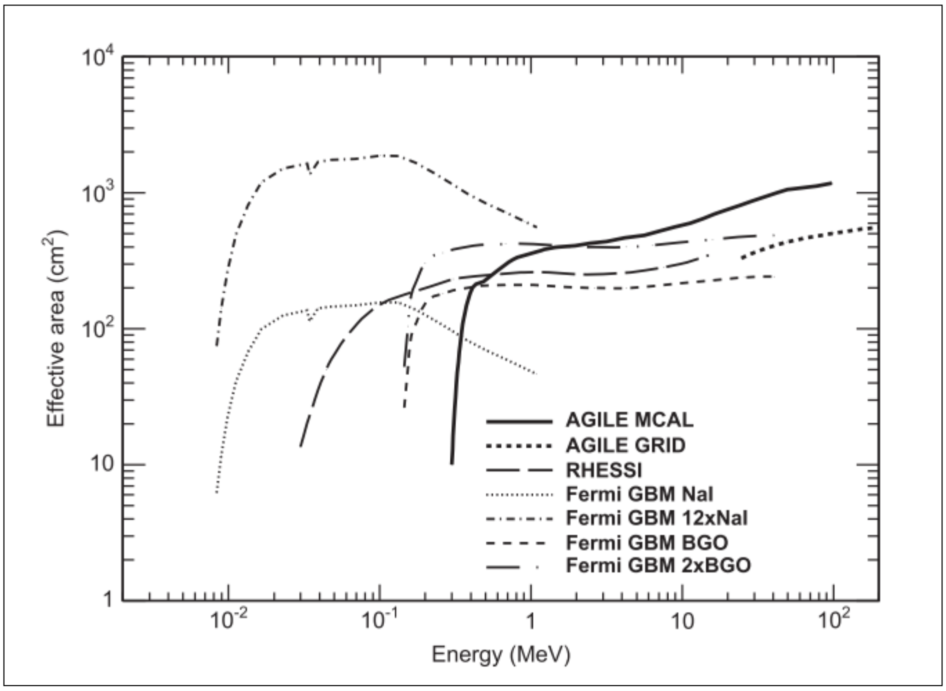

FIGURE 3.9: Effective areas of the AGILE, Fermi and RHESSI detectors. Figure from Marisaldi et al., 2013.

3.7 Ground-based lightning detection

To locate lightning strokes, we use lightning data from the WWLLN and Vaisala (GLD360) networks. These ground-based lightning detection networks are based on radiation of radiowaves during lightning flashes, radiated as “sferics” in the Very Low Frequency (VLF) band [Rodger et al., 2012]. Sferics are defined by Rakov and Uman, 2003, ch.13, to be; “lightning-produced electric and magnetic fields whose spectrum spans frequencies from a few kilohertz to a few hundred kilohertz”. The VLF signals can be detected far (>1000 km) from the source of the signals. Sferics frequency can expand into the Low Frequency (LF range). Radio waves from lightning strokes have the ability to propagate with low attenuation in the waveguide between the Earth and the ionosphere’s lower boundary [Rodger et al., 2012]. The waveguide is formed as a result of the ionosphere behaving like a conductor, due to its charged particles, creating a cavity between the Earth surface and the ionosphere.

Upon the observation of a sferic, the ground-wave, which is a radio wave propagating along the surface of the Earth, is first observed. The ground-wave is then followed by skywaves, which are a result of ionospheric reflections [Rakov and Uman, 2003, ch.13]. As the cutoff frequency for the waveguide formed between the Earth and the ionosphere is 3 kHz, sferics cannot contain frequencies <3 kHz.

3.7.1 WWLLN

WWLLN is a network of lightning sensors operating in the range 3-30 kHz, constituting a global lightning map. WWLLN measures the VLF from lightning, and by 2013, the network consisted of 70 VLF receiving stations globally. This allows for a lightning detection with ∼5 km accuracy corresponding to a timing accuracy of ∼15 μs. The lightning detection efficiency has varied over the years, but is low globally (∼11%) [Hutchins et al., 2013; Abarca et al., 2010], and higher for stronger strokes (>30%). The detection efficiency is not the same everywhere, due to the varying density of WWLLN stations. Rudlosky and Shea, 2013, also reported a better detection efficiency of WWLLN over oceanic regions.

The vertical electric fields created by lightning usually dominate over the power line noise in the receiver bandwidth (6-22 kHz). WWLLN can with high efficiency detect lightning-producing thunderstorms over 3 hour-intervals. After an upgrade in 2012, WWLLN was not only able to determine stroke locations, but also measure the stroke energies. The network has been shown to be biased towards high-energy strokes [Hutchins et al., 2013].

WWLLN detects both IC lightning and CG lightning strokes. As there is a higher peak current for the CG lightning strokes, WWLLN is better suited for detection of these [Rodger et al., 2012]. A lightning flash has to be detected by at least five different stations in order to be detected by WWLLN, and the residual time has to be less than or equal to 30 μs.

For determining lightning locations, a time-of-arrival method is used. By finding the time difference between the arrival of sferics at each receiving station, the position of the lightning could be determined by triangulation. The initial algorithm used for WWLLN data was based on time of group arrival (TOGA) of wave packets, and consisted of two main steps, as outlined by Rodger et al., 2012:

1. TOGA data was initially grouped based on a common lightning discharge. The measurements from two stations (Figure 3.10) are considered to originate from the same lightning discharge if:
$$\mid t_a - t_b \mid < \frac{r_{ab}}{c} \tag{3.4}$$
2. A numerical optimization method (Nelder-Mead) was used to determine the location where computed TOGA values would agree with the TOGA values detected.

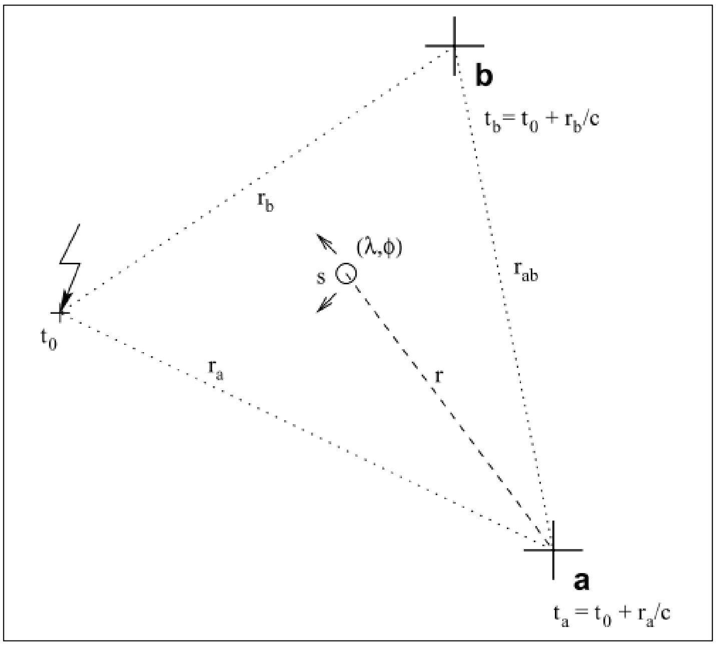

FIGURE 3.10: WWLLN stations a and b performing TOGA measurements from a lightning discharge [Rodger et al., 2012].

The initial algorithm was not sufficient to determine whether all the TOGA data originated from the same lightning discharge, because some of the TOGA data could contain measurements from several discharges. If no valid location was found, the original algorithm would simply discard all the datasets. The algorithm was improved in 2007 to discard the oldest TOGA data until a valid location was found [Rodger et al., 2012].

As outlined by Hutchins et al., 2012, each WWLLN station records the root mean square (RMS) value of the electric field used for the TOGA calculations of the waveform. As the digitization of the electric field waveform depends on several station-specific variables, the RMS electric field is reported on sound card units that are specific for each station. The stroke power is found by:

$$P_{stroke} = \frac{E_{scu}^2}{A_{local}^2} \times \frac{100kW}{(10^{\alpha/20}\mu V m^{-1})^2} \tag{3.5}$$

where E_{scu} is the electric field waveform (groundwave) that has been stored in the station's uncalibrated sound card units (SCUs). The power can then be found by using a conversion from this SCU-value to volts per meter, A_{local}, of the lightning waveform. The energy of the stroke can then be found by:

$$E_{stroke} = P_{stroke} \times t_{window} \tag{3.6}$$

where t_{window} is the triggering window.

The WWLLN stations are calibrated using the U.S. Navy Long Wave Propagation Capability (LWPC). Hutchins et al., 2012, also showed that the stroke power is directly related to the return-stroke peak current.

3.7.2 Vaisala

Vaisala's GDL360 is another global network of ground-based lightning sensors, detecting both CG lightning and IC lightning. The detections combine the measurements by multiple sensors [Said and Murphy, 2016], and use a combination of time-of-arrival (TOA) techniques and magnetic direction findings. Vaisala has an 80% detection efficiency for CG strokes (which comprises both CG and IC lightning) and a location accuracy of ∼2-3 km. To distinguish between CG lightning and IC lightning, Vaisala makes use of pulse classification, in contrast to other networks' use of altitude measurements.

An event must be detected simultaneously by at least three different sensors to be geolocated [Said et al., 2013]. Each of the sensors used by Vaisala stores a local empirical waveform bank, derived using VLF receivers and lightning location data from the National Lightning Detection Network (NLDN), to catalog the sferic waveforms [Said et al., 2010].

Chapter 4

Methodology

This chapter outlines the methods used for finding WWLLN associations for TGF detections by AGILE, Fermi and RHESSI, as well as the methods used for determining the onset and durations of TGFs detected by ASIM and the onsets of the associated optical pulses. The chapter also outlines how lightning network data (WWLLN and Vaisala) were connected to the ASIM detections.

4.1 Finding associated sferics for the TGFs detected by AGILE, Fermi and RHESSI

The TGF catalogs used for the comparison of different platforms preceding ASIM included TGFs detected by AGILE between March 2015 and September 2018, TGFs detected by Fermi between July 2008 and July 2016, and TGFs detected by RHESSI between 2002 and 2015. WWLLN associations were found for AGILE 2018 data, and Fermi 2016 data.

The light propagation time between the source and the satellite was found using the haversine equation and the law of cosines [Lindanger, 2018]. The haversine equation was used to find the arc length, S, between the subsatellite point and the WWLLN location.

Haversine formula:

$$S = 2R \arcsin\left(\sqrt{\sin^2\frac{\psi_2 - \psi_1}{2} + \cos\psi_1 \cos\psi_2 \sin^2\frac{\lambda_2 - \lambda_1}{2}}\right) \tag{4.1}$$

where ψ_1 and ψ_2 are the latitudes of points 1 and 2 respectively, λ_1 and λ_2 are the longitudes of the points, and R is the radius of the Earth.

Using $S = R\theta$ to find the angle θ between the two points, the law of cosines was used to find the distance, d, between the points.

$$d = \sqrt{(R + h_{sat})^2 + (R + h_L)^2 - 2(R + h_{sat})(R + h_L)\cos\theta} \tag{4.2}$$

where h_{sat} is the satellite altitudes and h_L is the source altitudes, assumed to be 15 km [Marisaldi et al., 2013]. This source altitude is within the range of thunderstorms, particularly over low latitudes [Dwyer and Smith, 2005].

The light propagation time was found by dividing the distance travelled by the speed of light.

4.2 Time sequence of TGFs and optical pulses detected by ASIM

To find the time sequence of TGFs and the onset of optical pulses, we had to:

1. Find the ASIM TGFs with associated optical data within the time period June 2018 - March 2019
2. Determine TGF durations
3. Determine the onset of optical pulses

4.2.1 Searching for ASIM TGFs with optical data

To find the ASIM TGFs with an associated optical detection file, a list of ASIM TGFs was used. In most cases, the TGFs with associated MMIA detections could be extracted from the list of ASIM TGFs based on the variables present for the event. For the events with available MMIA-data, the following variables were extracted from the list of ASIM TGFs:

- TGF-id
- Timing information for the TGF, including the year, exact time (in μs precision) and day of the year (DOY) for both MXGS and MMIA triggers
- The type of trigger (indication of whether it was a HED, LED or MMIA trigger)
- The xDPU variable
- Position information (longitude, latitude and altitude information for the ISS) at the time of the TGF detection

For aligning the MXGS and MMIA data and create a timeline with ±80 μs relative timing uncertainty, the procedure mentioned in subchapter 3.5.3 for handling relevant variables was followed. To find the MMIA-file associated with a detection in MXGS, several MMIA-files around the time of the MXGS detection were used. The correct MMIA-id was found from the file that could be aligned on a timeline with the MXGS data (Figure 4.1). Some events with MMIA-associations had to be removed from the extracted list of events. These were typically MMIA-triggers from the list of ASIM TGFs, and were removed because the MMIA-files could not be aligned in time with the MXGS detections (Figure 4.2).

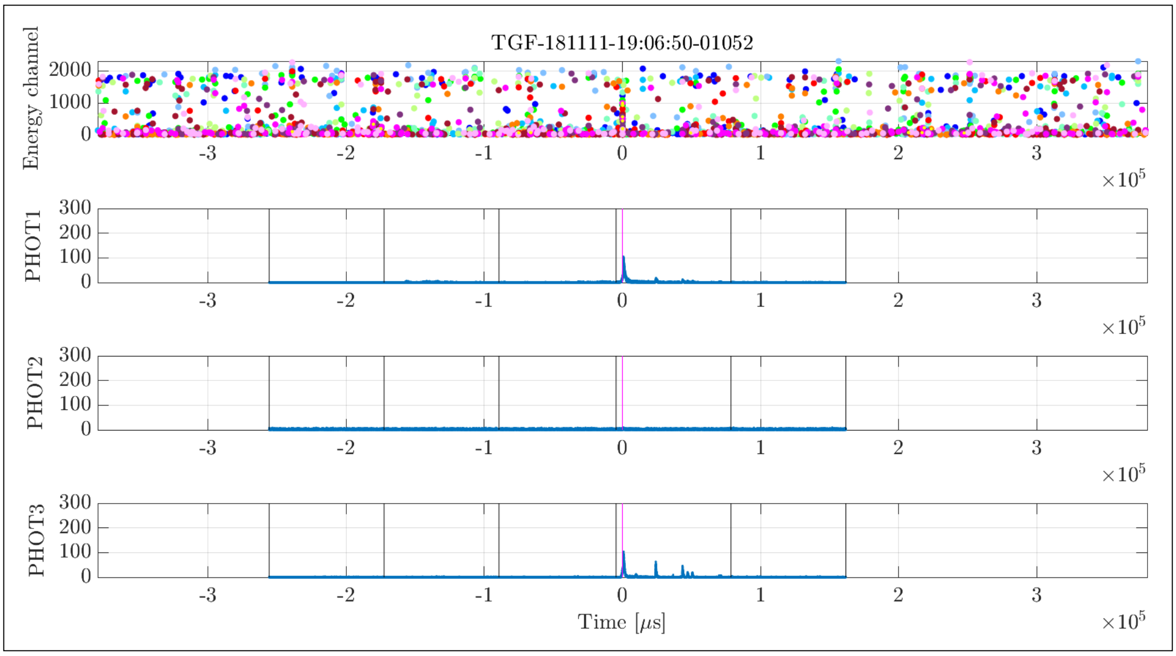

FIGURE 4.1: MXGS (top panel) and MMIA data (the other three panels) aligned for an event. The different colors in the energy-channel vs. time panel (top panel) indicate detections by different BGO detectors. The other panels show the MMIA photometer detections for the event. The magenta line indicates when the first photon of the TGF was detected in HED.

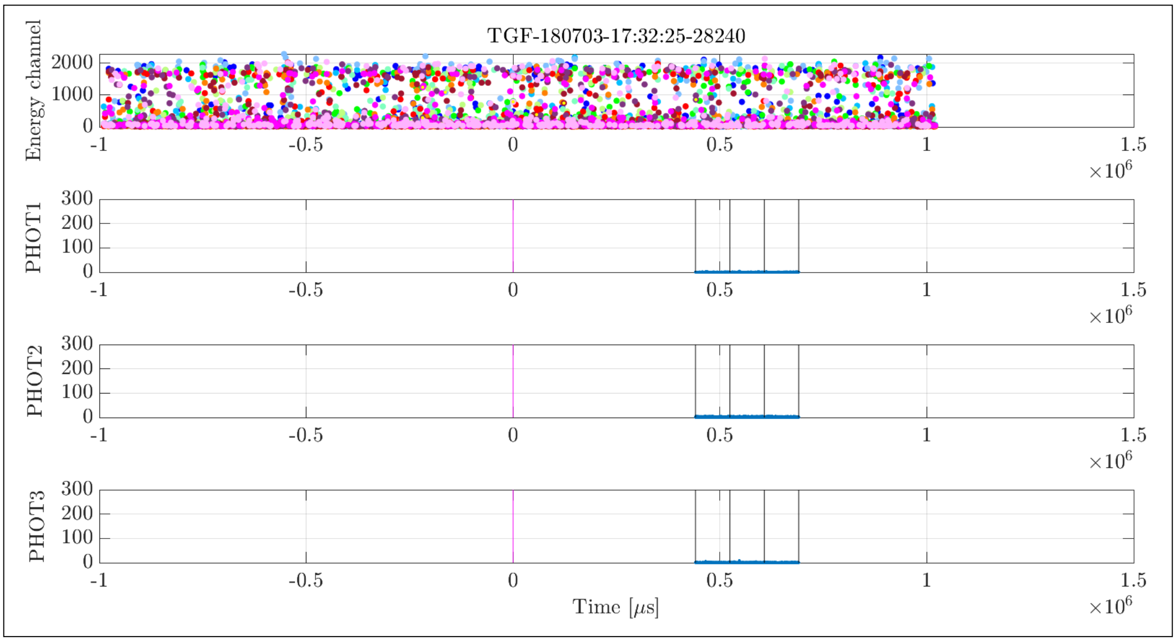

Figure 4.2: MXGS (top panel) and MMIA sequences (the other three panels) of data for an MMIA-triggered event, where the MXGS TGF detection and the MMIA data could not be aligned. The different colors in the energy-channel vs. time panel (top panel) indicate detections by different BGO detectors, and the magenta line indicates when the first photon of the TGF was detected in HED.

The TGFs with optical data were sorted into three categories; clear association, unclear association and no association. The clear association category included events where an optical pulse peak occurred within 2-3 ms of the first MXGS-detected photons (Figure 4.3). The majority of the optical pulses had onsets within 500 μs of the first TGF photon detected in HED. The unclear optical association category included pulses where there were several optical peaks, and the peak corresponding to the TGF could not be determined, and pulses that were too weak for determining an onset of the optical signal (Figure 4.4). The no association category included the events where the MMIA-data did not indicate any optical pulse (Figure 4.5), and there was no increase in activity around the MXGS detection time. This could occur when the lightning occurred outside the FOV of MMIA, but within the FOV of MXGS.

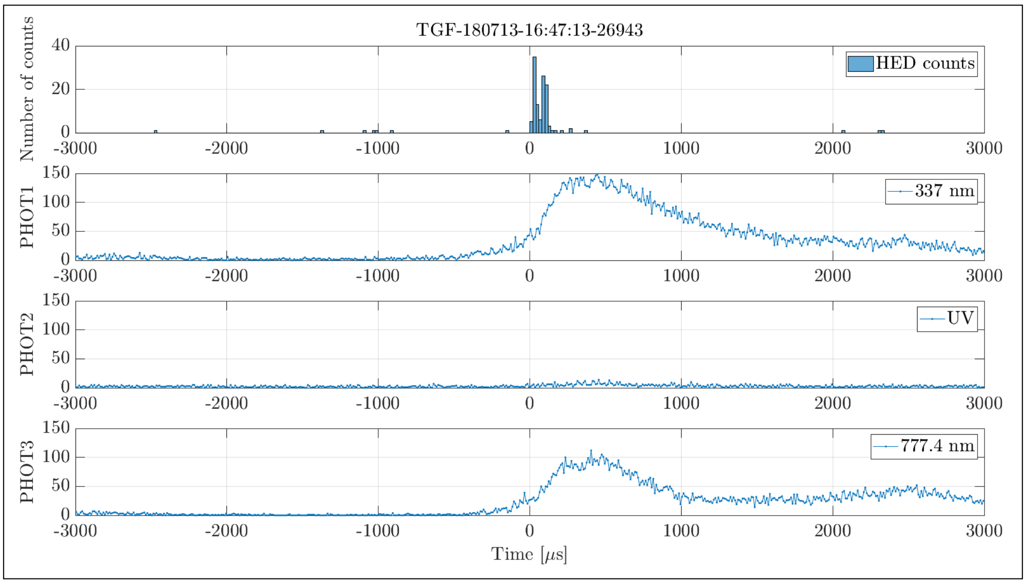

Figure 4.3: A TGF and an optical pulse with a clear association. The top panel shows HED counts in 20 μs bins, and the three lower panels show MMIA photometer detections for the event.

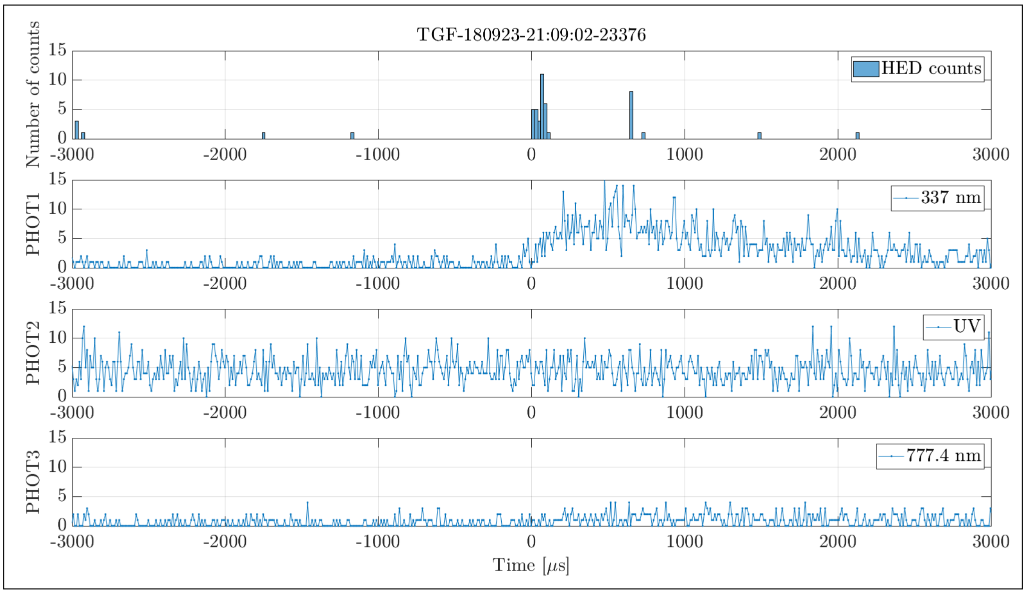

Figure 4.4: A TGF and an optical pulse with a weak association (*unclear association* category), where the onset of the optical pulse cannot be determined accurately. The top panel shows HED counts in 20 μs bins, and the three lower panels show the MMIA photometer detections.

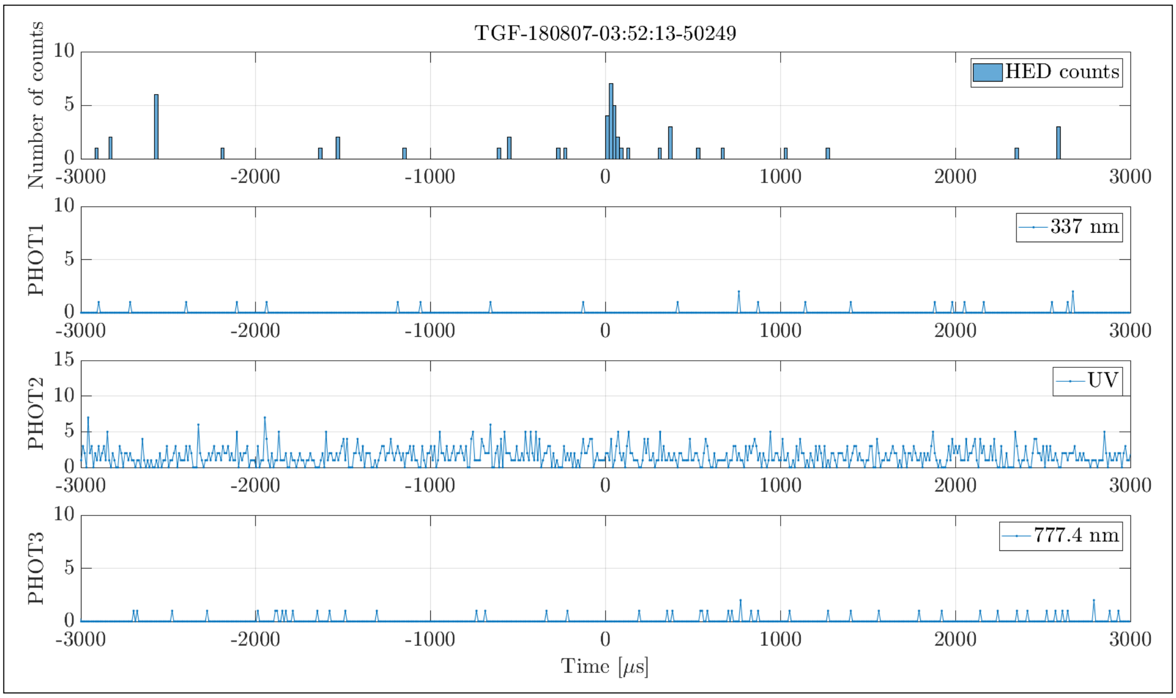

FIGURE 4.5: A TGF and optical MMIA data, where no optical pulse is seen (*no association* category). The top panel shows the HED counts for the event in 20 μs bins, and the three lower panels show the MMIA photometer detections around the TGF time.

WWLLN and Vaisala sferics were used to localize the lightning activity responsible for producing the ASIM TGFs. Lightning activity within the MMIA FOV was expected for TGFs within the clear optical associations category, and lightning activity in the outskirts or outside the MMIA FOV was expected for the other two categories.

Between June 2018 to March 2019, there were 95 MXGS-detected TGFs with aligned optical detections in MMIA (Table 4.1). To investigate the relationship between the TGF duration and the onset of optical activity, the TGFs with clear optical association in the MMIA PHOTs 1 and 3 were used.

4.2.2 Determining the TGF duration

The durations of the TGFs were determined using photon detections in the HED BGO detectors, with the aim of only including photon detections from TGFs and avoid the inclusion of random background counts. Two different approaches for determining the durations were explored. One of

Table 4.1: Categorization of the optical pulses

Category	**Amount**
Clear association	39
Unclear association	18
No association	38
Total	95

the methods explored was based on applying three criteria to the detector counts:

- The first HED count of the TGF had to be at least 50 μs later than any count preceding it, and within 50 μs of the following count
- Any HED counts within 50 μs of the next count were included in the TGF
- The last HED count of the TGF had to be at least 50 μs from the next detector count

To determine which photons to include in the TGF duration, plots of energy-channel vs. time of the BGO detector counts were constructed. These plots included all normal and fast events (subchapter 3.5.1). Different values (40, 50, 60 and 70 μs) were tested for the same criteria for all TGFs (both with and without associated optical data) during June 2018 - March 2019.

CZT detector counts from LED were included to ascertain that the end points of the TGFs were set correctly and not cut off too early by our criteria, in gaps of counts >50 μs only seen in HED. Some of the gaps in the energy channel vs. time plots of the HED BGO counts could be caused by saturation due to very high flux, and LED counts could be used to find these gaps. The inclusion of the CZT counts was not, however, used for determining the endpoints of the TGFs (as LED counts also included a long Compton tail for most of the observations), but rather for investigating the separations caused by the above criteria. After comparing the results and checking with the durations found by repeated visual inspections, 50 μs was found to be the photon separation criteria that resulted in the fewest separations of the BGO detector counts where CZT counts indicated a continuous event.

Figure 4.6 shows how the inclusion of CZT counts could indicate the last photon of the TGF. By including CZT counts, the apparent last count is at 181.5 μs. By using the above criteria for 50 μs, the last photon of the TGF is at 112.9 μs. Applying the same criteria with 40 μs gives a duration of 67.08 μs.

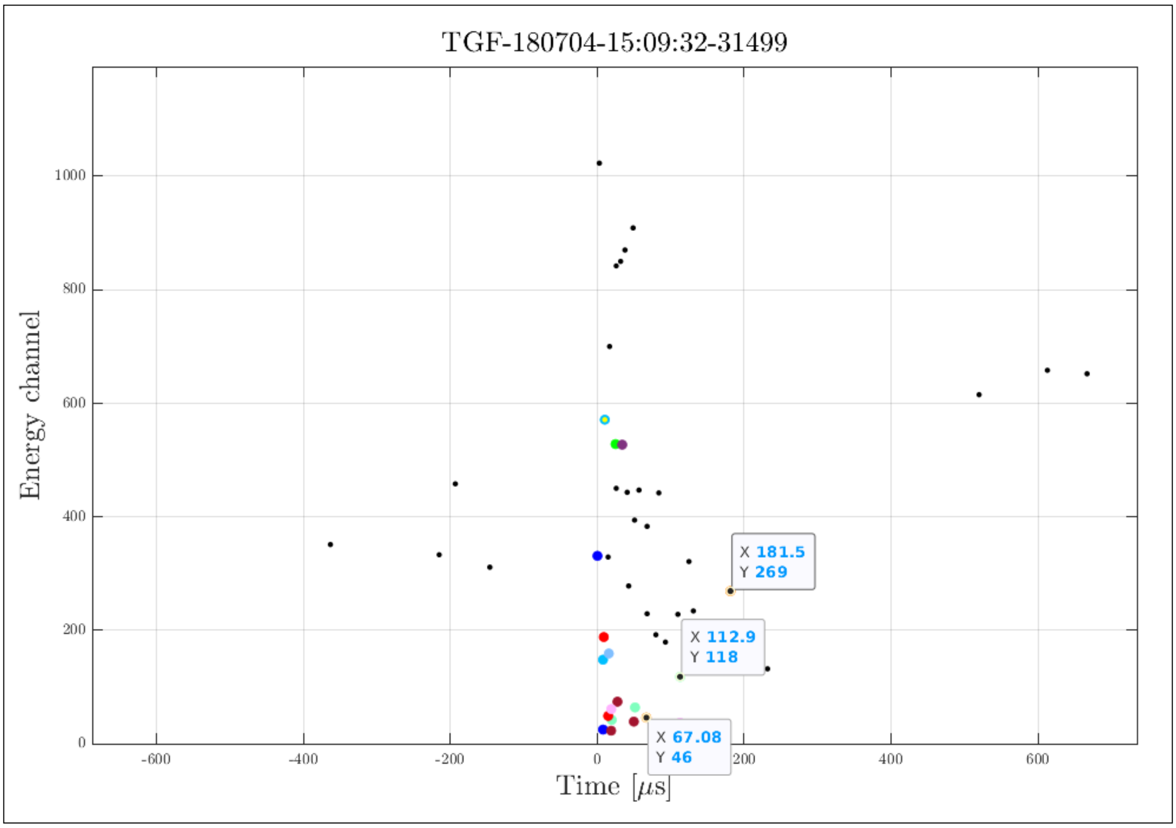

Figure 4.6: Plot of the detector counts from HED and LED in different energy channels versus time, showing different duration definitions. The different colors indicate counts in different BGO detectors. The CZT counts are shown by the smaller, black circles.

In addition to including LED counts to investigate the gaps between BGO counts, histograms with a binning of 20 μs were used for the BGO counts to determine whether there was a separation between some of the counts. The 20 μs binning was chosen as 20 μs is approximately half the minimum duration found for the ASIM TGFs. Figure 4.7 (top panel) shows an event where the HED detection appears to have fewer counts around 60-80 μs, which can also be seen in the histogram below. By the inclusion of LED counts, it is apparent that the two groups of BGO counts are likely to belong to the same event.

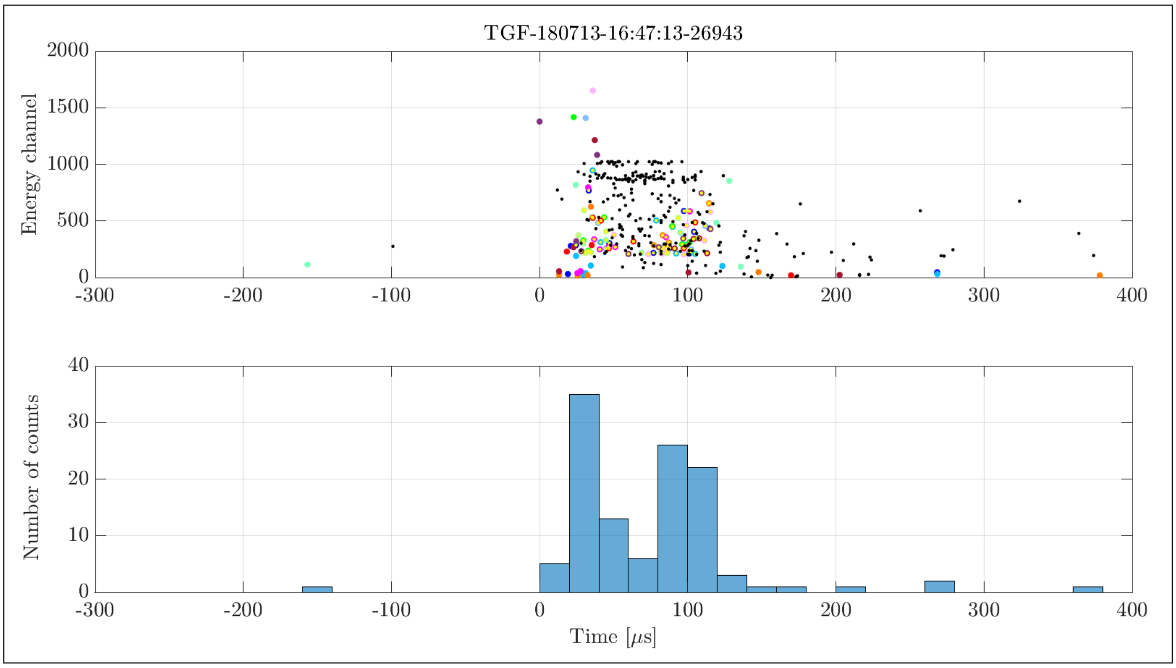

FIGURE 4.7: The top energy-channel vs. time plot shows detector counts from HED and LED, with the colors referring to detections in different BGO detectors. The CZT counts are the small, black circles. The histogram in the bottom panel shows the counts from HED in bins of 20 μs.

The other approach explored to determine the duration of the TGFs was based on a core duration, and finds the duration using a high percentage of the HED counts associated with the TGF. To ascertain that any relevant BGO counts were included, all BGO counts that had a separation <100 μs (using the same criteria as mentioned above) were used. 100 μs was chosen as separation as 70 μs also resulted in some early cut-offs by our criteria (subchapter 5.2.2). From the selected counts, the interval of 90% of the counts that gave the shortest duration was used. This implies that for an event with 100 HED counts, a sliding window was used with a starting point at the first BGO count and included the next 89 BGO counts to find a duration. Another 10 duration times were recorded using the sliding window. From these 11 possible durations, the shortest was chosen as an approximation of the TGF duration.

4.2.3 Determining the onset of optical pulses

The onsets of the clear optical pulses from photometer data were determined through both visual inspections and using a double linear method. The steps of the double linear method were:

1. Find a background level based on the activity preceding the main optical pulse, and draw a straight line indicating this background level
2. In the case of an apparent increase above the background level within 1 ms before the main optical pulse, identify the most linearly increasing region of this increased activity, and extrapolate a line along the linear increase
3. Identify the most linearly increasing region at the beginning of the optical pulse, and extrapolate a line through this region

If all the above lines were present for an event, the onset of the pulse would be at the intersection of the line from the pre-activity, indicative of lightning leader activity [Østgaard et al., 2019a], and the line extrapolated through the linearly increasing pulse (Figure 4.8). If the lightning leader activity appeared to be very weak in the photometer detection, the onset of the pulse would be at the intersection of the background line and the line indicating the linear increase of the pulse. Two lines were drawn through the region of linear increase of the optical pulse, and two lines through the pre-activity region, to find a range where the onset was likely to be located (Figure 4.8).

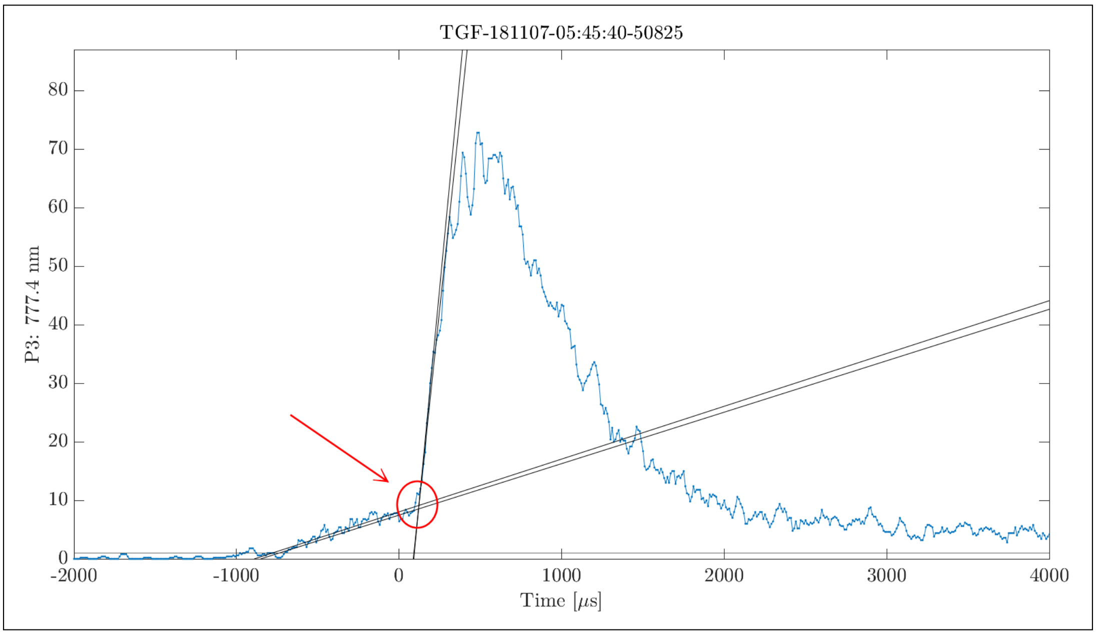

Figure 4.8: Selection of range of likely onsets of the 777.4 nm optical pulse seen in PHOT3. Two lines are drawn through the most linearly increasing region of the main optical pulse and two lines through the most linear increase of the pre-activity region. The red circle shows the location of the intersection of the lines drawn through the different parts of the activity, indicating the range of possible onsets. The bottom line indicates a background level.

Although the example shown in Figure 4.8 gives a quite narrow range where the onset is likely to be found, other events had a larger range of likely onsets. An example where the selection of the pre-activity influences the range of onsets is shown in Figure 4.9, where the pre-activity does not have a clear linearly increasing region. The range where the onset is likely to be located has a length of ∼15 μs. Another example where the selection of the pre-activity impacts the estimated range of likely onsets is shown in Figure 4.10. However, for both examples, the estimated range of possible onsets is significantly less than the ±80 μs relative timing uncertainty of MXGS and MMIA.

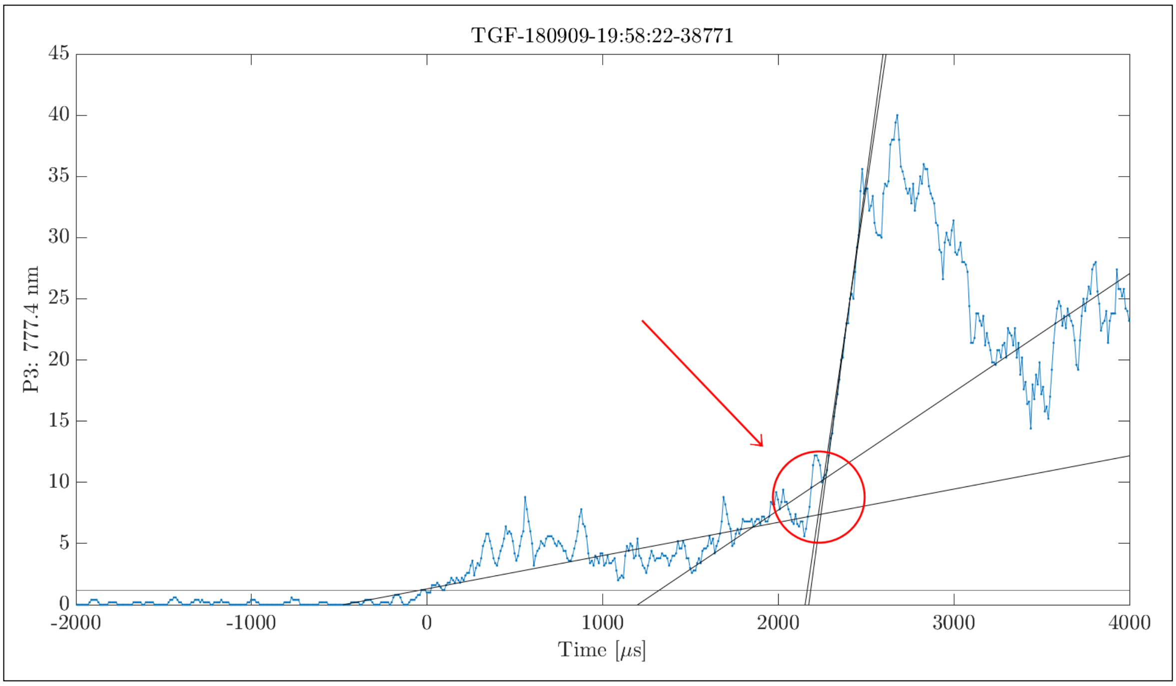

FIGURE 4.9: Selection of range of possible onsets of the 777 nm optical pulse, where the selected start of the pre-activity region determines the length of the range of possible onsets. The red circle shows the location of intersection of the lines drawn through the different parts of the activity, indicating the range of possible onsets. The bottom line indicates a background level.

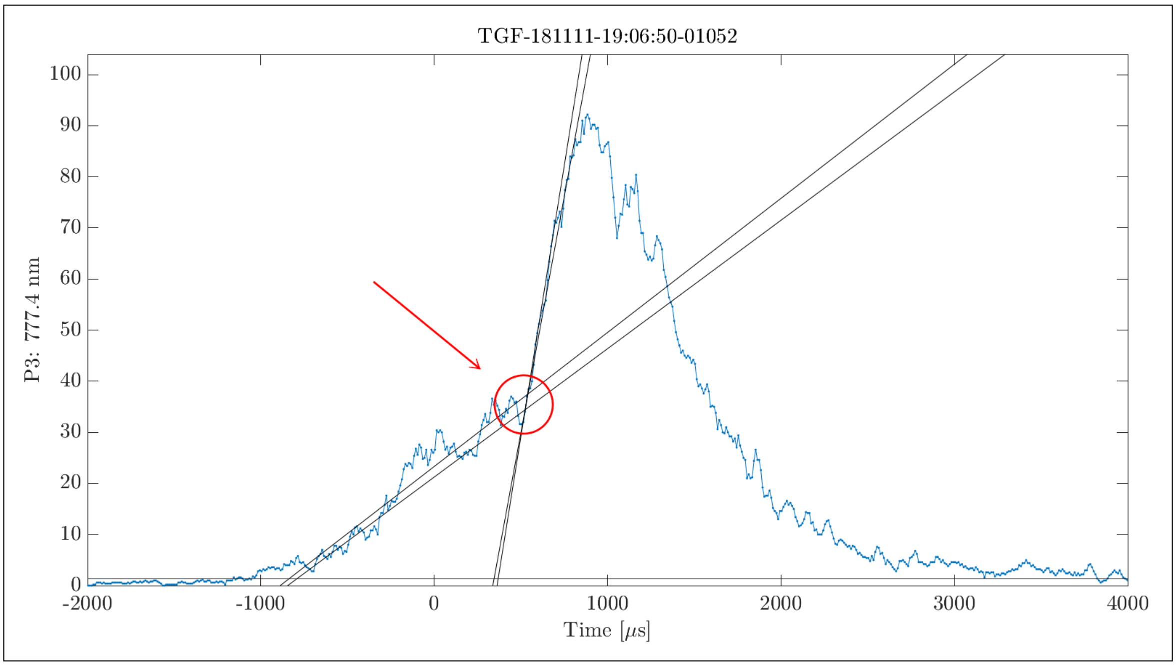

FIGURE 4.10: Selection of range of possible onsets of the 777 nm optical pulse, where the selection of the slope through the pre-activity region determines the length of the range of possible onsets. The red circle shows the location of intersection of the lines drawn through the different parts of the activity, indicating the range of possible onsets. The bottom line indicates a background level.

A few of the events that had a clear optical pulse showed very little visible pre-activity in PHOT1 (337 nm) and PHOT 3 (777.4 nm) (Figure 4.11). Although the photometer data indicate very faint pre-activity, a possible Vaisala association was found for the event, at ∼230 km from the ISS footpoint, which is in the outskirts of the MMIA FOV (subchapter 4.2.4). As the event had an associated Vaisala detection, it was included in the clear optical association category despite not having strong pre-activity.

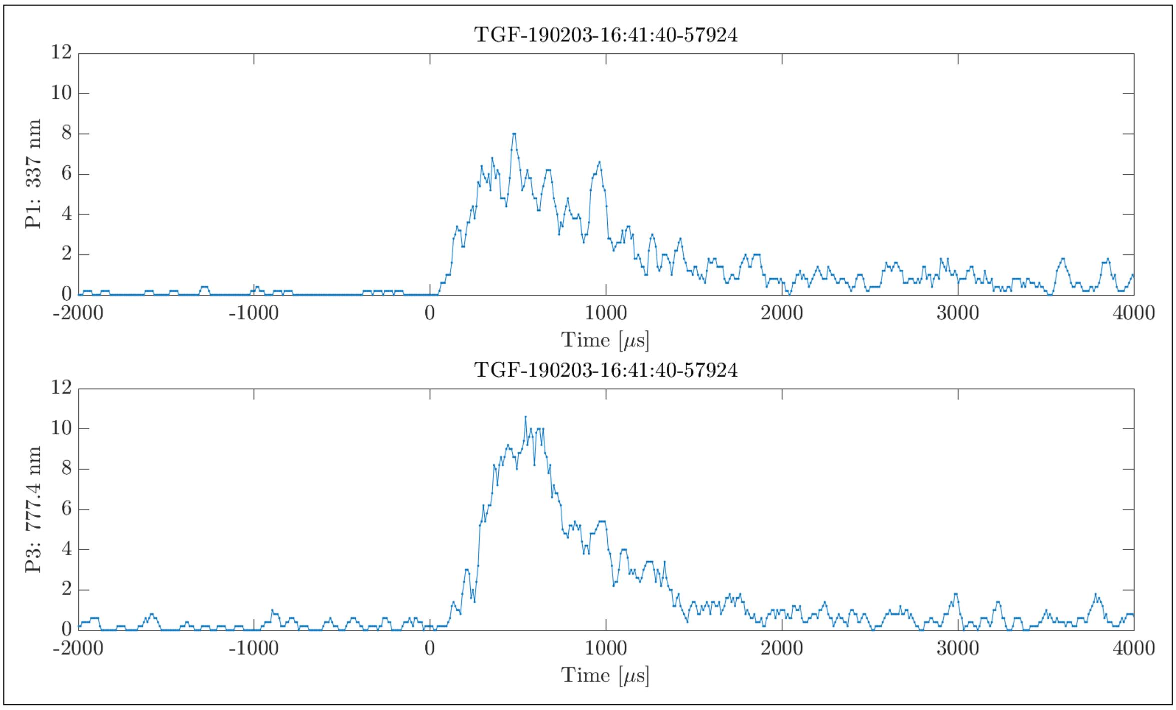

FIGURE 4.11: Detections by PHOT1 and PHOT3, showing very faint leader activity.

For the majority of the events, the optical pulse detected in PHOT3 was used, as the 777.4 nm band is the band where the signal is dominated by the lightning stroke. For the events where this pulse was weak or unclear, data from PHOT1 was used to determine the onset of the optical pulse. If there appeared to be several peaks present in the PHOT3 data, PHOT1 (as well as PHOT2 if there were detections in the UV-band for the event) was used to determine the peak of the main optical pulse associated with the event (Figure 4.12). If it was possible to align the optical data with sferics (subchapter 4.2.4), this was also used to determine the likely peak of the main optical pulse. For the case shown in Figure 4.12, a Vaisala association could be aligned with the first peak shown in the PHOT3 panel.

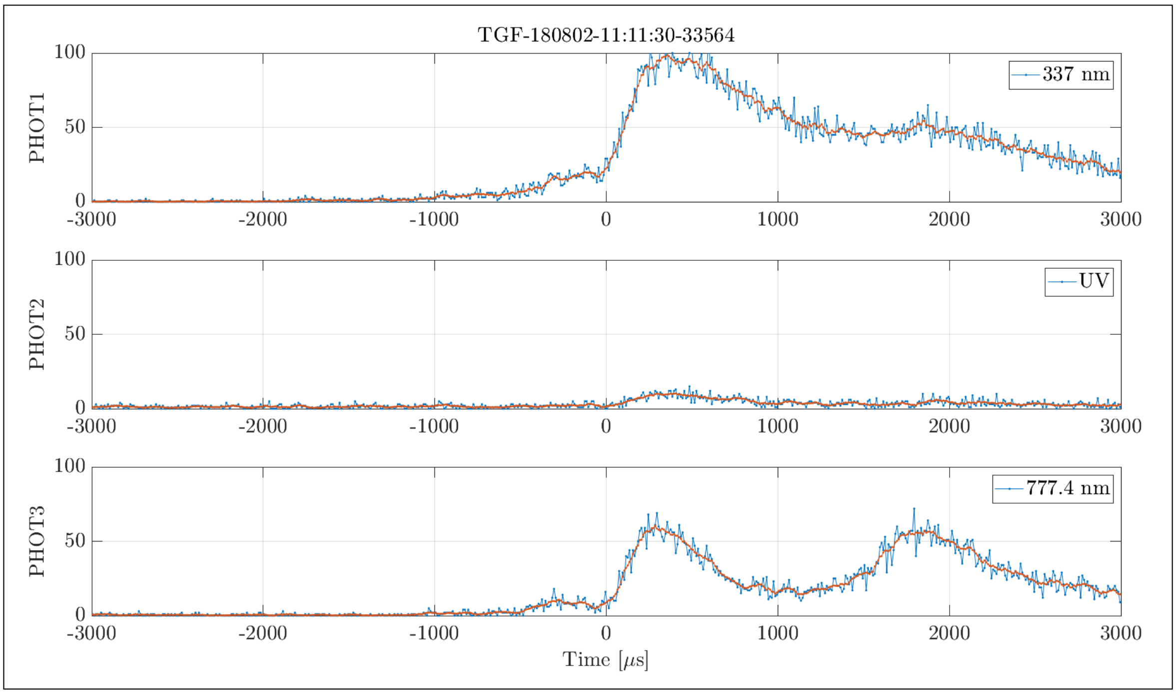

FIGURE 4.12: Data from all three photometers for a specific event, used to select the main optical pulse in PHOT3. Blue indicates the photometer data, and red shows a moving mean.

4.2.4 Finding associations to ground-based lightning detection networks

For the TGFs in the clear optical association category, lightning detection network data from Vaisala and WWLLN were used to confirm that there was lightning activity within the FOV of MMIA around the time of the TGF detection by ASIM. For the TGFs in the unclear association or the no association categories (Table 4.1), WWLLN and Vaisala data were used to determine whether there was lightning activity within or outside of MMIA's FOV.

When determining the FOV of MMIA, the geometry of the photometers, the 5° tilt of the CEPA (Columbus Externals Payloads Adaptor) and the movements of the ISS should be taken into account. The photometers detecting in the 337 and 777.4 nm bands have a square 80° diagonal FOV, and the photometer detecting in the UV-band has a circular 80° FOV. The geometric differences and the tilt of the CEPA and the ISS lead to an increased uncertainty for some of the events, as they could have lightning network matches in the outskirts of the FOV. Determining how the tilt of the CEPA and the movements of the ISS affect the MMIA FOV is referred in future work (chapter 6).

Processing the lightning network files

Vaisala GLD360 data files (csv-files) were downloaded from `https://asdc.space.dtu.dk/`, in four-minute intervals centered around the TGF-times. The following variables were extracted from the files:

- Timing of detections (in ns precision)
- Position information (longitude and latitude of the detection)

The WWLLN data files were given in txt-format and the same variables were extracted as from the Vaisala-files.

To determine the travel time from the lightning source to the ISS, the World Geodetic System 1984 (wgs84) reference ellipsoid was used to get a reference ellipsoid, and thereafter converted to Earth-Centered Earth-Fixed (ECEF) Cartesian coordinates for both the ISS location and the lightning detection coordinates. The source altitude of the lightning was set to 15 km. The reference ellipsoid was used to determine the geodesic distance from the lightning source to the ISS footpoint.

Possible lightning network detections that could be associated with the detected TGF were extracted using the timing and position information, as well as the computed travel time and geodesic distance, within the following initial criteria for reducing the dataset:

- The time difference between the TGF-time and the lightning detection network time (taking into account the travel time) had to be within 1 s
- The latitude and longitude of the lightning detection had to be within 20° of the ISS latitude and longitude
- The geodesic distance from the lightning source to the ISS footpoint had to be less than 1000 km

MMIA FOV

The square FOVs of PHOTs 1 and 3 and can be found using the 80° diagonal FOV and the altitude of the ISS (h in Figure 4.13). The distance from the centre of the square (∼345 km) spanned to a corner of the square was found by:

$$c = \tan(\alpha) \times h \tag{4.3}$$

where $\alpha = 40°$. The shortest distance from the square centre to the edge of the FOV (~244 km) is denoted by x, and found using an isosceles and equilateral triangle and Pythagoras' theorem:

$$x^2 + x^2 = c^2 \rightarrow x = \sqrt{\frac{c^2}{2}} \tag{4.4}$$

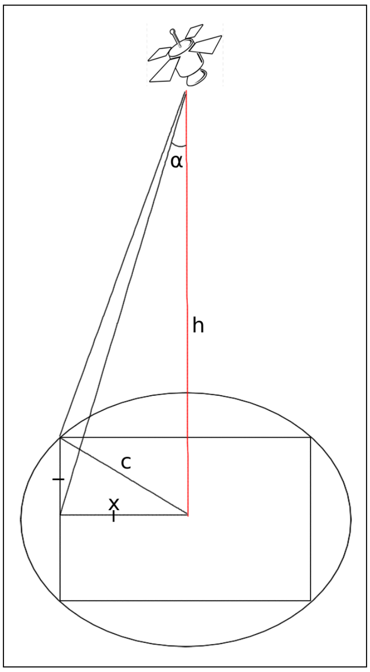

FIGURE 4.13: Illustration of the variables used for finding the FOV of PHOTs 1 and 3. The circle indicates the FOV of PHOT2, whereas the square indicates the FOV of PHOTs 1 and 3.

For a given TGF, ground-based lightning data were plotted to determine whether their detections occurred within or in the proximity of the FOV (Figure 4.14).

For the sferics that were either within or in the proximity of the MMIA FOV, the timings of the sferics were further compared with the TGF time. For the TGF in Figure 4.14, an associated Vaisala detection was found by aligning the optical data with Vaisala observations (Figure 4.15), as ASIM has an absolute timing uncertainty of 0-20 ms. This was done to ascertain that the optical pulses originate from the locations provided by the possible lightning network association. Figure 4.16 shows lightning activity detected by WWLLN and Vaisala within 1 s of a TGF in the no pulse association category, clearly outside the FOV.

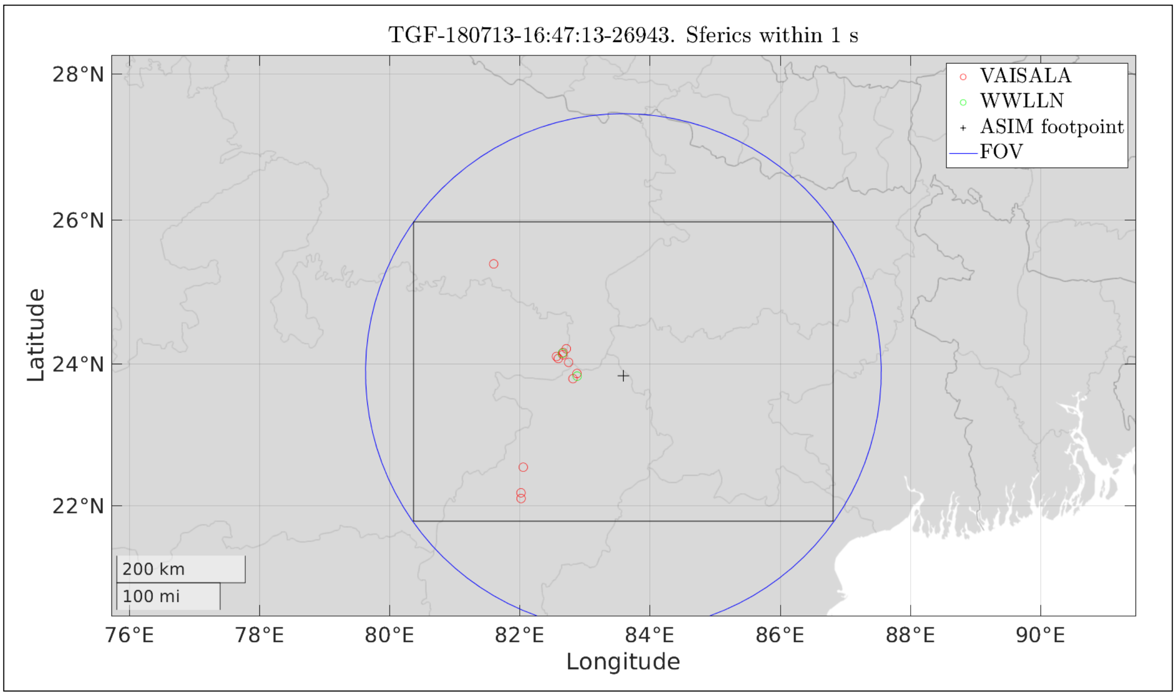

FIGURE 4.14: Map of WWLLN and Vaisala sferics inside the FOV of MMIA within 1 s of the TGF detection.

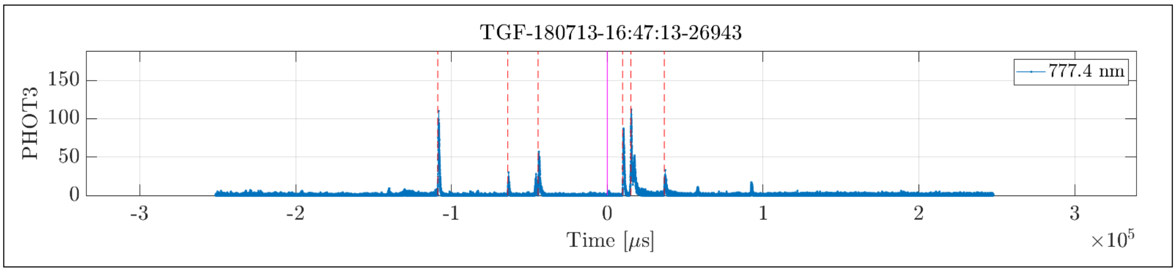

FIGURE 4.15: Aligning the lightning network detections with the MMIA optical pulse. The line at x=0 indicates the timing of the first photon of the MXGS detection, and the non-solid red lines indicate the lightning sferics.

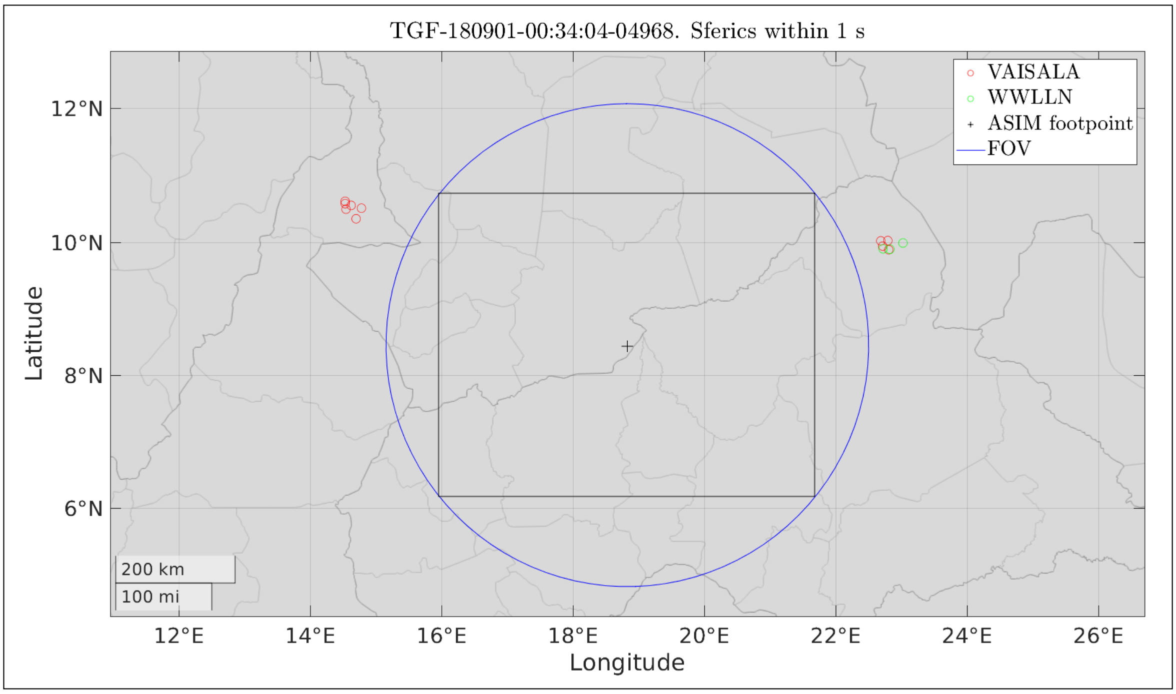

Figure 4.16: Map of MMIA FOV and WWLLN and Vaisala sferics outside the FOV, within 1s of the TGF.

Chapter 5

Results and Discussions

This chapter outlines the comparison of different platforms that have detected TGFs, followed by the investigation into the time sequence of TGFs and optical signals detected by ASIM.

5.1 Comparing different platforms for TGF observations

There are several spacecrafts that have detected TGFs, using different detectors and from different altitudes and orbits. We will here explore the similarities and differences between the TGF detections by these platforms. This subchapter will outline the differences in the geographic distribution of the TGFs detected by the three platforms AGILE, Fermi and RHESSI (subchapters 5.1.1, 5.1.2, 5.1.3, 5.1.4), and the differences in the TGF durations and number of counts detected by AGILE and Fermi (subchapter 5.1.5).

The distributions of TGFs detected by AGILE and Fermi include two samples of observations; a "standard" sample including all TGFs detected by the satellites within the time periods mentioned in Chapter 3, and a sample of TGFs that have associated WWLLN data. The RHESSI TGFs used in this thesis have not been connected to WWLLN data, but RHESSI TGFs have been connected to WWLLN data by others in our group [Gjesteland et al., 2012; Nisi et al., 2014; Mezentsev et al., 2016; Albrechtsen et al., 2019].

5.1.1 Geographic distribution

The global distribution of TGFs detected by the three platforms shows a clustering over the continents in the equatorial region (Figure 5.1). There is a gap in the South Atlantic ocean for the distributions of TGFs detected by all three platforms, as the instruments are powered off during the passage through the SAA. There is a smaller fraction of WWLLN matches over central Africa, where the detection efficiency of WWLLN is lowest.

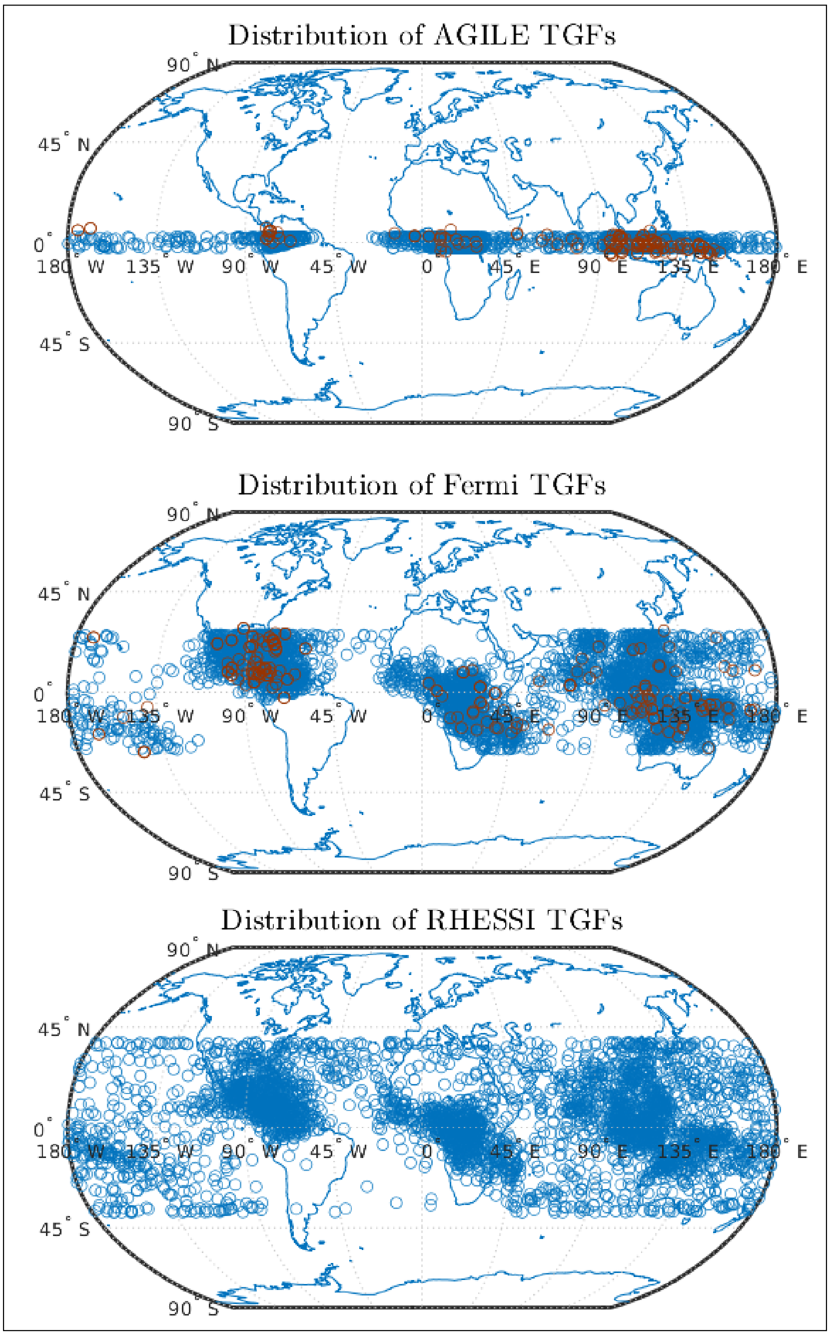
Distribution of AGILE TGFs

Distribution of Fermi TGFs

Distribution of RHESSI TGFs

FIGURE 5.1: Global distribution of the TGFs detected by AGILE (March 2015 - September 2018), Fermi (July 2008 - July 2016) and RHESSI (2002 - 2015). The blue circles indicate the subsatellite point of the spacecraft at the time of detection of the TGF. The sample with WWLLN associations is shown in red, and for these the WWLLN locations were used.

5.1.2 Longitude distribution

Figure 5.2 shows the longitude distributions of the TGFs detected by AGILE, Fermi and RHESSI. For the sample with WWLLN associations, the WWLLN longitudes were used. This sample is much smaller than the full sample of TGFs, and therefore the y-axis gives a fraction of the TGFs (with all the bars for one sample adding up to 1). The TGFs were mainly detected over three continental regions; central America [-90°,-60°], Africa [-10°,+30°] and the Maritime continent [+100°,+150°]. For AGILE TGFs, the majority of the standard sample TGFs were found over Africa, due to the satellite's orbit causing AGILE to spend more time over Africa. For the sample with WWLLN associations, the majority was detected over the Maritime continent (South-East Asia).

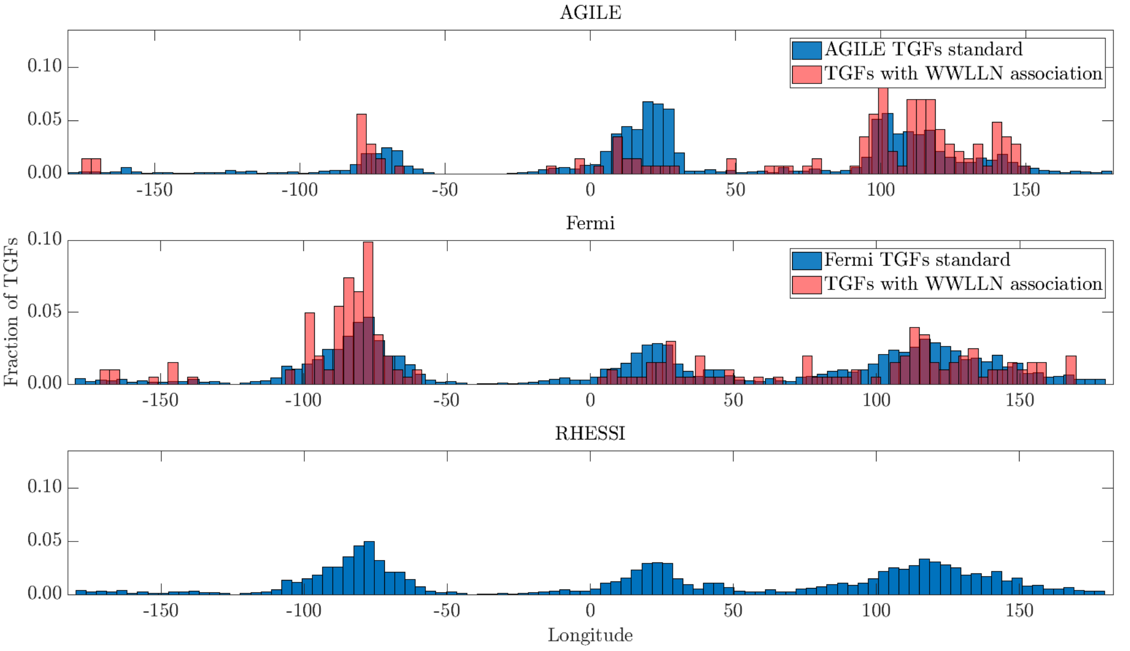

FIGURE 5.2: Longitudes of the TGFs detected by AGILE, Fermi and RHESSI.

The Fermi TGFs used in this thesis were detected between July 2008 and July 2016. From July 2010, the telemetry procedures for Fermi were changed to continuous TTE data acquisition from specific regions likely to have high TGF activity, and to continuous data acquisition for the entire orbit from 2012 [Briggs et al., 2013]. The continental regions favored by the geographically biased exposure of Fermi contained most TGFs (Figure 5.2). This bias, however, could have amplified the regional dependence. The clustering in the longitude distribution is in accordance with the results described by Marisaldi et al., 2015, showing that the longitude is clustered about the continents in the equatorial region, where the Intertropical Convergence Zone is found. The longitude distribution of the RHESSI TGFs shows the same trend as the standard sample Fermi TGFs, with a general continental clustering.

5.1.3 Latitude distribution

Figure 5.3 shows the latitude distribution of the TGFs detected by the same platforms, and emphasizes the orbital inclinations of the satellites. For all three platforms, the latitude distribution has an increase in the fraction of detected TGFs in the last bin at the boundaries of their latitude bands. This is caused by the satellites' orbits, leading to oversampling of TGFs [Briggs et al., 2013], and by the satellites' orbits causing them to spend more time at higher latitudes. This is especially evident for AGILE TGFs. AGILE has a very narrow latitude span compared to Fermi and RHESSI, as it has an orbital inclination of only 2.5°. The blue bars in Figure 5.3 show the distribution of latitudes for the full sample without WWLLN associations, and the red bars shows the distribution for the sample with WWLLN associations. For the sample with WWLLN associations, the WWLLN latitudes were used, resulting in TGFs found beyond the 2.5° latitude band of AGILE. The WWLLN associations can be found up to ∼6.5°, indicating that the WWLLN associations were located ∼440 km from the subsatellite point. The latitudes of the WWLLN associations for Fermi are also a few degrees outside the latitude band implied by the orbital inclination of the satellite. The WWLLN latitudes are found up to ∼3° from the latitude band of the spacecraft, indicating that the WWLLN associations are located ∼332 km from latitude band imposed by the orbital inclination of the satellite.

The distributions of the Fermi and RHESSI TGFs indicate a decrease towards higher latitudes, with the exception of the last bin. This suggests an oversampling of TGFs (similarly as seen for AGILE TGFs), due to orbital implications. If the orbital implications were corrected for, the distribution would continue to decrease for higher latitudes. Another possible explanation for the decrease towards higher latitudes is tropopause variations for different latitudes [Hoinka, 1998], as the height of the tropopause is typically lower at higher latitudes, causing thunderclouds that are less tall than those found in the equatorial region [Cooray, 2014]. Additionally, Mackerras and Darveniza, 1994 showed that lightning activity decreases towards higher latitudes. In the distributions of Fermi and RHESSI TGFs, there is an additional decrease in detected TGFs for southern latitudes, caused by lacking detections from the platforms' passage through the SAA [Grefenstette et al., 2009].

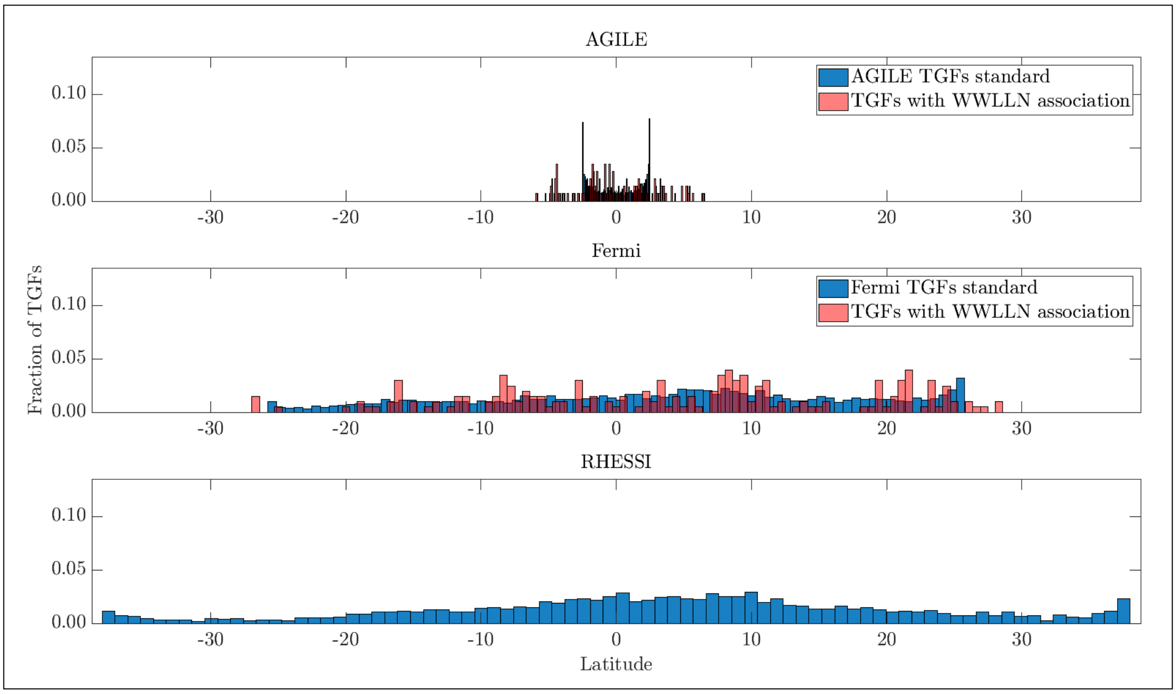

Figure 5.3: Latitudes of the TGFs detected by AGILE, Fermi and RHESSI.

5.1.4 Ocean, coast and land occurrence

Figure 5.4 displays the distance from the TGF locations to the coastline, using WWLLN locations, where negative distance occurs over land areas, and positive distance over water bodies. This distance was determined using the Global Self-consistent, Hierarchical, High-resolution Geography Database (GSHHC), which uses a 1×1 arc minute grid of the Earth and contains computed coastline distances. The majority of the TGFs are found at very close distances to the coastline. The warm coastal areas in the equatorial regions are where thunderclouds are most commonly found, as these conditions are ideal for strong convection. The distribution of the AGILE TGFs shows a larger fraction of detections over land areas, and could reflect the time spent over Africa. The distributions of Fermi TGFs indicate a larger fraction of TGFs detected over ocean areas. This might be another consequence of the orbital differences between the two satellites, which causes Fermi to cover a much larger area than AGILE.

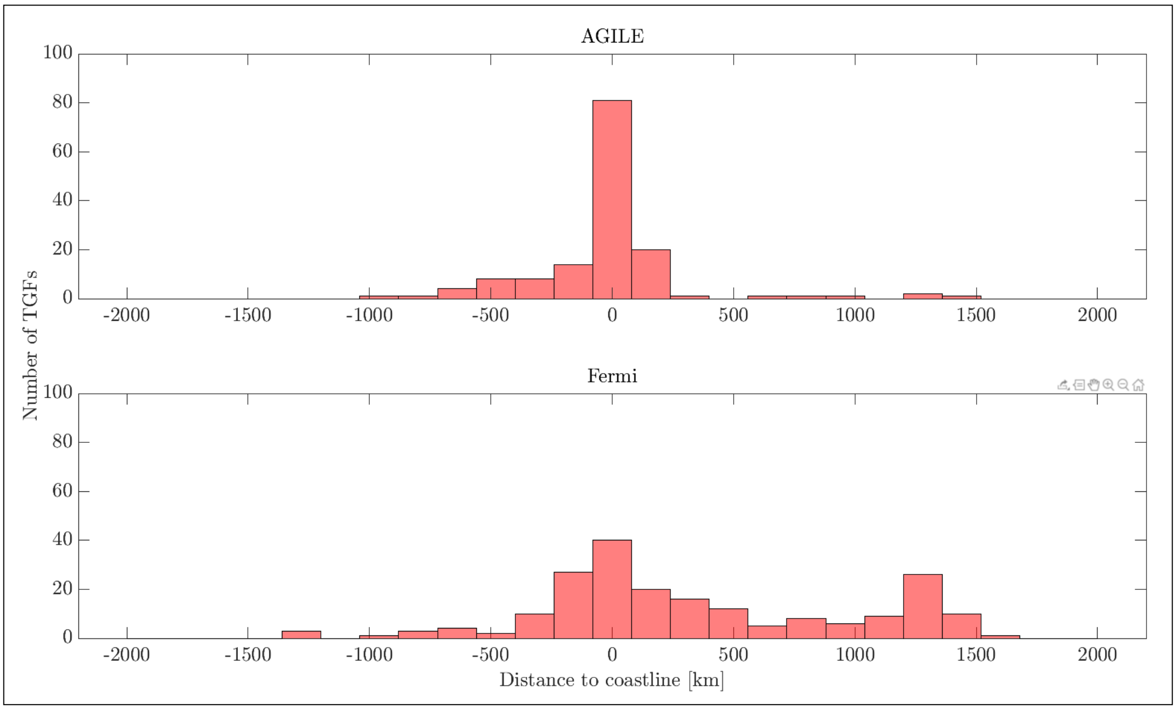

FIGURE 5.4: Distribution of the distance to the coastline for the TGFs detected by AGILE and Fermi, using WWLLN locations. Negative distances indicate detections over land areas.

5.1.5 Durations and number of counts

The TGF catalog for AGILE defined the TGF duration as t_{50}, and was found by using the maximum likelihood technique [Connaughton et al., 2013]. Because t_{50} is less affected by uncertainties from low counts rates and background counts in the TGF tail, t_{50} was used rather than t_{90} [Connaughton et al., 2010]. The distribution of the t_{50} duration of AGILE TGFs is shown in Figure 5.5, with red bars displaying the sample with WWLLN associations. Figure 5.5 indicates that the short TGFs were more likely to have a WWLLN association. The median t_{50}-duration of the TGFs in the standard sample of AGILE TGFs was 57 μs, which is smaller than the 86 μs found for the sample described by Marisaldi et al., 2015 with the new configuration. The median t_{50}-duration of the TGFs in the sample with WWLLN associations was 30 μs.

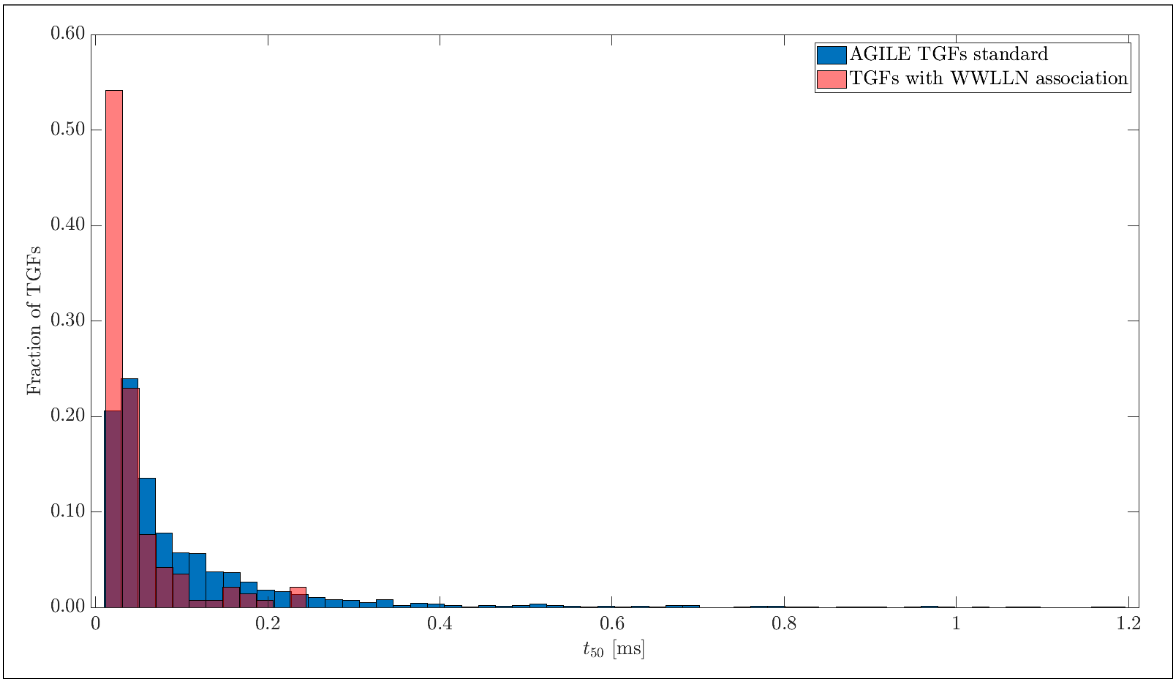

FIGURE 5.5: Distribution of the t_{50} duration from the AGILE catalog.

The durations of TGFs detected by Fermi (Figure 5.6) were given in the catalog as the width of the discovery bin, which denotes the interval where Fermi's off-line search program detected the highest statistical significance over 16 discrete timescales [Roberts et al., 2018], and is used as an approximation for the TGF duration. The median width of the discovery bin for the standard sample of Fermi TGFs was 0.2 ms, and the median for the sample of TGFs with WWLLN associations was 0.14 ms. The distribution in Figure 5.6 implies, similar to the distribution of durations for AGILE TGFs, that the shortest TGFs are more likely to have WWLLN associations. As reported by Roberts et al., 2018 and Connaughton et al., 2013, dead time effects are prevalent for Fermi TGFs, including weak TGF events found in the off-line search, and affect the duration distributions.

The AGILE and Fermi durations (t_{50} and width of discovery bin, respectively) both have a peak at less than 100 μs, The narrow peak in the Fermi duration, without the long tail of the AGILE duration, could be due to the off-line search of Fermi events being more sensitive to shorter durations [Briggs et al., 2013]. The differences in the duration and number of counts for AGILE and Fermi TGFS are largely due to dead-time effects, which gives a bias towards longer TGFs. The dead-time per count is larger for AGILE than for Fermi [Marisaldi et al., 2015], and accounts for the tail seen in Figure 5.5.

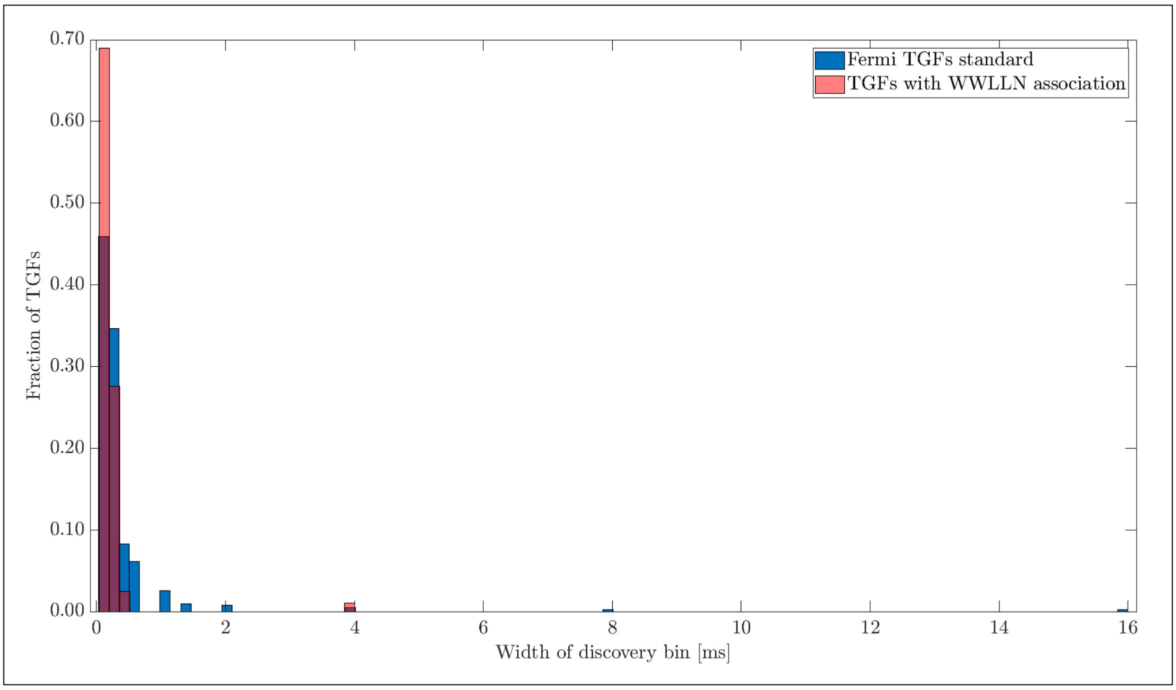

FIGURE 5.6: Distribution of the width of the discovery bin for Fermi TGFs.

Figure 5.7 shows the distribution of the number of counts detected for AGILE TGFs. The number of counts detected for each TGF were provided by the AGILE catalog, and found using the maximum likelihood technique. The number of counts detected for the AGILE TGFs was typically between 10 and 20, with a median 15 counts for the full sample of TGFs, and a median 12 counts for the sample with WWLLN associations. The distribution of the number of counts for the Fermi TGFs is shown in Figure 5.8. The number of counts for these TGFs were found from the counts recorded by Fermi's BGO 0 within the discovery bin, as provided by the Fermi catalog. The number of counts detected for Fermi TGFs was typically <10 counts. By also considering the counts recorded in Fermi's BGO 1 and the counts recorded in the NaI detectors summed, the median number of counts rises to 56, with a peak in the count distribution around 20-40 counts, reflecting the larger effective area of the Fermi NaI detectors.

The distributions of AGILE and Fermi counts (within the discovery bin) both show that the majority of the detected TGFs contain few counts, and that TGFs with few counts are more likely to have WWLLN associations. Shorter TGFs have a tendency to produce larger peak current moments, and emit more energy at higher frequencies. This is of importance for WWLLN detections, as WWLLN has a frequency threshold of >6 kHz [Connaughton et al., 2013].

A comparison to ASIM TGF durations and number of counts will be made in subchapter 5.2.2, after presenting the core duration distribution.

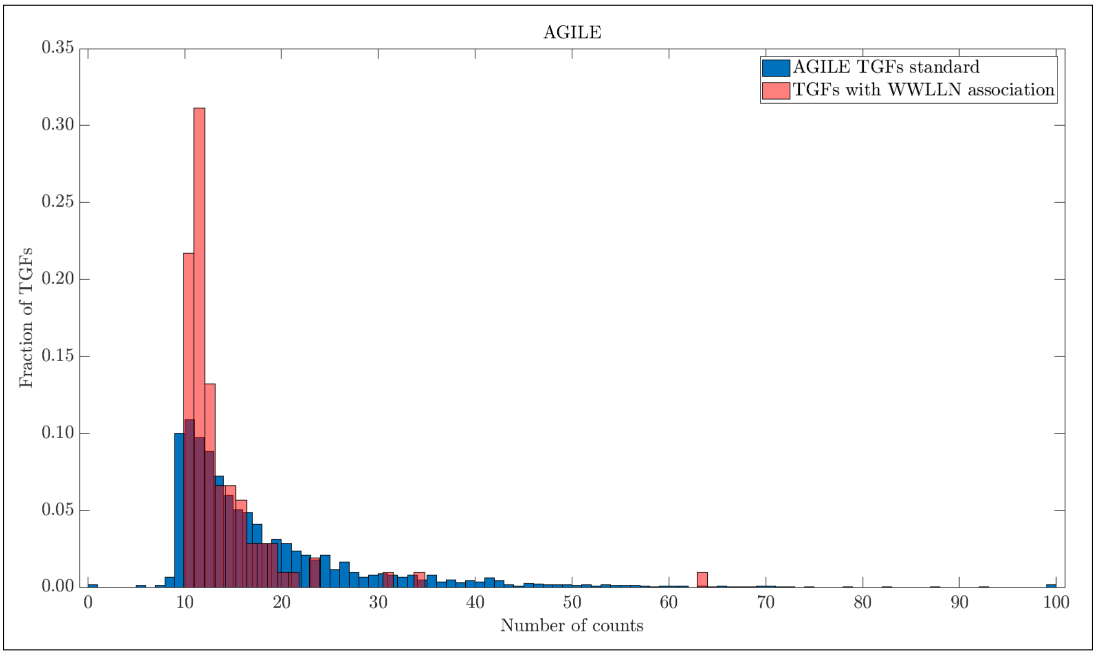

FIGURE 5.7: Distribution of the number of counts detected for AGILE TGFs.

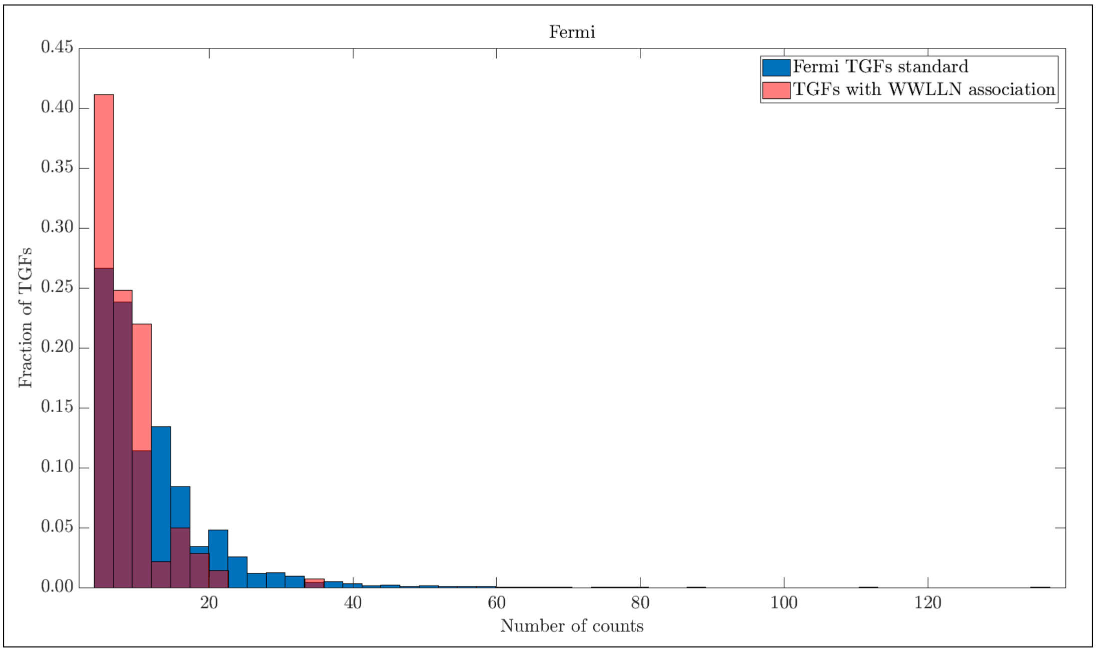

FIGURE 5.8: Distribution of the number of counts detected for Fermi TGFs.

5.2 Time sequence of TGFs and optical pulses detected by ASIM

The instruments of ASIM allow for investigating the duration of TGFs and optical pulses from lightning, as well as the time sequence of TGFs and the associated main optical pulses. This section addresses the core durations found for ASIM TGFs, the delay of the optical pulses detected by MMIA, and how these are related.

From June 2018 to March 2019, 95 TGFs (geographical distribution shown in Figure 5.9) with associated optical data were detected by ASIM. Of these 95 TGFs, 39 had a clear optical association and were used to investigate the time sequence of TGFs and the associated main optical pulses.

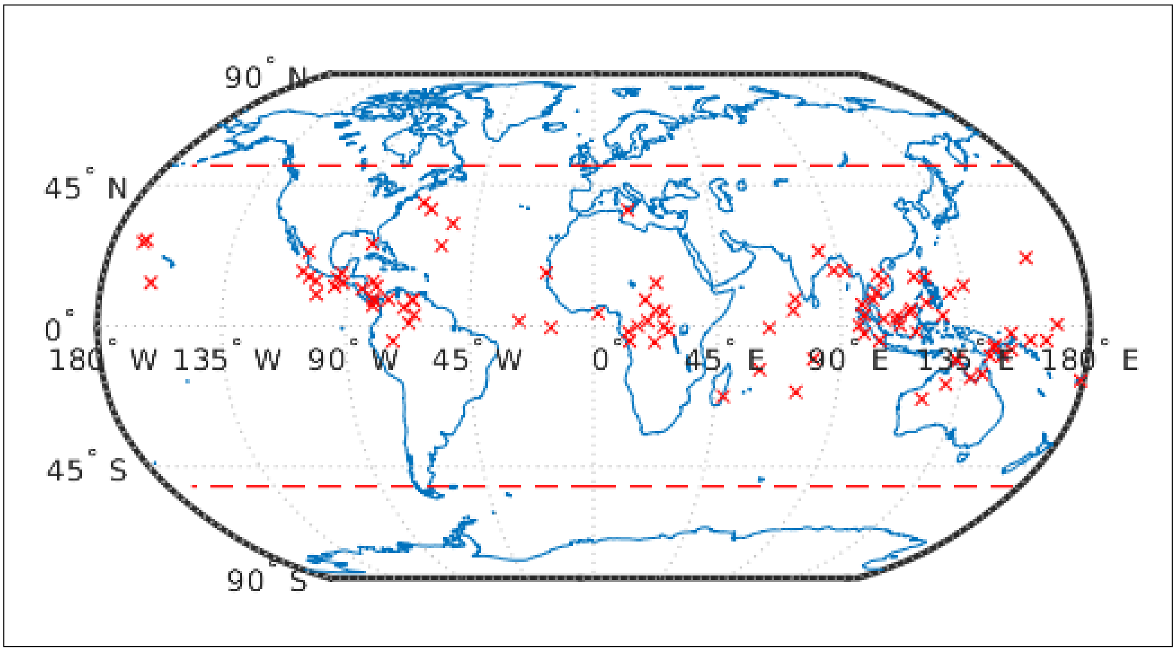

FIGURE 5.9: Global distribution of the 95 TGFs (red crosses) focused on in this thesis, using the location of the ISS footpoint at the time of the TGF detection. The dashed line indicates the latitude band imposed by the orbital inclination of the ISS.

5.2.1 Lightning network associations

Lightning network data from WWLLN and Vaisala were used to ascertain that the optical pulses categorized as clear optical associations to the TGFs were within the FOV of MMIA. The lightning network data were also used to further investigate the optical pulses initially categorized as unclear optical associations. Of the original list of 95 TGFs with optical data, 57 were categorized as having either a clear or an unclear optical association. Vaisala detections could be aligned in time with at least two optical pulses detected by MMIA (subchapter 4.2.4) for 30 events in the clear or unclear optical association categories, within 420 km of the ISS footpoint. The other TGFs in these categories typically had optical activity consisting of a single peak, or too few sferics near the TGF time, making any alignment with Vaisala associations uncertain. All the TGFs in the clear optical association category had lightning activity detected by Vaisala and/or WWLLN within the FOV <20 ms from the ASIM TGF time. The TGFs that were categorized as having no associated optical activity in MMIA (where there was no increased optical activity within ±2-3 ms of the TGF detection by MXGS), were found to have lightning sferics outside the MMIA FOV. The TGFs categorized as unclear optical association events had lightning network associations in the outskirts of the MMIA FOV. Figure 5.10 shows the distribution of the distance from the ISS footpoint to the location of the Vaisala association, for the 30 clear or unclear optical association TGFs that could be aligned in time using at least two peaks in the MMIA data.

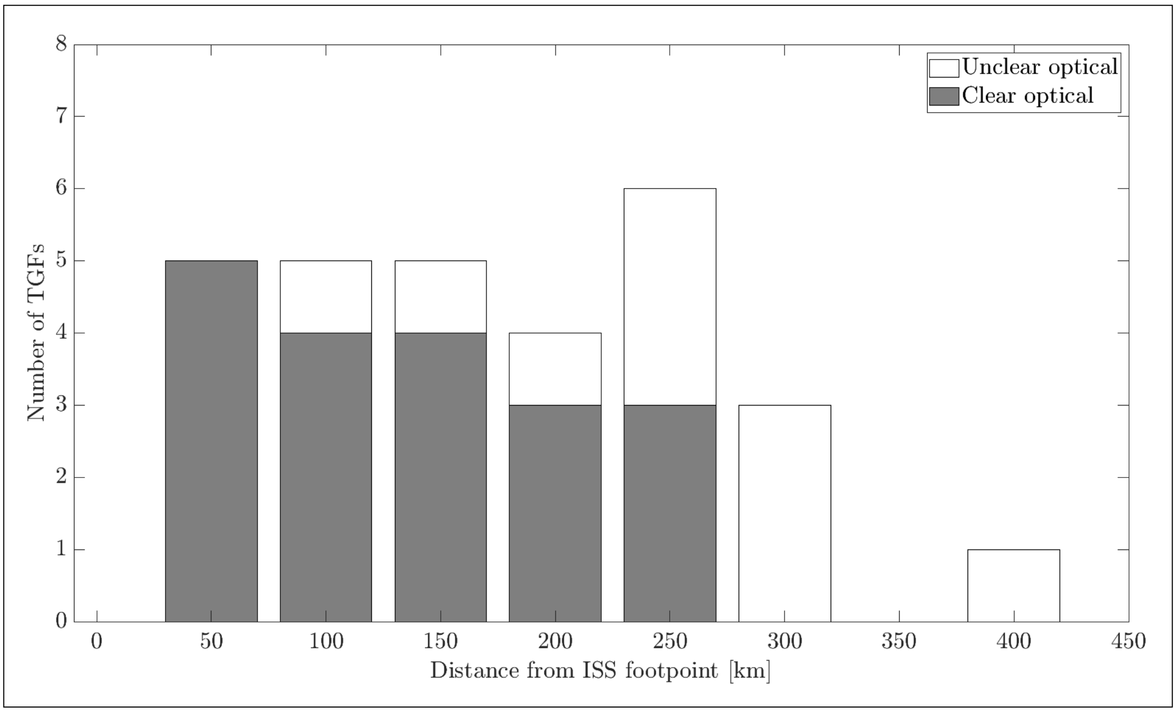

Figure 5.10: Distribution of the distance to the ISS footpoint from the Vaisala matches (stacked barplot), in 50 km bins.

5.2.2 Duration of TGFs

Figure 5.11 shows the distribution of the TGF durations found using the separation criteria outlined in subchapter 4.2.2. Table 5.1 shows how different separation criteria (40, 50, 60 and 70 μs) resulted in splits in the HED BGO counts where the CZT counts indicated a continuous event (causing the exclusion of counts that should be part of the TGF), and how the criteria could also lead to the inclusion of counts that appeared isolated from the event. A separation criteria could therefore either lead to the inclusion of too few or too many counts when determining the duration of a TGF. Table 5.1 shows that using 40 or 70 μs as separation criteria would lead to more incidents of including too few or too many counts, respectively, when determining the duration. This suggests that if applying the method of separation criteria (subchapter 4.2.2) for determining TGF durations, 50 or 60 μs should be used as separation criteria.

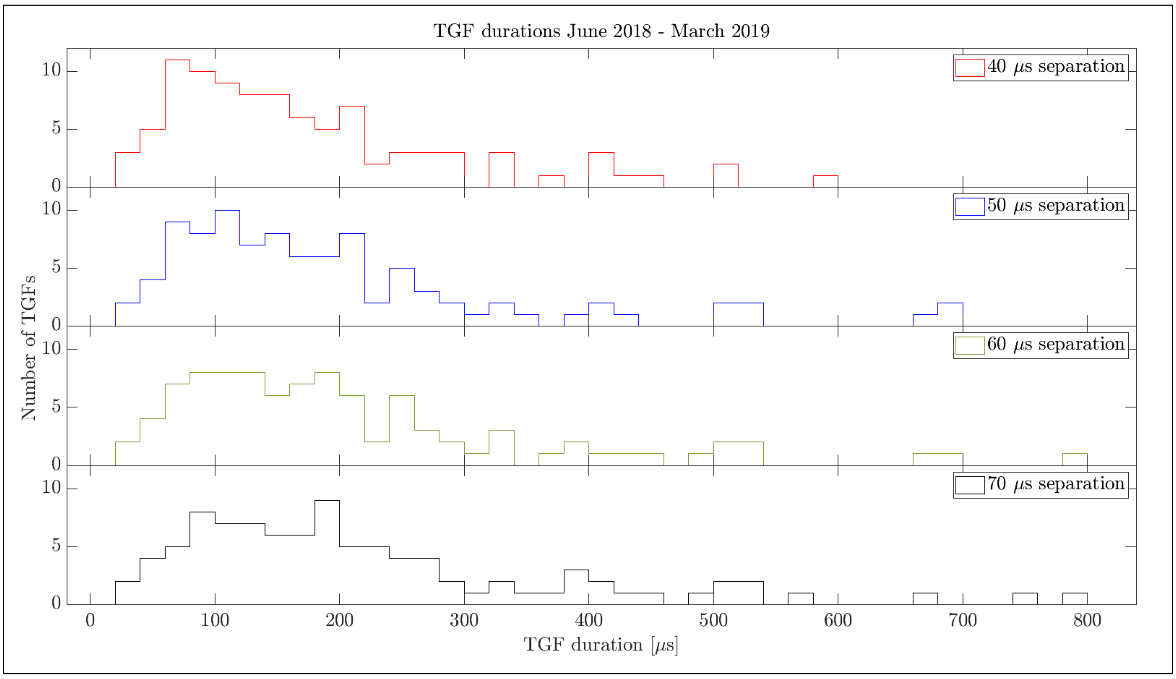

FIGURE 5.11: TGF durations for March 2018 - April 2019, using the separation criteria outlined in subchapter 4.2.2, in 20 μs bins.

The method of using a core duration was selected over the method using only separation criteria, as the core duration would include all counts that would be separated by the gaps of counts >50 μs only seen in HED. The core duration would also eliminate any outliers before or after the main portion of the TGF.

Table 5.1: Number of events where the separation criteria excluded TGF counts or included isolated counts

Separation criteria	**Exclusion of TGF counts**	**Inclusion of isolated counts**
40 μs	30	-
50 μs	16	-
60 μs	9	6
70 μs	4	14

The distribution of the core durations of the 95 TGFs focused on in this thesis is shown in Figure 5.12. A bin size of 20 μs was selected as it is half the minimum duration found amongst the ASIM TGFs. The median core duration of the whole sample from June 2018 to March 2019 was ~108 μs, and the median core duration for the sample with a clear optical association was 92.5 μs.

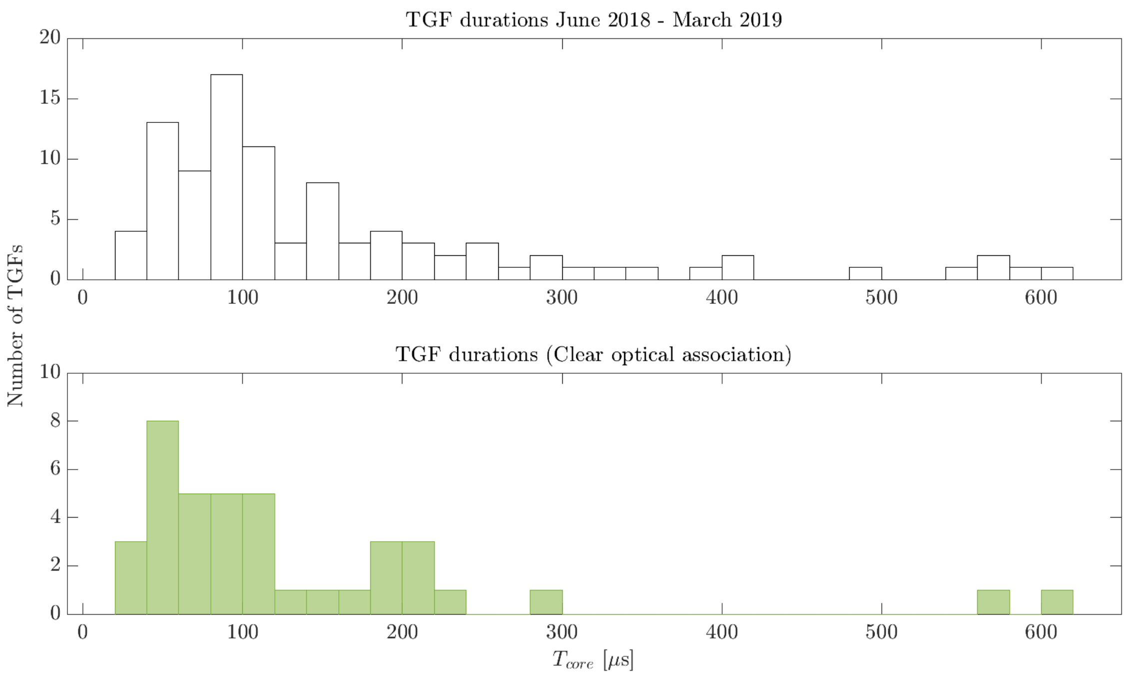

Figure 5.12: TGF durations for June 2018 - March 2019, in 20 μs bins, for the whole sample of 95 TGFs in the top panel, and the sample of 39 TGFs with clear optical associations in MMIA in the lower panel.

The sharpest peak in the core duration was the bin at 80-100 μs for the full sample of 95 TGFs, but at the 40-60 μs bin for the sample of TGFs with a clear optical association. To have a basis for comparison of ASIM TGF durations and AGILE TGF durations, a t_{50}-duration was found for the ASIM TGFs (Figure 5.13), using 50% of the counts that were separated by <100 μs (using the criteria outlined in subchapter 4.2.2 with 100 μs separation). 100 μs was selected as the separation criteria to ensure that any relevant counts were taken into account. The majority of the TGFs in the clear optical association sample had a t_{50}-duration <40 μs, with a median of ~37 μs. For the full sample of 95 TGFs, the peak in the t_{50} duration was also found in the 20-40 μs bin, with a median of ~45 μs. This is shorter than both the median t_{50}-duration found for AGILE TGFs, and the Fermi durations that were measured to several hundred microseconds. The capabilities of HED allow for the identification of TGFs with very short durations (<20 μs) and of TGFs with few counts (<10 counts) [Østgaard et al., 2019a]. The detection capability of ASIM is substantially greater than for the other spacecrafts because of the large effective area of ASIM, as well as the favorable low-orbit.

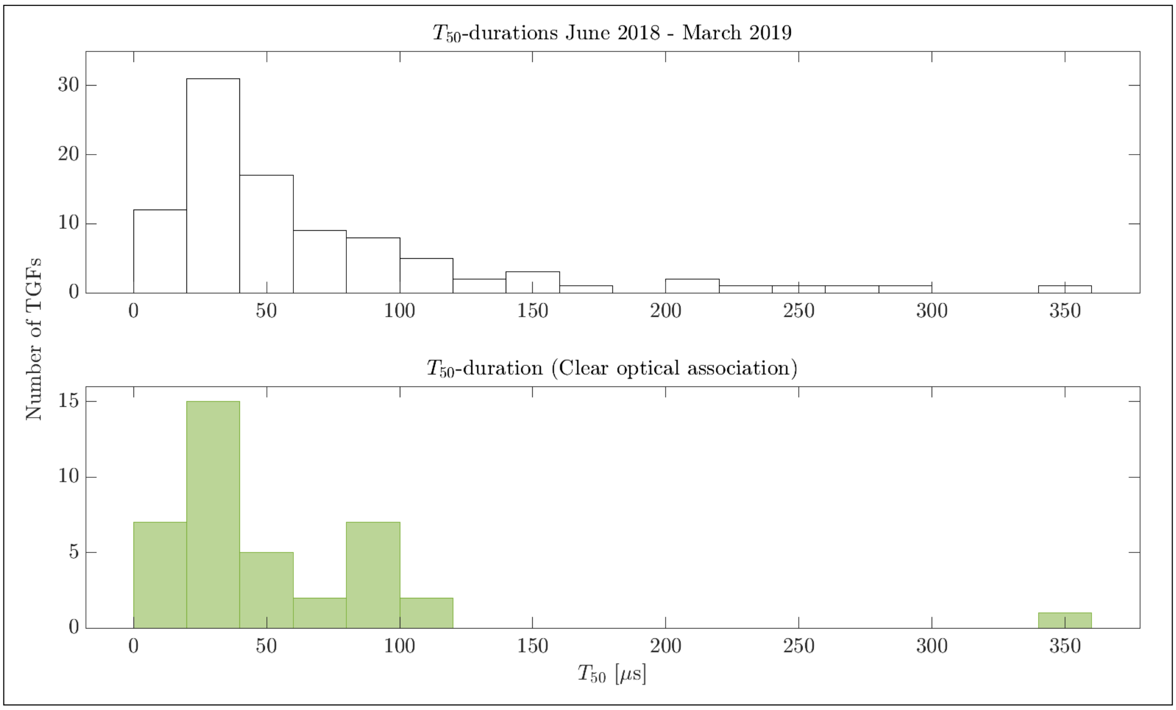

FIGURE 5.13: T_{50}-durations for the 95 TGFs (top panel) and for the TGFs with a clear optical association (lower panel), in 20 μs bins.

For the Fermi and AGILE TGFs, the durations were determined by the use of a discovery bin for Fermi TGFs and the use of maximum likelihood technique to find the t_{50}-duration of AGILE. The method of using a core duration is based on detector counts, and hence depends on the number of counts detected for the TGF. The advantage of applying a core duration is that any outliers will be eliminated, but when the number of counts gets substantially low, outliers are less likely to be removed by applying the core duration.

Figure 5.14 shows the distribution of the number of HED counts detected within the core duration. For the full sample, there is a peak in the number of counts in the 20-40 bin. The majority of the events have <60 counts, with a median of 48 counts. The TGFs with a clear optical association show two peaks in the 40-60 counts and 80-100 counts bins, This is a considerably higher amount of counts than detected for AGILE TGFs and Fermi TGFs (subchapter 5.1.5). The differences between the two samples in Figure 5.14 is caused by more weak TGFs being included in the full sample. These TGFs were typically located further from the ISS footpoint, whereas the TGFs in the clear optical association category are found within the MMIA FOV, resulting in a bias towards more HED counts.

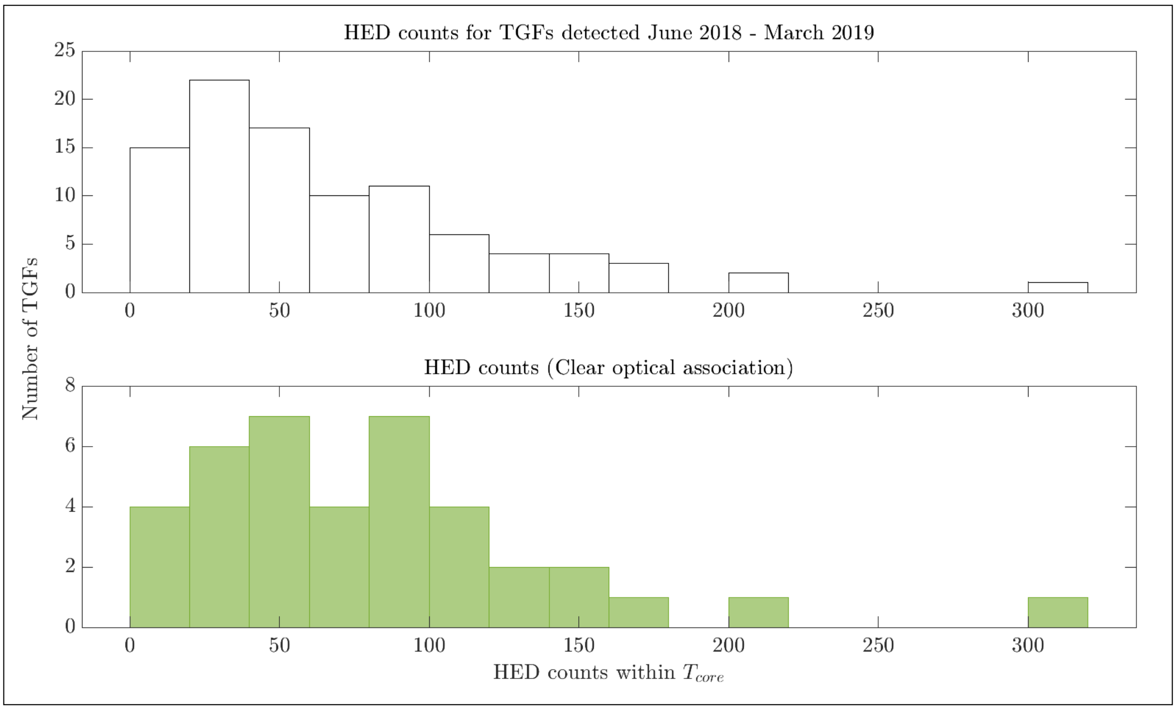

FIGURE 5.14: HED counts within T_{core} for the 95 TGFs in the top panel, and for the TGFs with a clear optical association in the lower panel, with 20 counts bins.

5.2.3 Onset of optical pulses

Figure 5.15 shows an example of a TGF with a clear optical pulse that can be seen in both the 337 nm and the 777.4 nm band, with the HED counts presented in a bar plot. Using the methods described in Chapter 4, the onsets of the main optical pulses in MMIA were approximated using a double linear method (subchapter 4.2.3). The distribution of the onsets of the main optical pulses relative to the onset of the TGF detected by MXGS is shown in Figure 5.16, given in 160 μs bins due to the relative timing uncertainty. The onsets found by visual inspection are shown by a dashed line, and were determined through repeated visual inspections. Most of the onsets of the optical pulses were delayed by <500 μs relative to the onset of the TGF, with the median delay being $\sim$190 μs. Onsets of the optical pulses found by eye indicate a similar delay of the optical pulse, with a median delay of 139 μs.

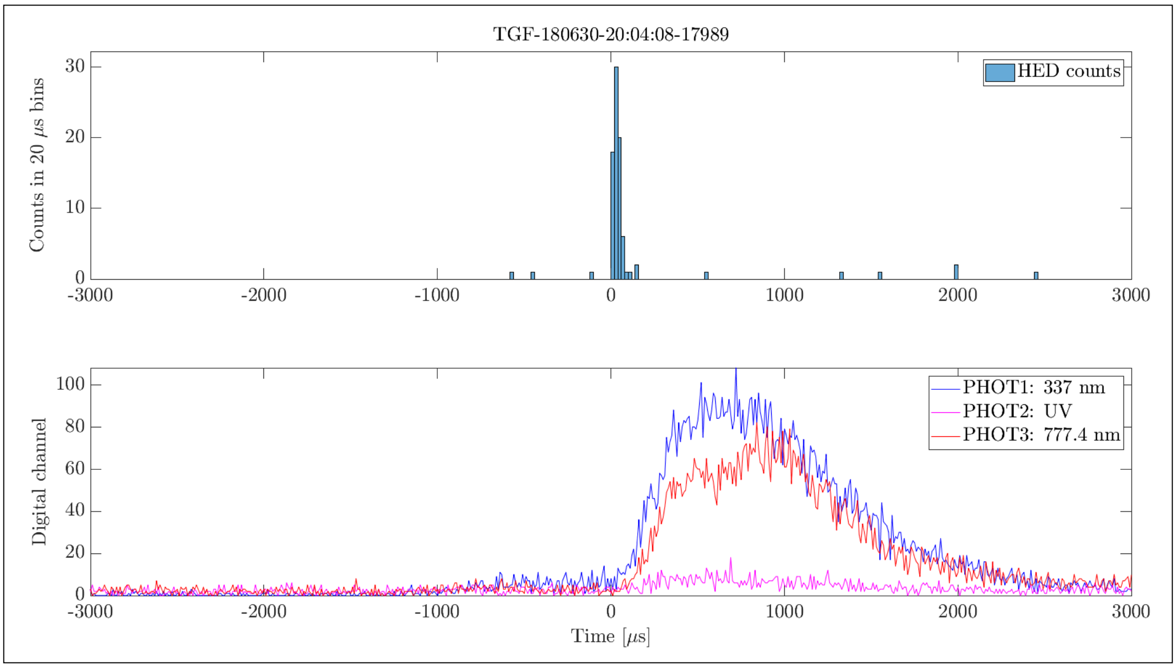

FIGURE 5.15: HED counts (top panel) and digital channels vs. time (bottom panel) plots for a TGF with a clear optical pulse association. The HED counts are sorted in 20 μs bins.

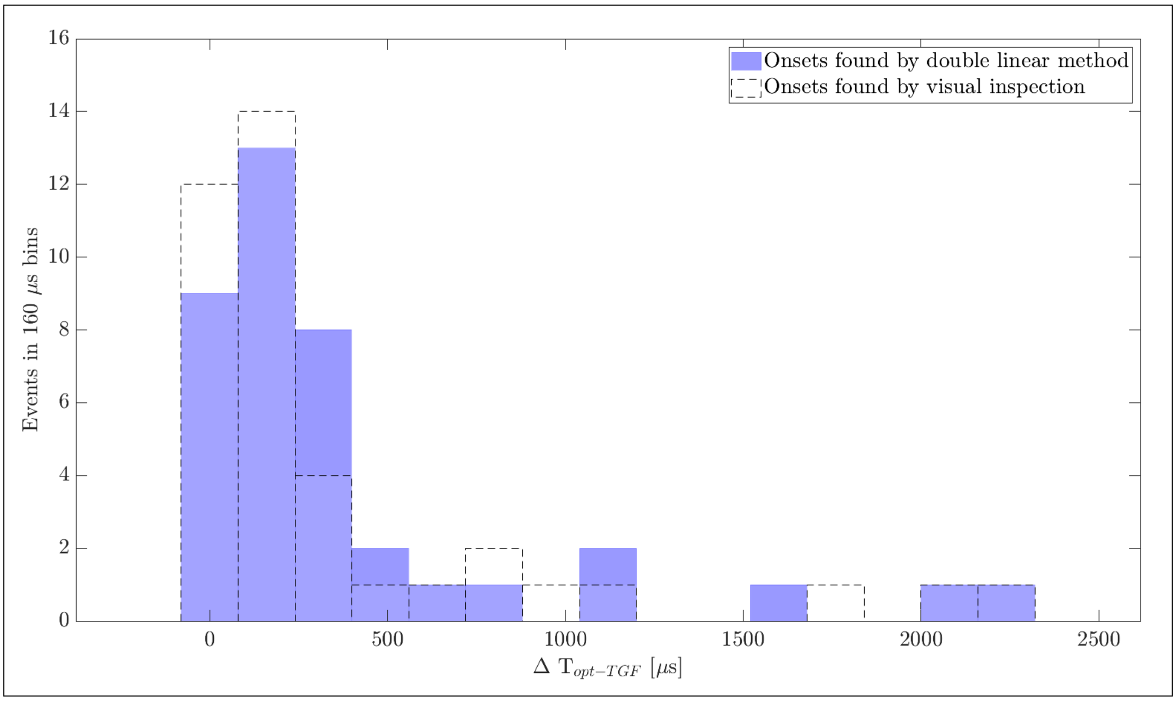

FIGURE 5.16: Onsets of the main optical pulses relative to the onset of the TGFs, in 160 μs bins, using a double linear method for determining the onsets (blue bars), and by visual inspection (non-solid line).

The criteria for determining the onset of the main optical pulse, outlined in subchapter 4.2.3, were used to determine a range of possible delays of the main optical pulse relative to the TGF onset, to estimate an uncertainty of the delay. The double linear method imposed an uncertainty not only on determining the onset of the optical pulse (and hence the delay of the optical pulse relative to the TGF), but also on the selection of a range of possible onsets. The uncertainty of the method arises both from the line extrapolated through the lightning leader activity and from the line through the approximately linear increase of the main optical pulse (subchapter 4.2.3).

Figure 5.17 shows the distribution of the estimated ranges of uncertainty for each delay of the main optical pulse with respect to the onset of the TGF detection in MXGS. The average estimated range of uncertainty for the 39 events with a clear optical association was found to be ~25 μs, which is less than half the relative timing uncertainty of ASIM between June 2018 and March 2019. Nearly all the estimated ranges of uncertainty, and hence the uncertainty imposed by the double linear method, are less than the relative timing uncertainty of ±80 μs. This estimation of a range of uncertainty is also affected by how the region of likely onsets is chosen. For TGFs detected after April 1st 2019, when the relative timing uncertainty decreased to ±5 μs, the double linear method would impose such a substantial uncertainty on the delays of the optical pulses detected in MMIA that another method should be used for finding the onsets of the main optical pulse (chapter 6).

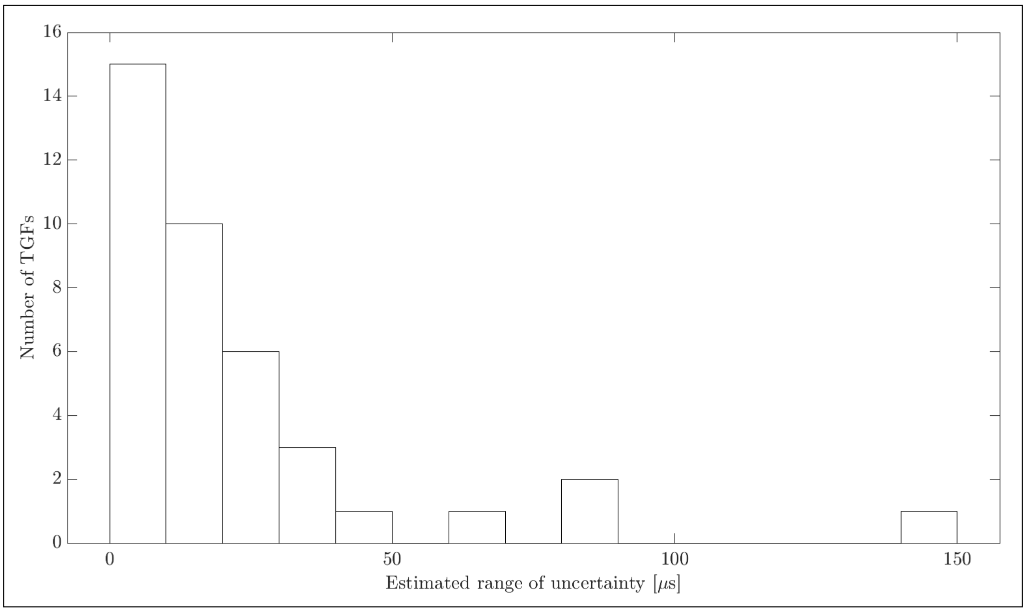

FIGURE 5.17: Estimated range of uncertainty of onsets for the events in the clear optical association category, in 10 μs bins.

5.2.4 Relation between TGF duration and onset of the optical pulse

The majority of the main optical pulses had onsets within 500 μs of the TGF onset (Figure 5.16), and the majority of the TGFs had core durations <120 μs (Figure 5.12), with the sharpest peak in the duration being 40-60 μs. Figure 5.18 shows the core duration of the TGFs vs. the delay of the optical pulse, given as the difference between the onsets of the optical pulse and TGF. Errorbars were not included in this plot, as all the delays have the same timing uncertainty of ±80 μs. Figure 5.19 shows the same distribution, using TGF duration and onset of the optical pulse found by visual inspection. Figure 5.20 focuses on the main fraction of events from Figure 5.18 (considering the other events as outliers), to further investigate the relationship between TGF duration and delay of the associated optical pulse, resulting in a correlation coefficient of ∼0.6. This could suggest a linear relationship between TGF duration and delay of the associated optical pulse. For the same narrow region of Figure 5.19, where both the TGF duration and the onset of the optical pulse were found by visual inspection, the correlation coefficient was found to be as low as ∼0.1. If instead selecting the region of Figure 5.19 where the main fraction of the events are found (x ϵ $[-5, 400]$, y ϵ $[0, 300]$), the correlation coefficient is ∼0.6.

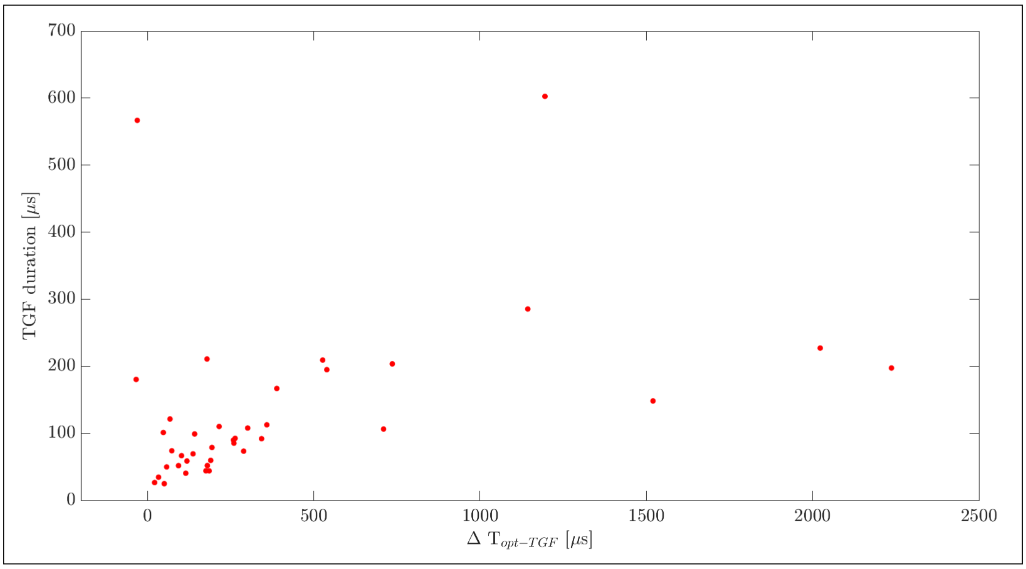

FIGURE 5.18: TGF duration vs. the difference in onsets of the optical pulse and the TGF, using a core duration (subchapter 4.2.2) and the optical pulse onset found by the double linear method (subchapter 4.2.3).

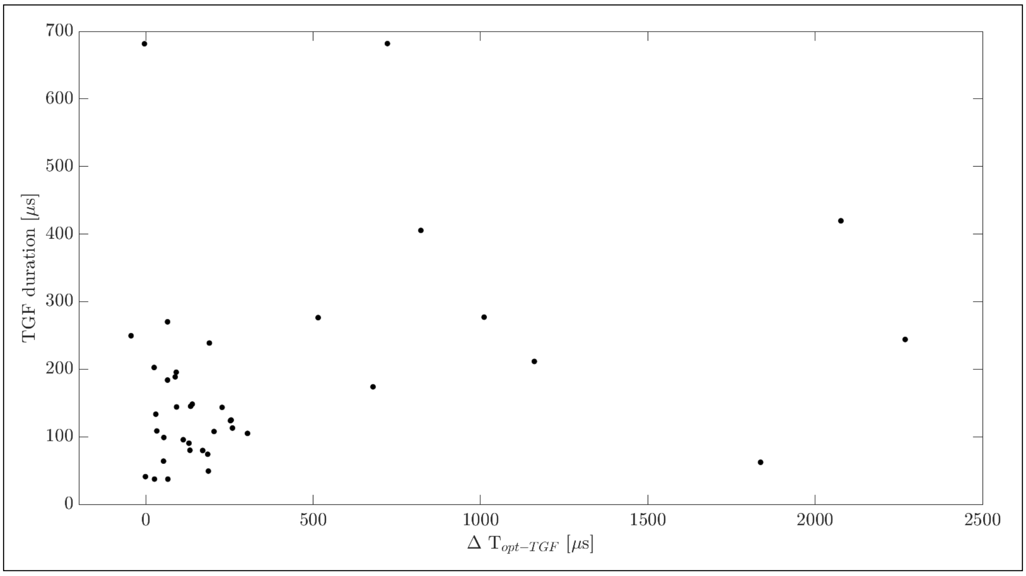

FIGURE 5.19: TGF duration vs. the difference in onsets of the main optical pulse and the TGF, using a duration and optical pulse onset found by visual inspection.

The results from visual inspection were included here for comparison with the results from the core duration and the double linear method. Visual inspection is a highly subjective approach, although the included results were obtained after repeated inspections and after discussions with members of our group. The double linear method also imposes an uncertainty to the results, in several parts of the method outlined in subchapter 4.2.3. The first uncertainty arises from the selection of the most linearly increasing region of both the pre-activity and the beginning of the optical pulse, as this was a subjective selection. Consequently, the extrapolation of lines through these regions has an added uncertainty, although it is less than the relative MXGS-MMIA timing uncertainty.

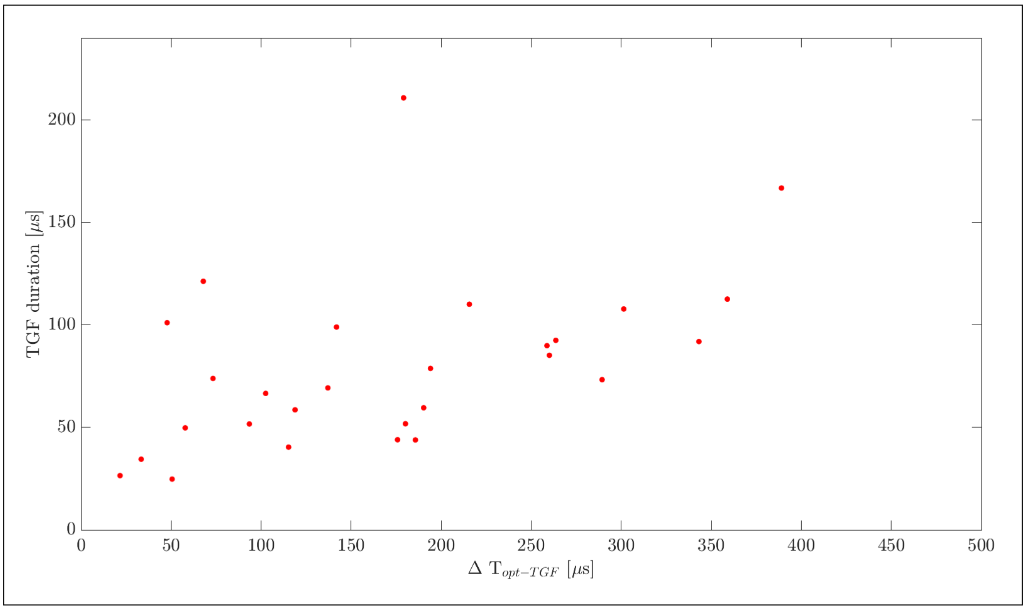

FIGURE 5.20: TGF duration vs. the difference in onsets between the optical pulse and the TGF, using TGF core duration and the optical pulse onset found using the double linear method, focusing on a narrow region (x ϵ $[0, 500]$, y ϵ $[0, 240]$) of Figure 5.18.

Plots of TGF duration vs. delay of the main optical pulse, indicate that short TGFs tend to have shorter delays of the associated optical pulse. Figure 5.16 showed that the typical delay of optical pulses was <500 μs, with a fraction of the TGFs and the optical pulses occurring simultaneously (within the relative timing uncertainty of ± 80 μs). This is in agreement with findings by Østgaard et al., 2013, for the first observation of a simultaneous TGF and optical lightning. They reported that the TGF occurred in the initial stage IC lightning, deep within the thundercloud, before the leader extended to the cloud top.

The very long delays seen for some of the optical pulses detected by MMIA, for both the pre-activity region and the main optical pulse, could be due to the sources of the TGFs being further from the

ISS footpoint (although still within the FOV of MMIA), or the influence of cloud scattering. Cloud scattering can also affect the rise time of pulses in PHOTs 1 and 3 [Østgaard et al., 2019a], but can only provide a delay of ~100 μs [Light et al., 2001], and therefore does not account for the very long delays seen for some of the optical pulses. The long delays could indicate that these TGFs were produced deep within the thunderclouds, and hence experience both optical and Compton scattering. Atmospheric scattering can also impact the TGF duration, which could be prolonged by Compton scattering in the atmosphere. High-energy photons experience less Compton scattering, and give durations closer to the TGF duration at the source [Connaughton et al., 2013].

The time sequence of the pre-activity seen in MMIA and the TGF detection by MXGS, indicates that the TGFs were produced towards the later stages of leader development (Figure 5.21), and before onset of the main current pulse. Some exceptions were evident for events with long delays of the associated optical pulse. These also appeared to have long-lasting lightning leader activity around the time of the MXGS detection (Figure 5.22), indicating production of TGFs around the middle of the leader development, consistent with Cummer et al., 2015. By analysing Fermi TGFs, and using lightning geolocation data from the NLDN, Pu et al., 2019, supported the results by Cummer et al., 2015, showing that at least some TGFs are produced after the leader initiation, but before it fully extends vertically.

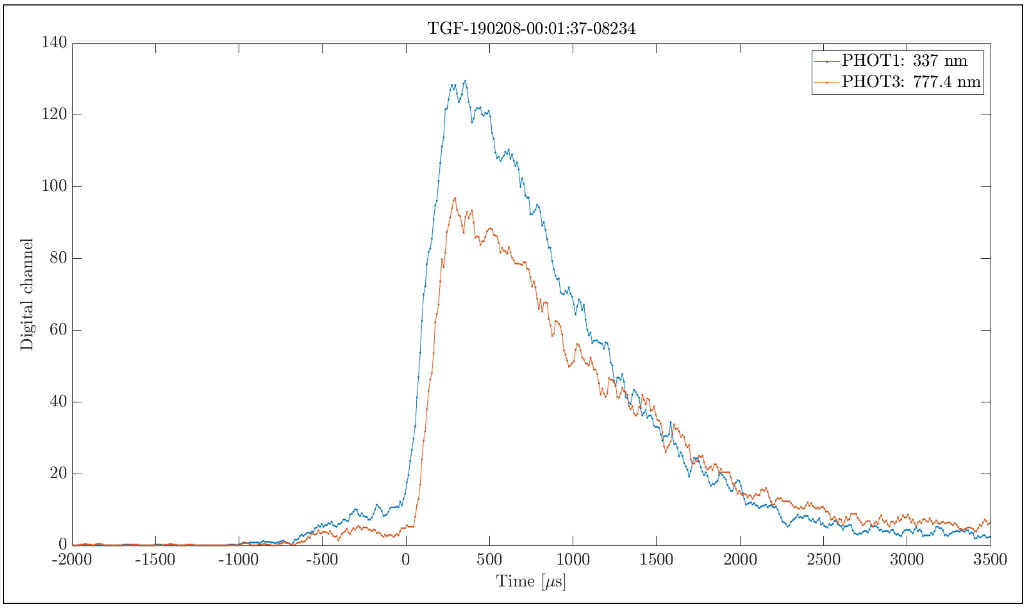

FIGURE 5.21: Detections in PHOTs 1 and 3 (smoothed) of MMIA around the time of TGF-190208-00:01:37-08234 detected by MXGS. Indications of lightning leader activity can be seen before 0 μs, which denotes the time of the first photon of the MXGS detection.

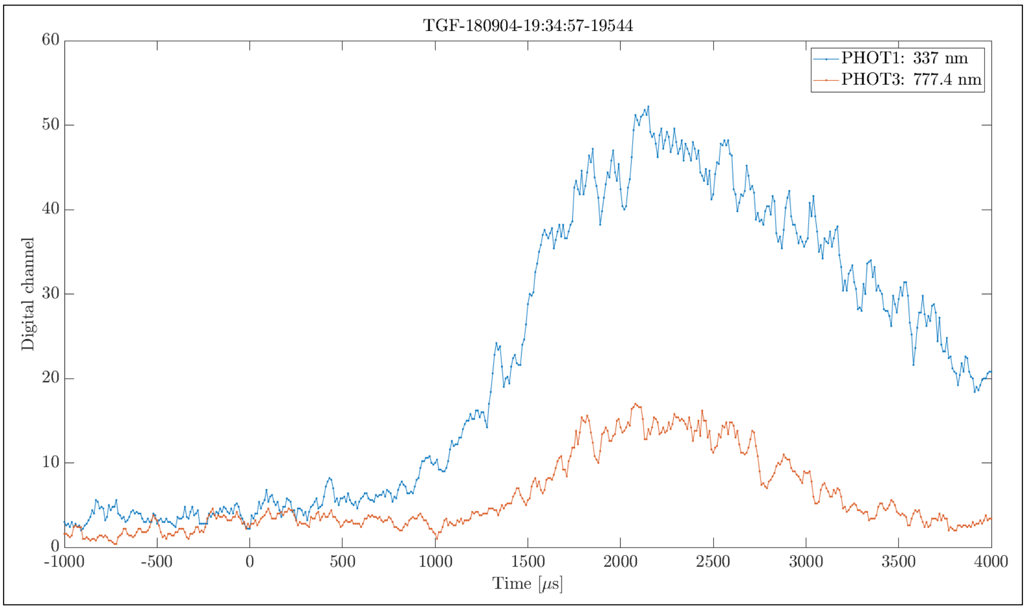

Figure 5.22: Detections in PHOTs 1 and 3 (smoothed) of MMIA around the time of TGF-180904-19:34:57-19544 detected by MXGS. Indications of lightning leader activity can be seen after 0 μs, which denotes the time of the first photon of the MXGS detection.

The time sequence of TGFs occurring before the main lightning stroke is in agreement with the time sequence reported by Shao et al., 2010, for RHESSI TGFs, using the Los Alamos Sferic Array (LASA). Shao et al., 2010, suggested that TGFs are produced on average 0.6 ms prior to the main lightning field change pulses. In comparison, the delay of the onset of the optical pulse of ASIM TGFs was on average ∼0.4 ms. Shao et al., 2010, also suggested that TGFs could be related to small discharge pulses rather than the main pulses, as field changes detected by LASA showed that the TGFs occurred 0.4-0.6 ms before the major field changes. They further suggested that these small pulses were produced during the stepped leader processes within the thunderclouds. Lu et al., 2010, using RHESSI TGFs and the North Alabama Lightning Mapping Array (LMA), suggested that TGFs are produced between the negative lower and the upper positive charge regions of the thundercloud. They argued that TGFs are produced during the early stages of upward propagation of the negative lightning leader, after the IC flash onset. Lu et al., 2010, also showed that the RHESSI TGFs were produced in association with compact IC flashes <30 km from the subsatellite point.

Celestin and Pasko, 2011, suggested that TGFs are produced in the strong electric field ahead of leaders and before the lightning stroke. The time sequence of the TGF detection in MXGS, the pre-activity seen in MMIA-data and the delay of the main optical pulse, suggests that TGFs are likely to be produced towards later stages of leader development. This occurs before the current pulse heats up the channel to emit an optical pulse.

There appears to be a correlation between the TGF duration and the delay of the associated optical pulse. The TGFs are believed to be produced in the strong fields ahead of streamers when this field exists, but stops once the current pulse collapses the field ($\sim$120 μs before the optical pulse). This implies that TGFs with longer durations occur earlier before the optical pulse than the shorter TGFs, which appear to occur closer to the onset of the optical pulse. This relation cannot be accurately determined with the relative timing uncertainty of ± 80 μs for the time period (June 2018 - March 2019) used in this thesis, but the relative timing uncertainty of ± 5 μs that has since been implemented could give a better indication of this relationship.

Chapter 6

Summary and Future Work

TGFs detected by RHESSI, Fermi and AGILE all showed similar geographic distributions, with a clustering of TGFs around the continents in the equatorial region, consistent with the occurrence of thunderstorm activity. The median durations and number of counts for Fermi and AGILE TGFs are shown in Table 6.1, along with the durations and counts for ASIM TGFs.

Table 6.1: Durations and number of counts for TGFs detected by Fermi, AGILE and ASIM

	Fermi	**AGILE**	**ASIM**
TGF durations	Median width of discovery bin: 0.2 ms	Median T_{50}: 57 μs	Median T_{core}: 108 μs Median T_{50}: 45 μs
Number of counts	Median within discovery bin: 9 counts	Median: 15 counts	Median: 48 counts

Of the 95 ASIM TGFs with available optical data, 39 had a clear associated optical pulse. For 18 of the other events, there was increased optical activity in proximity to the TGF time, but it was too weak to determine an onset of the activity. This could be due to ASIM not detecting optical pulses until the flux levels increase above the instrumental threshold [Neubert et al., 2020]. For these events, lightning network data indicated lightning activity in the outskirts of the FOV.

The clear optical pulses detected by MMIA typically had onsets within <500 μs of the TGF onset, with a fraction of the optical pulses occurring simultaneously (within ±80 μs) with the TGF detection. There is an apparent correlation between TGF duration and the delay of the associated optical pulse. This implies that optical pulses associated with short TGFs tend to be less delayed than the optical pulses associated with long TGFs.

For the majority of the events, optical pre-activity was observed to start before the onset of the

MXGS TGF detection, suggesting that TGFs tend to be produced towards the later stages of leader development, before the current pulse has heated the channel to emit an optical pulse.

The methods applied when investigating the relation between duration of ASIM TGFs and delays of optical pulses detected by the photometers in MMIA, imposed uncertainties on the findings that could be improved through future work.

Suggestions for future work to improve the analysis are listed below:

Comparison of platforms

- RHESSI TGFs could be connected to WWLLN associations. This would enable a more accurate geographic comparison with AGILE and Fermi, in particular in terms of the distance from the TGFs to the coastline

Relationship between the ASIM TGF durations and the delay of optical pulses

1. TGF duration:
    - A larger sample of TGFs could be used for investigating the distributions of TGF durations and number of counts. This would allow determining the typical ASIM TGF duration and number of counts with greater power, and improve comparisons between the ASIM TGFs and the other platforms
    - An energy threshold could be applied to the HED counts in an attempt to remove the low energy photons in the Compton tail
2. Onsets of the main optical pulses:
    - To improve the estimate of the onset, a line could be extrapolated through the pre-activity and a variation, σ, relative to this line could be found. The onset could then be selected to be when σ increases sufficiently ($\sim 3\sigma$) above the pre-activity
    - A line could be extrapolated through the pre-activity, and the main optical pulse fitted with a Gaussian function. The onset could then be selected at the intersection of the line from the pre-activity and the Gaussian function
3. A more thorough investigation could be made into the lightning activity inside the FOV within 20 ms of the TGF detection, to more accurately determine which lightning activity is responsible for the optical pulse seen in MMIA
4. Further correlating of lightning network data with optical pulses, using continuous timelines of MMIA data, could be performed. This would allow for aligning more of the optical pulses from the clear optical association category with lightning network data

5. The tilt of the CEPA and the movements of the ISS could be used to more accurately find the distance from the ISS footpoint to associated lightning network detections

Bibliography

Abarca, Sergio F. et al. (2010). “An evaluation of the Worldwide Lightning Location Network (WWLLN) using the National Lightning Detection Network (NLDN) as ground truth”. In: *Journal of Geophysical Research Atmospheres* 115.18, pp. 1–11. ISSN: 01480227. DOI: `10.1029/2009JD013411`.

Albrechtsen, K. H. et al. (2019). “Observationally Weak TGFs in the RHESSI Data”. In: *Journal of Geophysical Research: Atmospheres* 124.1, pp. 287–298. ISSN: 21698996. DOI: `10.1029/2018JD029272`.

Briggs, M. S. et al. (2010). “First results on terrestrial gamma ray flashes from the Fermi Gamma-ray Burst Monitor”. In: *Journal of Geophysical Research: Space Physics* 115.7, pp. 1–14. ISSN: 21699402. DOI: `10.1029/2009JA015242`.

Briggs, Michael S. et al. (2013). “Terrestrial gamma-ray flashes in the Fermi era: Improved observations and analysis methods”. In: *Journal of Geophysical Research: Space Physics* 118.6, pp. 3805–3830. ISSN: 21699402. DOI: `10.1002/jgra.50205`.

Celestin, Sebastien and Victor P. Pasko (2011). “Energy and fluxes of thermal runaway electrons produced by exponential growth of streamers during the stepping of lightning leaders and in transient luminous events”. In: *Journal of Geophysical Research: Space Physics* 116.3, pp. 1–14. ISSN: 21699402. DOI: `10.1029/2010JA016260`.

Cember, Herman and Thomas E. Johnson (2009). *Introduction to Health Physics: Fourth Edition.* 4th ed. Vol. 35. 12. The McGraw-Hill Companies, Inc. ISBN: 9780071643238. DOI: `10.1118/1.3021454`.

Chanrion, Olivier et al. (2019). “The Modular Multispectral Imaging Array (MMIA) of the ASIM Payload on the International Space Station”. In: *Space Science Reviews* 215.4. ISSN: 15729672. DOI: `10.1007/s11214-019-0593-y`. URL: `http://dx.doi.org/10.1007/s11214-019-0593-y`.

Connaughton, V. et al. (2010). “Associations between Fermi Gamma-ray Burst Monitor terrestrial gamma ray flashes and sferics from the World Wide Lightning Location Network”. In: *Journal of Geophysical Research: Space Physics* 115.12, pp. 1–14. ISSN: 21699402. DOI: `10.1029/2010JA015681`.

Connaughton, Valerie et al. (2013). "Radio signals from electron beams in terrestrial gamma ray flashes". In: *Journal of Geophysical Research: Space Physics* 118.5, pp. 2313–2320. ISSN: 21699402. DOI: `10.1029/2012JA018288`.

Cooray, Vernon (2014). *The lightning flash: 2nd edition*, pp. 1–897. ISBN: 9781849196925. DOI: `10.1049/PBP0069E`.

Cummer, Steven A. et al. (2005). "Measurements and implications of the relationship between lightning and terrestrial gamma ray flashes". In: *Geophysical Research Letters* 32.8, pp. 1–5. ISSN: 00948276. DOI: `10.1029/2005GL022778`.

Cummer, Steven A. et al. (2015). "Lightning leader altitude progression in terrestrial gamma-ray flashes". In: *Geophysical Research Letters* 42.18, pp. 7792–7798. ISSN: 19448007. DOI: `10.1002/2015GL065228`.

Dwyer, J. R. (2003). "A fundamental limit on electric fields in air". In: *Geophysical Research Letters* 30.20, pp. 1–4. ISSN: 00948276. DOI: `10.1029/2003GL017781`.

Dwyer, J. R. and D. M. Smith (2005). "A comparison between Monte Carlo simulations of runaway breakdown and terrestrial gamma-ray flash observations". In: *Geophysical Research Letters* 32.22, pp. 1–4. ISSN: 00948276. DOI: `10.1029/2005GL023848`.

Dwyer, Joseph R. et al. (2012). "High-energy atmospheric physics: Terrestrial gamma-ray flashes and related phenomena". In: *Space Science Reviews* 173.1-4, pp. 133–196. ISSN: 00386308. DOI: `10.1007/s11214-012-9894-0`.

Fishman, Gerald J. et al. (1994). "The first BATSE gamma-ray burst catalog". In: *The Astrophysical Journal Supplement Series* 92.June, p. 229. ISSN: 0067-0049. DOI: `10.1086/191968`.

Gjesteland, T. et al. (2012). "A new method reveals more TGFs in the RHESSI data". In: *Geophysical Research Letters* 39.5, pp. 1–5. ISSN: 00948276. DOI: `10.1029/2012GL050899`.

Gjesteland, Thomas et al. (2017). "On the timing between terrestrial gamma ray flashes, radio atmospherics, and optical lightning emission". In: *Journal of Geophysical Research: Space Physics* 122.7, pp. 7734–7741. ISSN: 21699402. DOI: `10.1002/2017JA024285`.

Grefenstette, B. W. et al. (2009). "First RHESSI terrestrial gamma ray flash catalog". In: *Journal of Geophysical Research: Space Physics* 114.2, pp. 1–19. ISSN: 21699402. DOI: `10.1029/2008JA013721`.

Gurevich, A. V. et al. (1992). "Runaway electron mechanism of air breakdown and preconditioning during a thunderstorm". In: *Physics Letters A* 165.5-6, pp. 463–468. ISSN: 03759601. DOI: `10.1016/0375-9601(92)90348-P`.

Henley, Ernest M. and Alejandro Garcia (2007). *Subatomic Physics*. Singapore, pp. 303–306. ISBN: 9789812700575.

Hoinka, Klaus P. (1998). “Statistics of the global tropopause pressure”. In: *Monthly Weather Review* 126.12, pp. 3303–3325. ISSN: 00270644. DOI: `10.1175/1520-0493(1998)126<3303:SOTGTP>2.0.CO;2`.

Hutchins, M. L. et al. (2013). “Radiated VLF energy differences of land and oceanic lightning”. In: *Geophysical Research Letters* 40.10, pp. 2390–2394. ISSN: 00948276. DOI: `10.1002/grl.50406`.

Hutchins, Michael L. et al. (2012). “Far-Field power of lightning strokes as measured by the world wide lightning location network”. In: *Journal of Atmospheric and Oceanic Technology* 29.8, pp. 1102–1110. ISSN: 07390572. DOI: `10.1175/JTECH-D-11-00174.1`.

Jayaratne, E. R. et al. (1983). “Laboratory studies of the charging of soft-hail during ice crystal interactions”. In: *Quarterly Journal of the Royal Meteorological Society* 109.461, pp. 609–630. ISSN: 1477870X. DOI: `10.1002/qj.49710946111`.

Labanti, C. et al. (2009). “Design and construction of the Mini-Calorimeter of the AGILE satellite”. In: *Nuclear Instruments and Methods in Physics Research, Section A: Accelerators, Spectrometers, Detectors and Associated Equipment* 598.2, pp. 470–479. ISSN: 01689002. DOI: `10.1016/j.nima.2008.09.021`.

Lehtinen, N. G. et al. (1996). “Gamma-ray emission produced by a relativistic beam of runaway electrons accelerated by quasi-electrostatic thundercloud fields”. In: 23.19, pp. 2645–2648.

Lehtinen, N. G. et al. (1999). “Monte Carlo simulation of runaway MeV electron breakdown with application to red sprites and terrestrial gamma ray flashes”. In: *Journal of Geophysical Research: Space Physics* 104.A11, pp. 24699–24712. ISSN: 2169-9402. DOI: `10.1029/1999ja900335`.

Light, T. E. et al. (2001). “Simulations of lightning optical waveforms as seen through clouds by satellites”. In: *Journal of Geophysical Research Atmospheres* 106.D15, pp. 17103–17114. ISSN: 01480227. DOI: `10.1029/2001JD900051`.

Lindanger, A. et al. (2020). “The 3rd AGILE Terrestrial Gamma Ray Flash catalog. Part I: Association to lightning sferics”. In: *Journal of Geophysical Research: Atmospheres*, e2019JD031985. DOI: `10.1029/2019jd031985`.

Lindanger, Anders (2018). *Search for Terrestrial Gamma-ray Flashes in AGILE data by correlation with ground-based lightning measurements.* Tech. rep. Master Thesis, University of Bergen.

Lindy, N. C. et al. (2014). “The Cosmic-Ray Extensive Air Shower Environment of Thunderstorms”. In: *XV International Conference on Atmospheric Electricity, 15-20 June 2014, Norman, Oklahoma, U.S.A.* June.

Liu, Ningyu and Victor P. Pasko (2004). “Effects of photoionization on propagation and branching of positive and negative streamers in sprites”. In: *Journal of Geophysical Research: Space Physics* 109.A4, pp. 1–17. ISSN: 21699402. DOI: `10.1029/2003JA010064`.

Lu, Gaopeng et al. (2010). “Lightning mapping observation of a terrestrial gamma-ray flash”. In: *Geophysical Research Letters* 37.11, pp. 1–5. ISSN: 00948276. DOI: `10.1029/2010GL043494`.

Mackerras, D. and M. Darveniza (1994). “Latitudinal variation of lightning occurrence characteristics”. In: *Journal of Geophysical Research* 99.D5. DOI: `https://doi.org/10.1029/94JD00018`.

Maiorana, C. et al. (2020). “The 3rd AGILE Terrestrial Gamma-ray Flashes Catalog. Part II: Optimized selection criteria and characteristics of the new sample”. In: *Journal of Geophysical Research: Atmospheres*, e2019JD031986. DOI: `10.1029/2019jd031986`.

Marisaldi, M et al. (2013). “Journal of Geophysical Research : Space Physics Properties of terrestrial gamma ray flashes detected by AGILE MCAL below 30 MeV”. In: *Journal of Geophysical Research: Space Physics* 119.November 2009, pp. 1337–1355. DOI: `10 . 1002 / 2013JA019301 . Received`.

Marisaldi, M. et al. (2015). “Enhanced detection of terrestrial gamma-ray flashes by AGILE”. In: *Geophysical Research Letters* 42.21, pp. 9481–9487. ISSN: 19448007. DOI: `10.1002/2015GL066100`.

Marshall, Thomas C. and Maribeth Stolzenburg (2001). “Voltages inside and just above thunderstorms”. In: *Journal of Geophysical Research Atmospheres* 106.D5, pp. 4757–4768. ISSN: 01480227. DOI: `10.1029/2000JD900640`.

Meegan, Charles et al. (2009). “The fermi gamma-ray burst monitor”. In: *Astrophysical Journal* 702.1, pp. 791–804. ISSN: 15384357. DOI: `10.1088/0004-637X/702/1/791`.

Mezentsev, Andrew (2019). *Relative MXGS-MMIA timing.* Tech. rep. University of Bergen.

Mezentsev, Andrew et al. (2016). “Radio emissions from double RHESSI TGFs”. In: DOI: `10.1002/2016JD025111.A`.

Mezentsev, Andrew et al. (2018). “Spectral Characteristics of VLF Sferics Associated With RHESSI TGFs”. In: *Journal of Geophysical Research: Atmospheres* 123.1, pp. 139–159. ISSN: 21698996. DOI: `10.1002/2017JD027624`.

Moss, Gregory D. et al. (2006). “Monte Carlo model for analysis of thermal runaway electrons in streamer tips in transient luminous events and streamer zones of lightning leaders”. In: *Journal of Geophysical Research: Space Physics* 111.2, pp. 1–37. ISSN: 21699402. DOI: `10.1029/2005JA011350`.

Neubert, Torsten et al. (2019). “The ASIM Mission on the International Space Station”. In: *Space Science Reviews* 215.2. ISSN: 15729672. DOI: `10.1007/s11214-019-0592-z`. URL: `http://dx.doi.org/10.1007/s11214-019-0592-z`.

Neubert, Torsten et al. (2020). “Ultraviolet Emissions Powered By Lightning”. In: 186.January, pp. 183–186.

Nisi, R. S. et al. (2014). “Journal of Geophysical Research : Space Physics An altitude and distance correction to the source fluence distribution of TGFs”. In: 16, pp. 8698–8704. DOI: `10.1002/2014JA019817.The`.

Østgaard, N. et al. (2013). “Simultaneous observations of optical lightning and terrestrial gamma ray flash from space”. In: *Geophysical Research Letters* 40.10, pp. 2423–2426. ISSN: 00948276. DOI: `10.1002/grl.50466`.

Østgaard, N. et al. (2019a). “First 10 Months of TGF Observations by ASIM”. In: *Journal of Geophysical Research: Atmospheres* 124.24, pp. 14024–14036. ISSN: 21698996. DOI: `10.1029/2019JD031214`.

Østgaard, Nikolai et al. (2019b). “The Modular X- and Gamma-Ray Sensor (MXGS) of the ASIM Payload on the International Space Station”. In: *Space Science Reviews* 215.2. ISSN: 15729672. DOI: `10.1007/s11214-018-0573-7`.

Phys252: Measurements of Auroral X-rays. Tech. rep. University of Bergen.

Pu, Yunjiao et al. (2019). “Low Frequency Radio Pulses Produced by Terrestrial Gamma-Ray Flashes”. In: *Geophysical Research Letters* 46.12, pp. 6990–6997. ISSN: 19448007. DOI: `10.1029/2019GL082743`.

Rakov, Vladimir and Martin A. Uman (2003). *Lightning physics and effects.*

Roberts, O. J. et al. (2018). “The First Fermi-GBM Terrestrial Gamma Ray Flash Catalog”. In: *Journal of Geophysical Research: Space Physics* 123.5, pp. 4381–4401. ISSN: 21699402. DOI: `10.1029/2017JA024837`.

Rodger, C. J. et al. (2012). “Relative detection efficiency of the World Wide Lightning Location Network”. In: *Radio Science* 47.6. ISSN: 00486604. DOI: `10.1029/2012RS005049`.

Rudlosky, Scott D. and Dustin T. Shea (2013). “Evaluating WWLLN performance relative to TRMM/LIS”. In: *Geophysical Research Letters* 40.10, pp. 2344–2348. ISSN: 00948276. DOI: `10.1002/grl.50428`.

Said, R. K. and M. J. Murphy (2016). “GLD360 Upgrade: Performance Analysis and Applications”. In: *24th International Lightning Detection Conference* Ic.

Said, R. K. et al. (2010). “Long-range lightning geolocation using a VLF radio atmospheric waveform bank”. In: *Journal of Geophysical Research Atmospheres* 115.23, pp. 1–19. ISSN: 01480227. DOI: `10.1029/2010JD013863`.

Said, R. K. et al. (2013). “Highly intense lightning over the oceans: Estimated peak currents from global GLD360 observations”. In: *Journal of Geophysical Research Atmospheres* 118.13, pp. 6905–6915. ISSN: 21698996. DOI: `10.1002/jgrd.50508`.

Shao, X. M. and P. R. Krehbiel (1996). “The spatial and temporal development of intracloud lightning”. In: *Journal of Geophysical Research Atmospheres* 101.21, pp. 26641–26668. ISSN: 01480227. DOI: `10.1029/96jd01803`.

Shao, Xuan Min et al. (2010). “A closer examination of terrestrial gamma-ray flash-related lightning processes”. In: *Journal of Geophysical Research: Space Physics* 115.6, pp. 1–8. ISSN: 21699402. DOI: `10.1029/2009JA014835`.

Skeltved, Alexander Broberg et al. (2017). “Constraints to do realisticmodeling of the electric field ahead of the tip of a lightning leader”. In: *Journal of Geophysical Research* 122.15, pp. 8120–8134. ISSN: 21562202. DOI: `10.1002/2016JD026206`.

Smith, D. M. et al. (2002). “The RHESSI spectrometer”. In: *Solar Physics* 210.1-2, pp. 33–60. ISSN: 00380938. DOI: `10.1023/A:1022400716414`.

Smith, David M. et al. (2005). “Terrestrial gamma-ray flashes observed up to 20 MeV”. In: *Science* 307.5712, pp. 1085–1088. ISSN: 00368075. DOI: `10.1126/science.1107466`.

Splitt, M. E. et al. (2010). “Thunderstorm characteristics associated with RHESSI identified terrestrial gamma ray flashes”. In: *Journal of Geophysical Research: Space Physics* 115.6, pp. 1–10. ISSN: 21699402. DOI: `10.1029/2009JA014622`.

Stolzenburg, Maribeth et al. (2007). “Electric field values observed near lightning flash initiations”. In: *Geophysical Research Letters* 34.4, pp. 1–7. ISSN: 00948276. DOI: `10.1029/2006GL028777`.

Takahashi, Tsutomu (1978). “Riming Electrification as a Charge Generation Mechanism in Thunderstorms”. In: *Journal of the Atmospheric Sciences* 35, pp. 1536–1548. URL: `http://repositorio.unan.edu.ni/2986/1/5624.pdf`.

Tavani, M et al. (2009). “The AGILE mission”. In: *Astronomy & Astrophysics* 1013, pp. 995–1013.

Thorsteinsen, T. F. (1995). *Strålingsfysikk.*

Wilson, C. T.R. (1924). “The electric field of a thundercloud and some of its effects”. In: *Proceedings of the Physical Society of London* 37.1. ISSN: 14787814. DOI: `10.1088/1478-7814/37/1/314`.